

SEARCH FOR RESONANT DOUBLE HIGGS PRODUCTION WITH bbZZ  
DECAYS IN THE  $b\bar{b}\ell\ell\nu\bar{\nu}$  FINAL STATE IN pp COLLISIONS AT  $\sqrt{s} = 13$  TeV

by

Rami Kamalieddin

A DISSERTATION

Presented to the Faculty of  
The Graduate College at the University of Nebraska  
In Partial Fulfilment of Requirements  
For the Degree of Doctor of Philosophy

Major: Physics and Astronomy

Under the Supervision of Professor Ilya Kravchenko

Lincoln, Nebraska

May, 2019

SEARCH FOR RESONANT DOUBLE HIGGS PRODUCTION WITH bbZZ  
DECAYS IN THE  $b\bar{b}\ell\ell\nu\bar{\nu}$  FINAL STATE IN pp COLLISIONS AT  $\sqrt{s} = 13$  TeV

Rami Kamalieddin, Ph.D.

University of Nebraska, 2019

Advisers: Ilya Kravchenko

Since the discovery of the Higgs boson in 2012 by the ATLAS and CMS experiments, most of the quantum mechanical properties that describe the long-awaited Higgs boson have been measured. Due to the outstanding work of the LHC, over a hundred of  $fb^{-1}$  of data have been delivered to both experiments. Finally, it became sensible for analyses teams to start working with a very low cross section processes, which made it possible to observe rare decay modes of the Higgs boson, e.g., a recent success in observing ttH and VHbb processes. One of the main remaining untouched topics is a double Higgs boson production. However, additional hundred of  $fb^{-1}$  per year from the HL-LHC will not necessarily help us much with the SM double Higgs physics, the process may remain unseen even in the most optimistic scenarios. The solution is to work in parallel on new reconstruction and signal extraction methods as well as new analysis techniques to improve the sensitivity of measurements. This thesis is about both approaches: we have used the largest available dataset at the time the analysis has been performed and developed/used the most novel analysis methods. One of such methods is the new electron identification algorithm that we have developed at the CMS electron identification group, to which I have had a privilege to contribute during several years of my stay at CERN.

The majority of this thesis is devoted to techniques for the first search at the LHC for the double Higgs boson production mediated by a heavy narrow-width resonance

in the  $b\bar{b}ZZ$  channel:  $X \rightarrow HH \rightarrow b\bar{b}ZZ^* \rightarrow b\bar{b}\ell\ell\nu\bar{\nu}$ . The measurement searches for a resonant production of a Higgs boson pair in the range of masses of the resonant parent particle from 250 to 1000 GeV using  $35.9\text{ }fb^{-1}$  of data taken in 2016 at 13 TeV. Two spin scenarios of the resonance are considered: spin 0 and spin 2. In the absence of the evidence of the resonant double Higgs boson production from the previous searches, we proceed with setting the upper confidence limits.

“... a place for a smart quote”

*Lenin, 1922.*

## ACKNOWLEDGMENTS

This will be a long list!

---

## Table of Contents

---

<b>List of Figures</b>	<b>ix</b>
<b>List of Tables</b>	<b>xv</b>
<b>1 Introduction</b>	<b>1</b>
<b>2 Theory</b>	<b>15</b>
2.1 Lagrangian formalism of the Standard Model . . . . .	15
2.2 Beyond the Standard Model . . . . .	19
<b>3 LHC and the CMS experiment</b>	<b>25</b>
3.1 Introduction . . . . .	25
3.2 The LHC . . . . .	28
3.2.1 The Magnets . . . . .	28
3.2.2 Radio Frequency System . . . . .	30
3.2.3 Vacuum System . . . . .	31
3.2.4 Powering . . . . .	32
3.2.5 Cryogenic system . . . . .	33
3.2.6 Beam dumping system . . . . .	35
3.2.7 Beam injection system . . . . .	36

3.2.8	LHC injection chain	36
3.3	The CMS experiment	37
3.3.1	The CMS challenging environment	38
3.3.2	CMS coordinate system	41
<b>4</b>	<b>Analysis overview</b>	<b>43</b>
4.1	Analysis Strategy	44
<b>5</b>	<b>Data and Triggers</b>	<b>46</b>
5.1	Data	46
5.2	Triggers	47
<b>6</b>	<b>Simulated Samples</b>	<b>55</b>
6.1	Signal simulation	55
6.2	Background simulation	56
<b>7</b>	<b>Physics Objects Reconstruction</b>	<b>59</b>
7.1	Electrons	59
7.2	Muons	60
7.3	Jets	61
7.4	Identification of b jets	62
7.5	Missing transverse energy	62
<b>8</b>	<b>Event Selection</b>	<b>64</b>
8.1	Higgs and Z Boson Selection	64
8.2	$H \rightarrow b\bar{b}$ and $Z \rightarrow \ell\ell$ variables to define signal and control regions	68
8.3	Signal and background characteristics	69
8.4	Data and MC comparison	71

8.5 Scale Factors . . . . .	73
<b>9 BDT Discriminant</b>	<b>75</b>
9.1 Construction of the BDT . . . . .	75
<b>10 Systematic Uncertainties</b>	<b>91</b>
10.1 Normalization uncertainties . . . . .	91
10.2 Shape uncertainties . . . . .	93
<b>11 Statistical Analysis</b>	<b>96</b>
<b>12 Limits Extraction</b>	<b>99</b>
12.1 Optimization for the best limit . . . . .	99
12.2 Results from the fit . . . . .	100
<b>13 <math>bbZZ</math> measurements and combination of all HH channels</b>	<b>106</b>
<b>14 Conclusions</b>	<b>109</b>
<b>Bibliography</b>	<b>111</b>
<b>References</b>	<b>111</b>

---

## List of Figures

---

1.1	The structure of an atom . . . . .	2
1.2	All SM interaction and simple vertices . . . . .	9
1.3	SM particles and force carriers . . . . .	10
1.4	Coupling of particles to SM Higgs boson . . . . .	11
1.5	SM Higgs boson production modes . . . . .	13
1.6	Higgs boson decay channels . . . . .	14
2.1	SSB Potential form . . . . .	18
2.2	SM double Higgs boson production. . . . .	21
2.3	Left: comparison of the double Higgs boson mass distribution at the LO at 14 and 100 TeV center-of-mass energy, Right: the total SM HH cross section and the box and the triangular contributions ("box" and "tri" at the plots). . . . .	22
2.4	BSM double Higgs boson production. . . . .	23
2.5	Double Higgs decay in the 2 b, 2 lepton, and 2 neutrino final state. . . .	24
2.6	Double Higgs decay channels according to the SM branching fractions. .	24
3.1	Schematic layout of the LHC. . . . .	27
3.2	The cross section of the LHC dipole . . . . .	29

3.3	Cables of the dipole magnet . . . . .	30
3.4	RF cavities module. . . . .	30
3.5	Beam screen. . . . .	32
3.6	13 kA high-temperature superconducting current lead. . . . .	33
3.7	Cross section of the LHC tunnel . . . . .	34
3.8	LHC cryogenic states and the temperature scale. . . . .	35
3.9	LHC injection complex. . . . .	37
3.10	CMS experiment with all sub-detectors shown. . . . .	38
3.11	Coordinate system of the CMS detector . . . . .	42
4.1	The Feynman diagram of the graviton/radion production with the subsequent decay to HH. HH system decays to a pair of b quarks and Z bosons. Shown is 2 b quarks, 2 leptons, and 2 neutrinos final state. . . . .	44
5.1	Electron scale factors in $p_T$ and $\eta$ bins for 2016 data set for the HLT_Ele23_Ele12_CaloIdL_Trigger. ID cut (general purpose MVA WP90) and ISO cuts are applied, then the scale factors are measured. Taken from [110] . . . . .	49
5.2	Muon scale factors in $p_T$ and $\eta$ bins for 2016 data runs B, C, D, E, F, G for the HLT_Mu17_TrkIsoVVL_Mu8_TrkIsoVVL_v* OR HLT_Mu17_TrkIsoVVL_TkMu8_TkIsoVVL_v* triggers. Left: Scale factors for 8 GeV leg. Right: Scale factors for 17 GeV leg, provided that the subleading leg passed 8 GeV cut. . . . .	50
5.3	Muon scale factors in $p_T$ and $\eta$ bins for 2016 data run H for the HLT_Mu17_TrkIsoVVL_Mu8_OR_HLT_Mu17_TrkIsoVVL_TkMu8_TrkIs_oVVL_v* triggers. Left: Scale factors for 8 GeV leg. Right: Scale factors for 17 GeV leg, provided that the subleading leg passed 8 GeV cut. . . . .	50

5.4	Scale factors in $\eta$ bins of the leading and subleading muons for 2016 data set for dZ requirement, measured after muons have passed the HLT_Mu17_TrkIsoVVL_Mu8_OR HLT_Mu17_TrkIsoVVL_TkMu8_TrkIsoVVL_v* triggers. . . . .	51
5.5	Muon ID scale factors in $p_T$ and $\eta$ bins. Left: runs B to F. Right: runs G and H. . . . .	52
5.6	Muon ISO scale factors in $p_T$ and $\eta$ bins. Left: runs B to F. Right: runs G and H. . . . .	53
5.7	Electron ID+ISO scale factors in $p_T$ and $\eta$ bins. . . . .	54
7.1	Z boson (left) and photon (right) kinematics with the vector of all the visible objects (denoted by u) and a resulting MET. . . . .	63
8.1	Significance-like ( $\sqrt{S}/B$ ) figure of merit as a function of the MET cut. Green curve shows the significance for our analysis keepings event above the cut, red curve is for HIG-18-013 analysis and their phase space is below the cut value. Top: 300 GeV cut. Middle: 600 GeV cut. Bottom: 900 GeV cut. On the left dielectron channel is shown, while dimuon plots are on the right. . . . .	67
8.2	Signal region, control region $t\bar{t}$ , and control region Drell-Yan in the phase space of $Z \rightarrow \ell\ell$ and $H \rightarrow b\bar{b}$ masses. . . . .	68
8.3	Cut flow for mm (top) and ee (bottom) channels. . . . .	72

8.4	Transverse mass of the reconstructed HH candidates for data, the simulated signal graviton sample for the 300 GeV mass hypothesis, and simulated backgrounds scaled according to the fit results. The top row shows the figures for the muon channel while the bottom row is for the electron channel. For each row, the left plot is for the Drell-Yan control region, the middle is for the $t\bar{t}$ control region, and the right is for the signal region. Signal normalization choice is discussed in the text. The crosshatched area represents the sum of statistical and systematic uncertainties. . . . .	73
8.5	Transverse mass of the reconstructed HH candidates for data, the simulated signal radion sample for the 300 GeV mass hypothesis, and simulated backgrounds scaled according to the fit results. The top row shows the figures for the muon channel while the bottom row is for the electron channel. For each row, the left plot is for the Drell-Yan control region, the middle is for the $t\bar{t}$ control region, and the right is for the signal region. Signal normalization choice is discussed in the text. The crosshatched area represents the sum of statistical and systematic uncertainties. . . . .	74
9.1	Ranking of variables in the BDT training for electron(muon) channel at the top(bottom). Left: low mass BDT. Right: high mass BDT. . . . .	76
9.2	BDT plots for radion case, electron(muon) channel at the top(bottom). Signal region, 300 GeV mass hypothesis. For electrons cut is at 0.4, for muons at 0.7. More details at the table 12.1. . . . . . . . . . .	77
9.3	Variables used in the low mass training for electron channel. Index '1' refers to $b\bar{b}$ and index '0' refers to ZZ. . . . . . . . . . .	78
9.4	Variables used in the high mass training for electron channel. . . . .	79

9.5	BDT discriminants for electron channel. Top: low mass training. Bottom: high mass training. . . . .	81
9.6	ROC curves for electron channel. Top: low mass training. Bottom: high mass training. . . . .	82
9.7	Input variables correlations for electron channel, low mass training. Top: signal sample mix. Bottom: background sample mix. . . . .	83
9.8	Input variables correlations for electron channel, high mass training. Top: signal sample mix. Bottom: background sample mix. . . . .	84
9.9	Variables used in the low mass training for muon channel. Index '1' refers to $b\bar{b}$ and index '0' refers to ZZ. . . . .	85
9.10	Variables used in the high mass training for muon channel. . . . .	86
9.11	BDT discriminants for muon channel. Top: low mass training. Bottom: high mass training. . . . .	87
9.12	ROC curves for muon channel. Top: low mass training. Bottom: high mass training. . . . .	88
9.13	Input variables correlations for muon channel, low mass training. Top: signal sample mix. Bottom: background sample mix. . . . .	89
9.14	Input variables correlations for muon channel, high mass training. Top: signal sample mix. Bottom: background sample mix. . . . .	90
12.1	Cut on the BDT output vs 'r-value' from Combine. Electron channel. . .	103
12.2	Cut on the BDT output vs 'r-value' from Combine. Muon channel. . .	104

12.3 Expected (dashed line) and observed (solid line) limits on the cross section of a resonant HH production as a function of the mass of the narrow resonance for both leptonic channels combined. Graviton case is shown at the top and radion case at the bottom. The red line shows a theoretical prediction for the production of a WED particle with certain model assumptions [63]. . . . .	105
13.1 Combination of HH channels using 2016 data. Expected (dashed) and observed (solid line) 95% CL exclusion limits are shown. The results describe the production cross section of a narrow width spin 0 (top) and spin 2 (bottom) resonance decaying into a pair of SM Higgs bosons. . .	108

---

## List of Tables

---

5.1	List of used 2016 DoubleMuon data sets. An uncertainty of 2.5% is assigned for the 2016 data set luminosity [101] . . . . .	46
5.2	Triggers for dimuon and dielectron analysis channels both at L1 and HLT levels. . . . .	47
6.1	Background Monte Carlo samples . . . . .	57
8.1	$\cancel{E}_T$ cut to orthogonalise the analysis with respect to HIG-18-013. . . . .	66
8.2	Efficiency of the BDT selection requirement. $ee$ channel (top) and $\mu\mu$ channel (bottom). . . . .	69
8.3	Number of events surviving analysis cuts corresponding to the last entry in the 8.3 . . . . .	71
12.1	Suboptimal BDT cuts used in the analysis . . . . .	100
12.2	The expected and observed HH production cross section upper limits at 95% CL for different narrow resonance graviton (top) and radion (bottom) mass hypotheses for both dielectron and dimuon channels combined. . .	102

## CHAPTER 1

---

### Introduction

---

Richard Feynman, a Physics Nobel Prize winner whom I consider one of the brightest physicists who has ever lived on Earth, once summarised in one single phrase what he believed to be the most important fact about the world around us: "all things are made of atoms" [1]. Feynman himself was the father of the quantum electrodynamics but in this simple statement delivered originally to Caltech students and now known to everyone through his series of physics books, he decided not go into quantum mechanics principles and rather illustrated at the highly abstract level that everything is made of smaller particles.

Nowadays we know that atoms have heavy nuclei and light electrons "orbiting" around the nucleus on the electron shells. The nucleus is positively charged proportionally to the number of protons it contains. To provide the stability of the nuclei of the heavy atoms our world also needs neutrons, which have no electric charge. Going further to an even smaller scale, we now know that protons and neutrons are not elementary, instead they are composed of point-like constituents that are called quarks (see Figure 1.1).

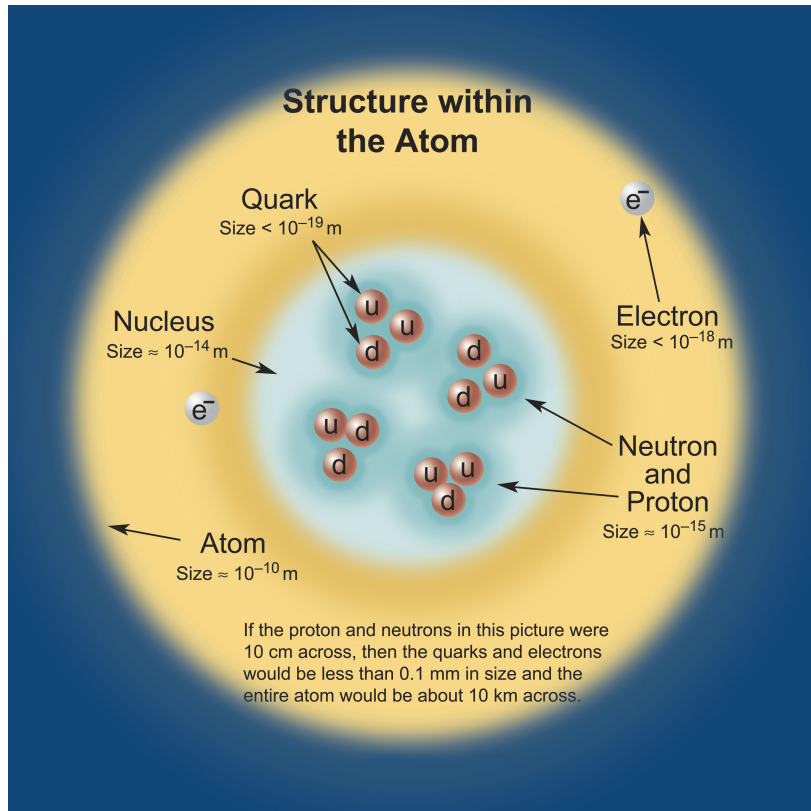


**Figure 1.1:** The structure of an atom. Approximate scale values are indicated.

Quarks were proposed by Gell-Mann and also by Zweig to explain periodicity in properties of observed subatomic particles. [2]. Quarks come in three families, or generations, and are arranged into doublets. A doublet is mathematical construct that is used to explain two-level/value system. For example, by design of Gell-Mann and Zweig, each doublet in their theory is a two quark system that has an "up" quark with the electric charge  $-1/3$  and a "down" quark with the charge  $+2/3$ . For antiquarks signs are reversed.

Physics world before Gell-Mann and Zweig got used to the fact that particles have integer charges due to enormous number of observations. The fact that the quark charge values were fractional was so revolutionary that Gell-Mann decided not to publish his article in a highly prestigious journal but, expecting a rejection,

decided to go with the second tier one [2]. There are six different types of quarks and to distinguish one from another there is a "flavor" number assigned to them. For instance, a charm quark has +1 unit of "charmness", while a strange quark has -1 unit of "strangeness". All the other quark flavor fields are zero for them. And this pattern is applied to all the other four quarks to fill the corresponding "quarkness" numbers. Besides, the mass of quarks increases from the first to the third family. No explanation exists in the Standard Model (SM).

SM is the mathematical theory that has been extremely successful describing the interactions of elementary particles and fields. SM includes all known interactions except gravity. For the last several decades SM is the most tested theory of fundamental forces and elementary particles and is presently generally accepted by the whole physics community. Formally, all SM elementary particles are split into two classes: fermions and bosons. Particles with the half-integer spin 1/2 (quarks and leptons) are called fermions since they obey Fermi-Dirac statistics [3]. The other class of particles is bosons. They are force carriers, have an integer spin, and are characterised by the Bose-Einstein statistics.

Continuing with quarks, their another important characteristics has been revealed at the  $e^+e^-$  colliders when physicists compared production rates of muons and hadrons. The theory was off by a factor of three. This was the motivation to introduce three quark colours: green, blue, and red. Quarks were observed decades after electrons have been discovered. In particle physics, electron belong to a family of leptons. A lepton is an elementary particle with the spin 1/2 that participates in all but strong interactions, which will be discussed in more detail later in this chapter. An electron was discovered by Thompson [4] in 1897 when he was studying the properties of a cathode ray. Due to this discovery, that year may be considered the beginning of an era of a particle physics: a dozen of particles have been discovered in

the next decades. In 1936, another lepton was observed, a muon [5], in an experiment of Anderson and Neddermeyer who studied cosmic radiation. In essence, a muon is almost a copy of an electron, but is 207 times heavier and no explanation for this mass difference exists in the SM. As a side note, according to Carl Bender, there is a story that Feynman was able to derive the mass of the muon starting with the mass of an electron, but the world has never seen that calculation published [6].

Analogously to quark families, leptons are also arranged in generations. Each generation is a doublet that consists of a charged lepton (electron, muon or tau) with the charge  $-1$  and a neutral lepton (corresponding electron, muon, or a tau neutrino). An electron and a muon neutrinos have been discovered in 1956 and 1962, respectively. The existence of the electron neutrino was deduced from the violation of the conservation of energy in a beta decay, while the muon neutrino [7] was discovered by Schwartz, Lederman, and Steinberger during an experiment with the pion beam where leptons from the pion decays arrive to the aluminum spark chamber after passing the steel wall. 51 events of interest have been observed after running the experiment for several months. Those events could not be due to electron neutrinos, since they will interact with the metal and produce electrons. The presence of narrow muon tracks in the chamber in each event, hence muons, was a clear indication that those neutrinos were of a different kind, they were muon neutrinos. Finally, a tau lepton and a tau neutrino were discovered in 1975 and 2000 correspondingly [8, 9]. With that, all three families of the SM leptons were observed: a long-awaited tau neutrino, which was decades ago theoretically speculated to exist, was finally discovered experimentally. In a like manner to families of quarks, lepton masses grow with the generation, where a tau from the third generation is the heaviest lepton. To classify leptons of different families the lepton numbers have been reserved: 1 unit of electron number to an electron and an electron neutrino, 1 unit of muon

number to a muon and an muon neutrino, and 1 unit of tau number to a tau and a tau neutrino.

In the SM there are four fundamental forces: gravitational, weak, electromagnetic, and strong forces. We will classify all four forces [10] in terms of the relative strength, the range that they can cover, the spin of the mediator, and whether the force's nature is attractive, repulsive, or both. This should be taken with the grain of salt though, since this is quite ambiguous categorisation, but it has a deep pedagogical meaning because it helps to illustrate in which regime each of the forces is dominant. According to Carl Bender, this is of great importance since it is one of the main approaches to solving physics problems: to know which effects are the dominant and which are sub-dominant. This helps to justify what effect can be neglected and what approximation can be used, thus, allowing the possibility to do calculations for problems where closed-form solutions do not exits, which is almost all the complex phenomena around us [6].

The first force on our list of SM forces is the the gravitational force. This force governs the Universe at the macroscopic level: planets, solar systems, etc. The first theory of gravity was formulated by Newton [11] and then further developed by Einstein. A good historical perspective is available at [12]. It is worth noting that the gravitational force is not included in the SM. Attempts are ongoing to expand the SM, e.g., adding the graviton as a mediator, but no real success so far has been achieved to create a renormalizable theory that would combine both SM and gravity [13]. To surprise of many, gravity is the weakest force, the only reason why the motion of planets and galaxies is governed by gravity is because those are gigantic objects. Gravity effects become the dominant ones at the macroscopic scale because of an enormous number of particles involved in the interaction. If the strength of the strongest force, which is the strong force, is set to 1, then the strength of the gravity

will be about  $10^{-41}$ . It is contemplated that the gravity mediator (the graviton), if exists, would have a charge of zero, zero mass, spin 2, and should be a stable particle. The gravitational force is of the infinite range and its nature is purely attractive, while all other three forces can exhibit both an attractive and a repulsive behaviour. Einstein's general relativity theory is the only proven working theory of gravity as of now, though not a quantum theory.

The next force we are going to discuss is the weak force. It is mediated by a charged W (charge +1/-1) boson or a neutral Z boson, thus giving name to charged and neutral weak interactions correspondingly. All SM fermions experience the weak force, both quarks and leptons. The relative strength of the weak force is  $10^{-16}$  and the range of applicability is  $10^{-3}$  fm. All three weak bosons ( $W^+$ ,  $W^-$ , and Z) have spin 1 and are quite massive:  $m_{W^\pm} = 80.385$  GeV and  $m_Z = 91.189$  GeV. GeV is the unit of the so-called "natural system of units", in which  $\hbar = c = 1$ . This system is very popular in the high-energy physics and is widely used in this thesis. Adoption of this system simplifies how many equations look and also makes a fine-structure constant  $\alpha \approx 1/137$  dimensionless. Using the natural system of units [14] masses, momenta, and energies are measured in electronvolts (eV), with GeV ( $10^9$  eV) and TeV ( $10^{12}$  eV) being the most popular units in a modern high-energy physics due to energy regimes involved.

Charged weak interactions are interesting due to the fact that a primitive interaction vertex can be intuitively thought of as a point where a charged lepton is converted to a neutral lepton or vice versa. A good example is a muon decay, which is nothing but a conversion of the muon to a muon neutrino with the help of the W boson, which further decays to an electron and a corresponding electron antineutrino. It is worth noting that charged weak interactions do not conserve the flavor of quarks, e.g., members of doublets of the third and the second families can be converted

into members of the lower family of quarks. This fact is reflected in the Cabibbo-Kobayashi-Maskawa (CKM) matrix [15]. This matrix describes the strength of the flavour-changing weak interactions. Since diagonal elements of this matrix are less than one and off-diagonal elements are non-zero, CKM matrix represents a mismatch of quantum states of quarks when they propagate freely and when they take part in the weak interactions. In other words, the CKM matrix with non-zero off-diagonal elements means cross-generation interactions are allowed and this is the information that the CKM matrix quantifies.

$$\begin{pmatrix} |V_{ud}| & |V_{us}| & |V_{ub}| \\ |V_{cd}| & |V_{cs}| & |V_{cb}| \\ |V_{td}| & |V_{ts}| & |V_{tb}| \end{pmatrix} = \begin{pmatrix} 0.97427 \pm 0.00015 & 0.22534 \pm 0.00065 & 0.00351^{+0.00015}_{-0.00014} \\ 0.22520 \pm 0.00065 & 0.97344 \pm 0.00016 & 0.0412^{+0.0011}_{-0.0005} \\ 0.00867^{+0.00029}_{-0.00031} & 0.0404^{+0.0011}_{-0.0005} & 0.999146^{+0.000021}_{-0.000046} \end{pmatrix}. \quad (1.1)$$

In SM several multi-boson vertices are allowed. W and Z bosons that mediate weak interactions can couple to each other, so  $WWZ$ ,  $WWWW$ , and  $WWZZ$  vertices are possible in the SM. In addition, W boson that participates in charged weak interactions also couples to photons, so  $\gamma WW$ ,  $\gamma WWZ$ , and  $WW\gamma\gamma$  vertices are also allowed.

Now, we are moving to the electromagnetic (EM) force. This is one of the main forces that we experience in our everyday life. The reason the reader can sit in the chair and do not fall further down due to gravity, is that electrons of the reader's body repel electrons of the chair. Relative strength of the EM force is  $10^{-3}$  and the range of applicability is infinite. A photon, as its mediator, has zero mass, spin 1, and the theory that describes its interaction with leptons and quarks is called quantum electrodynamics (QED), developed in 1940th and 1950th by Tomonaga, Schwinger, Feynman, and Dyson [16]. Electric charge is conserved in EM interactions and no

single photon-to-fermion vertex is possible, there are always two fermions that must be involved. Lastly, even though Z boson is massive and photon is massless, Z boson is neutral, thus, any interaction where the photon is a force carrier, can be also mediated by the Z boson.

Finally, we can talk about the forth force of the SM - the strong force. This is the strongest known force and the gluons are the carriers. There are nine types of gluons and each gluon carries one unit of color and one unit of anticolor. But, technically, the ninth gluon is a color invariant, and would give rise to an infinite range of the strong force, which contradicts experiments. That is why modern physics assumes that in our world only eight gluons exist [2, 15]. Gluons carry color charge and can couple to each other. For several high order processes in quantum chromodynamics (QCD), 3- and 4-gluon vertices have to be introduced to restore gauge invariance and no higher order vertices are required [17].

We can summarise the knowledge about four fundamental forces in one figure using the Feynman diagram representation [18]. Fig. 1.2 shows all allowed SM particle interactions and corresponding simple vertices.

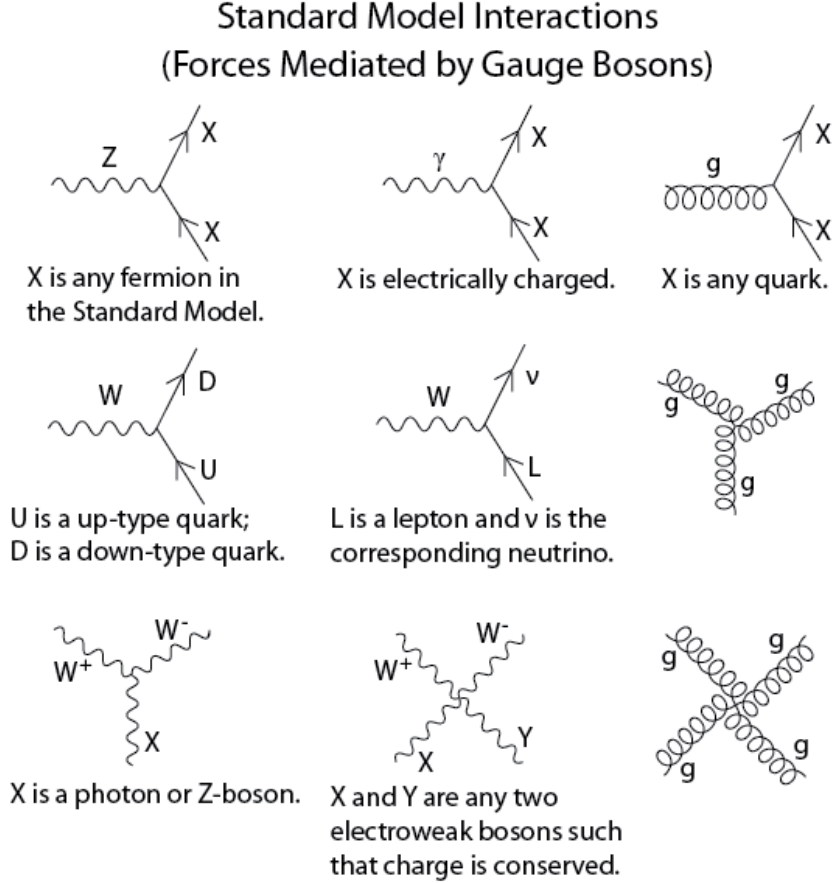


**Figure 1.2:** All SM interaction and simple vertices.

The description of the SM picture will not be complete without mentioning the main particle, yet missing until 2012<sup>th</sup> ... the Higgs boson! (Fig. 1.3 [19]) After the electroweak (EW) unification by Glashow, Salam, and Weinberg [20], it was still not clear what is the origin of the mass of fundamental particles. In 1964, Robert Brout and François Englert [21], Peter Higgs [22], Gerald Guralnik, C. Richard Hagen, and Tom Kibble [23] (BEHGHK authors), proposed the method by which the particles can acquire mass. This technique consists of three stages and we will discuss them one-by-one:

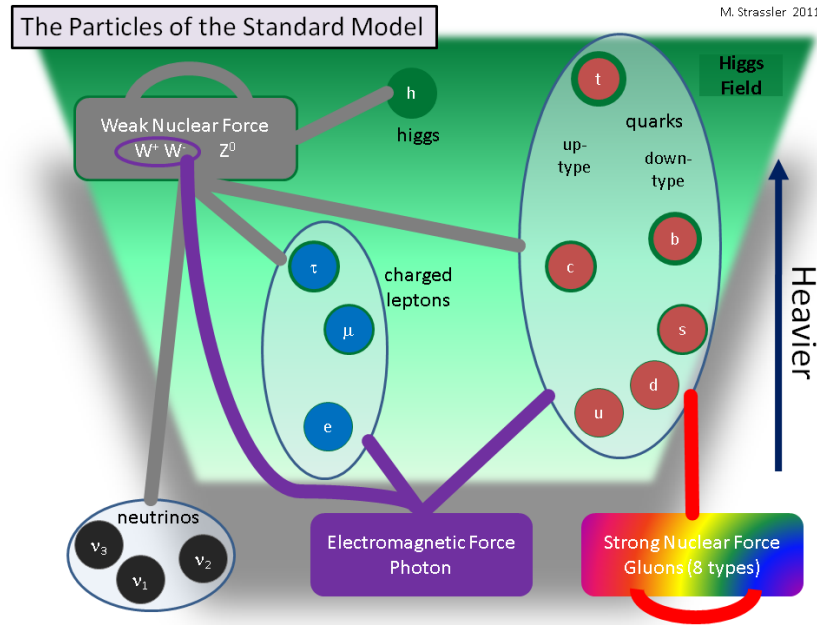


**Figure 1.3:** SM particles and force carriers. Self-interactions are also shown. The strength of the coupling to the Higgs boson increases from the bottom to the top, which is illustrated by the shades of the green color (the Higgs field).

1. The Brout-Englert-Higgs (BEH) mechanism
2. The BEH field
3. The Higgs boson.

The first stage, the BEH mechanism, is simply a spontaneous symmetry breaking (SSB) mechanism, which is a mathematical trick consisting of rewriting the original scalar fields in the EW Lagrangian, rearranging equations, and requiring that the fields are real. What does this lead to? We started with a scalar complex field and a massless vector field and after SSB we obtained a single real scalar field (Higgs boson) and a massive vector field. In terms of our physical world this it what gives mass to W and Z bosons.

The second stage is the BEH field. It exists everywhere and has been present almost since the Big Bang [24]. It is a property of our world. All the fundamental particles that interact with the BEH field acquire mass. Those, who do not interact directly (at the tree level), have no mass and all their energy is in the form of the momentum, thus they can travel with the speed of light. The more the particle interacts with the BEH field, the higher is the coupling to the Higgs boson or simply the higher is the mass of the particle. For example, the coupling of the Higgs boson to fermions is proportional to the mass of the fermions, while for W and Z bosons it is proportional to the squared mass of bosons, thus top quark and Z bosons are quite massive (see Fig. 1.4 [25]).

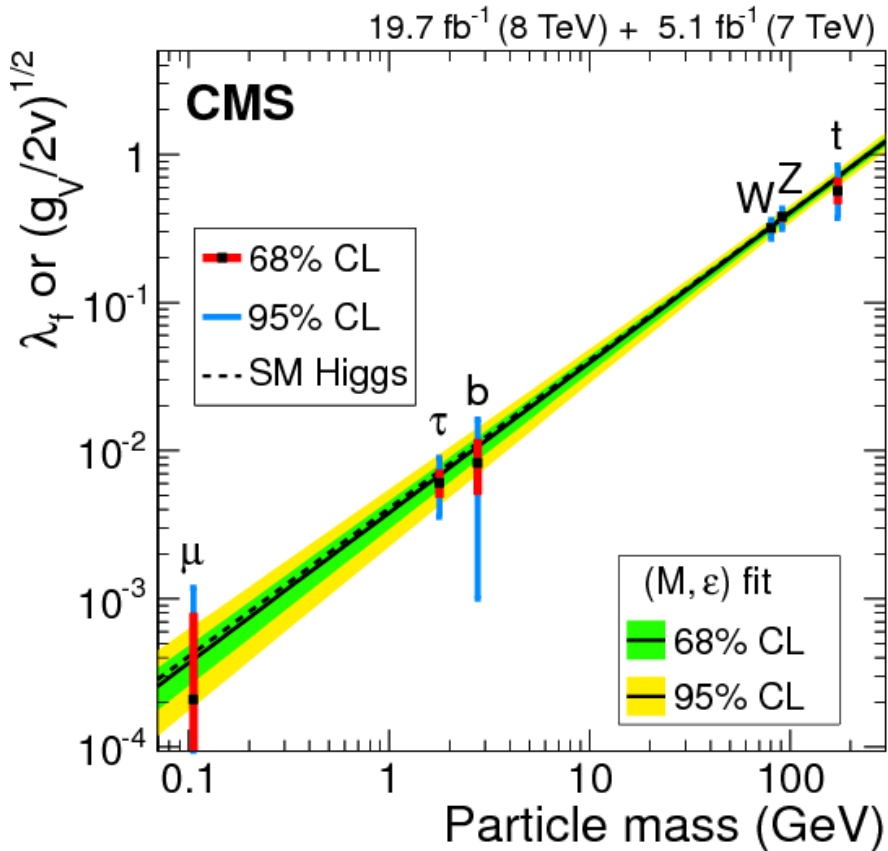


**Figure 1.4:** Coupling of particles to SM Higgs boson versus the mass of the particle, log-log scale is used.

The third and arguably the most important stage - the Higgs boson. The Higgs boson is the excitation of the BEH field. Thus, the Higgs bosons can be produced at colliders by pumping more and more energy in a small space-time region exciting the BEH field to "produce" the Higgs bosons. In reality this happens through making the LHC beams more energetic and thus, during the collision, having more energetic gluons (and also quarks). The main production mechanism is called a gluon fusion, when through the top quark loop a single Higgs boson is produced. This accounts for about 90% of the overall LHC Higgs production at the 13 TeV energy. The second mechanism is a vector boson fusion. The third mechanism is the associated production with a weak boson. And the smallest contributor to the Higgs boson production is the ttH process, which stands for the associated production of the Higgs boson with the top anti-top quark pair. All mentioned Higgs boson production mechanisms are presented in the form of Feynman diagrams in Fig. 1.5.

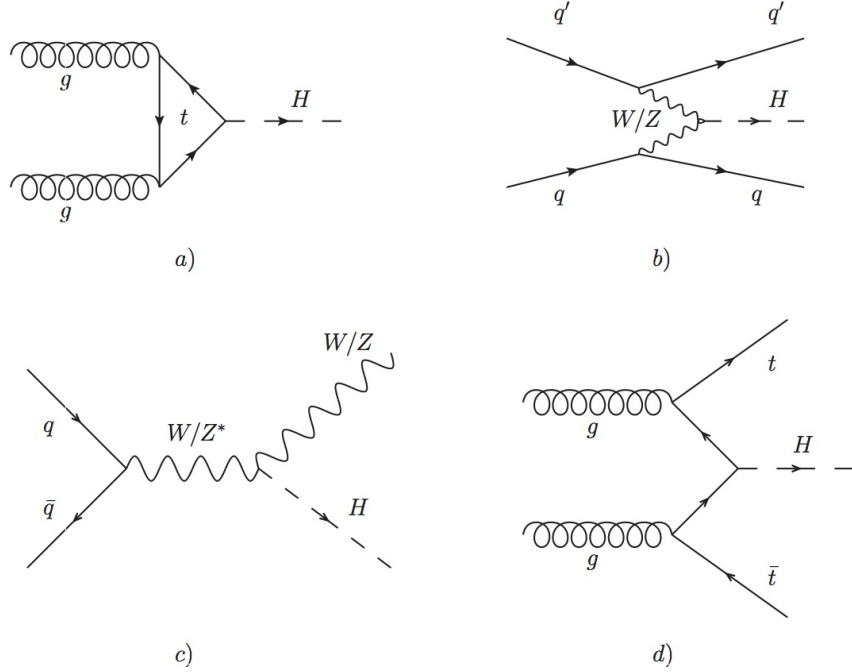


**Figure 1.5:** SM Higgs boson production modes: a) a gluon fashion, b) a vector boson scattering, c) an associated production with a vector boson, d) an associated production with the top anti-top pair.

The final important aspect of the Higgs boson physics is the decay channels of the Higgs boson, in other words probabilities with which Higgs boson decays to other particles, so called branching fractions (see Fig. 1.6). This analysis focuses on two Higgs boson decays,  $H \rightarrow b\bar{b}$  and  $H \rightarrow ZZ$ . The first one has the highest branching ratio, while the second one gives a clean signature when subsequent  $Z \rightarrow \ell\ell$  decays are selected. Before we conclude with the BEHGHK method, a little bit of history, an irony of life, actually. The BEH particle is called the Higgs boson, but Peter Higgs was not the first to publish the article on the BEH mechanism, in fact he was the last out of BEHGHK authors! His very first article was rejected since it contained no specific predictions or conclusions drawn from his calculations. This is why he was out-published by others. But this rejection made him write another article where he explicitly predicted an existence of the new boson. And this is what has made all the

difference, he was the first to predict a new boson, and this boson now is called the Higgs boson.

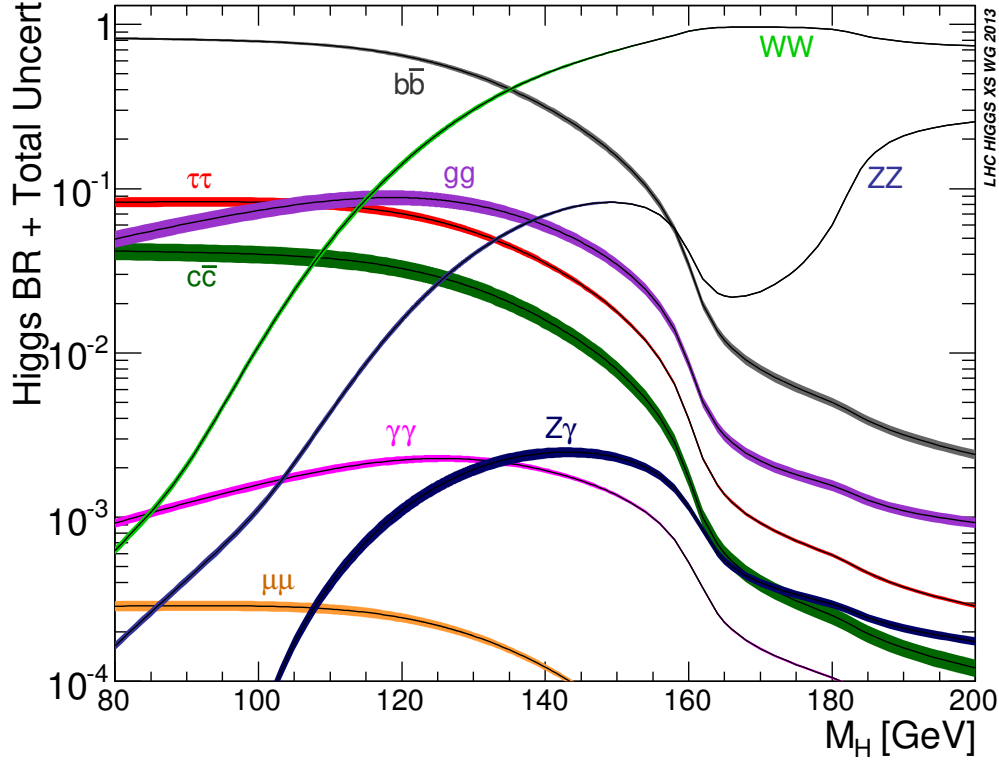


**Figure 1.6:** Higgs boson decay channels. At 125 GeV the dominant decay mode is  $H \rightarrow b\bar{b}$ .

Even though the facts above tell us about how great the SM is, SM is still far from being perfect. Masses of elementary particles are the parameters in this theory, they do not come from SM predictions. It is hypothesised that the SM could be a part of the larger ultimate theory, the so-called "The Theory of Everything" (TOE), which is to be written (had been a lifelong journey of another genius, Einstein [26]). There is hope that the TOE will be able to explain many phenomena, such as the quark mass hierarchy, flavor mixing, etc. Also, in the SM all neutrinos are massless, however, it has been shown that they have a non-zero mass [27]. This fact is one of the main motivations for theorists to look for extensions of the SM.

## CHAPTER 2

---

### Theory

---

In the previous chapter we introduced the SM and discussed particles and interactions that the SM as a theory describes. In this chapter we will discuss first the general mathematical formalism of the SM and in the second part we will focus on the double Higgs theory in the BSM .

## 2.1 Lagrangian formalism of the Standard Model

The SM uses the Lagrangian mechanics as the mathematical approach to describe quantitatively the interactions of elementary particles and fields. The SM Lagrangian can be split into four main contributions [126]:

$$\mathcal{L}_{SM} = \mathcal{L}_{YM} + \mathcal{L}_{ferm} + \mathcal{L}_H + \mathcal{L}_{Yuk} \quad (2.1)$$

This equation contains the following terms:

- gauge bosons and their interactions,  $\mathcal{L}_{YM}$
- fermions and their interactions with the gauge bosons,  $\mathcal{L}_{ferm}$

- Higgs boson, its self-interaction, and interaction with the gauge bosons to give them mass,  $\mathcal{L}_H$
- fermions and their interactions with the Higgs boson, which through the Yukawa mechanism give mass to fermions  $\mathcal{L}_{Yuk}$

The first term in the SM Lagrangian in full can be written as:

$$\mathcal{L}_{YM} = -\frac{1}{4}W_{\mu\nu}^i(x)W_i^{\mu\nu}(x) - \frac{1}{4}B_{\mu\nu}(x)B^{\mu\nu}(x) - \frac{1}{4}G_{\mu\nu}^a(x)G_a^{\mu\nu}(x) \quad (2.2)$$

where

$$B_{\mu\nu}(x) \equiv \partial_\mu B_\nu - \partial_\nu B_\mu \quad (2.3)$$

$$W_{\mu\nu}^i(x) \equiv \partial_\mu W_\nu^i(x) - \partial_\nu W_\mu^i(x) - g\varepsilon^{ijk}W_\mu^jW_\nu^k \quad (2.4)$$

$$G_{\mu\nu}^a(x) \equiv \partial_\mu G_\nu^a(x) - \partial_\nu G_\mu^a(x) - g_s f^{abc}G_\mu^bG_\nu^c \quad (2.5)$$

with indexes  $i, j, k = 1, 2, 3$  and  $a, b, c = 1, \dots, 8$ . According to the Noether's theorem, each symmetry is intrinsically connected to the conservation law [137]. The fields in the  $\mathcal{L}_{YM}$  are connected to their corresponding underlying symmetries. For instance,  $B_{\mu\nu}$  corresponds to  $U(1)$  symmetry of the weak hypercharge  $Y_k$ ,  $W_{\mu\nu}^i$  corresponds to  $SU(2)_I$  symmetry of the weak isospin  $I_w^i$ , and  $G_{\mu\nu}^a$  corresponds to  $SU(3)_c$  symmetry of the QCD color charge. The "B" field is a kinematic term, "W" and "G" terms describe interactions among the bosons,  $g$  and  $\varepsilon$  are  $SU(2)$  coupling and structure constants, finally  $g_s$  and  $f$  are coupling and structure constants for  $SU(3)$ .

The second term in the SM Lagrangian shows how fermions interact with the

gauge bosons. Notice, that the mass terms are still absent:

$$\mathcal{L}_{ferm} = i\bar{\Psi}_L \not{D} \Psi_L + i\bar{\psi}_{l_R} \not{D} \psi_{l_R} + i\bar{\Psi}_Q \not{D} \Psi_Q + i\bar{\psi}_{u_R} \not{D} \psi_{u_R} + i\bar{\psi}_{d_R} \not{D} \psi_{d_R} \quad (2.6)$$

Above  $\Psi$  represents a doublet of a charged lepton and a corresponding neutral lepton within the same lepton family of  $SU(2)_L$ , the letter Q is reserved for a family of quarks, and  $\psi_R$  describes a right-handed leptonic singlet.

Gauge boson interactions are present due to the derivative term:

$$D_\mu = \partial_\mu + igI_w^i W_\mu^i + ig'Y_w B_\mu + ig_s T_c^a G_\mu^a \quad (2.7)$$

(2.8)

Physical fields in this notation are represented by a linear combination of W and B fields:

$$A_\mu = B_\mu \cos \theta_W + W_\mu^3 \sin \theta_W \quad (2.9)$$

$$Z_\mu = -B_\mu \sin \theta_W + W_\mu^3 \cos \theta_W$$

where  $\theta_W$  is known as the *Weinberg angle* [128].

With the first two terms of the SM Lagrangian we obtain a valid theory of fermions and bosons, however, these particles are massless in this theory [127], which evidently contradicts the reality. To solve this issue and to ensure that weak bosons are massive, we need to introduce a Higgs field. Higgs mechanism enters the SM Lagrangian through the corresponding Higgs Lagrangian term given by

$$\mathcal{L}_H = (D_\mu \Phi)^\dagger (D^\mu \Phi) - V(\Phi), \quad V(\Phi) = -\mu^2 (\Phi^\dagger \Phi) + \frac{\lambda}{4} (\Phi^\dagger \Phi)^2 \quad (2.10)$$

where

$$\Phi = \begin{pmatrix} \phi^+ \\ \phi^0 = (v + H + i\chi)/\sqrt{2} \end{pmatrix} \quad \text{with} \quad v = 2\sqrt{\frac{\mu^2}{\lambda}} \quad (2.11)$$

Here  $\mu$  and  $\lambda$  are parameters of the Higgs potential. The Higgs boson mass is proportional to the  $\mu$  parameter. In 2012 with precise single Higgs boson mass measurements from both ATLAS and CMS experiments we determined the value of  $\mu$ . Since that time many analyses at CERN have been targeting the measurement of the  $\lambda$  parameter, because it is related to the shape of Higgs potential. The simplest interaction that is probing the Higgs potential directly is the Higgs boson self-coupling. One of such processes is the non-resonant double Higgs boson production. With double Higgs boson physics being such a valuable tool to determine the

After the SSB, the value of the Higgs field vacuum expectation value  $v$  shown above can be expressed in terms of  $\mu$  and  $\lambda$  [129]. See Fig. 2.1 for an illustration for the Higgs potential before and after SSB.

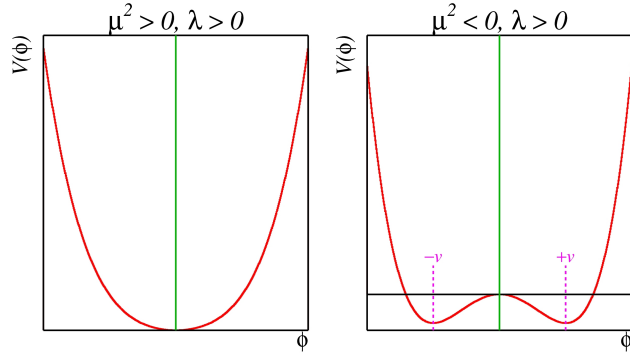


**Figure 2.1:** Shape of the Higgs potential before and after SSB that is determined at the leading orders by  $\mu$  and  $\lambda$  parameters.

After adding  $\mathcal{L}_H$  and rearranging terms, bosons have masses given by:

$$M_W = \frac{gv}{2}, \quad M_Z = \frac{M_W}{\cos \theta_W}, \quad M_H = \sqrt{2\mu^2} \quad (2.12)$$

The final contribution to the SM Lagrangian is the Yukawa term, and Yukawa Lagrangian is given by:

$$\mathcal{L}_{Yuk} = -i\bar{\Psi}_L G_l \psi_{l_R} \Phi - i\bar{\Psi}_Q G_u \psi_{u_R} \tilde{\Phi} - i\bar{\Psi}_Q G_d \psi_{d_R} \Phi + h.c. \quad (2.13)$$

where  $\tilde{\Phi} = i\sigma^2 \Phi^*$

The masses of fermions enter the equations through the  $3 \times 3$  matrices  $G$ , which are not known from the theory and are the parameters of the SM. The mass of each fermion is proportional to the Yukawa coupling of the corresponding fermion to the Higgs boson, see Fig. 1.4.

## 2.2 Beyond the Standard Model

Several BSM theories [33, 60, 62] predict a resonant production of the double Higgs boson events through a heavy narrow width ( $\sim O(1 - 10)$  GeV) resonance, which could be spin 0 or spin 2 particle [130]. In this particular analysis data is compared with respect to predictions from the Warped Extra Dimensions theory (WED) [63]. WED theory to address the hierarchy problem adds additional fifth dimension to the 4-dimensional (4D) space-time. In the framework that Randall and Sundrum (RS) [131] followed, 4D space is nothing but an EFT approximation of the higher dimensional space, where the radion or graviton may exist as Kaluza-Klein (KK) [132] excitation modes at the TeV scale. Since LHC had provided us with no evidence of the SM particles interacting with the additional RS dimensions, it is postulated that they are confined to 3-brane, or a so-called wall. At the same time, gravity, which

is not in the SM, can propagate freely in the full higher-dimensional space, so-called bulk. If/when the bulk is compactified, it may produce KK modes of the gravitons. In this analysis RS model with parameter  $k$  of the order of Planck scale and  $\bar{M}_{Pl}$ , a reduced 4D  $M_{Pl}$  which is a function of the 5D Planck scale  $M$  and a parameter  $k$  with  $k < M$ , are assumed to satisfy the constraint  $0.01 \leq k/\bar{M}_{Pl} \leq 1$ , because values outside of this range are not applicable/or overcomplicate the theory [133]. Considered in this measurement graviton and radion are thus RS KK graviton and RS radion particles that emerge in RS scenario with the excitation or a KK state mass of the order of TeV.

If we denote a part of the KK 5D wave function, often called a profile, as  $f_X^{(n)}(\phi)$ , where  $n$  is referred to the KK<sup>*th*</sup> mode, then the graviton 4D profile wave-function can be expressed as  $h_{\mu\nu}^{(n)}(x_\mu)(f_X^{(n)}(\phi))$  and the zero-th mode of this function would correspond to the graviton that is a gravity mediator. Its effective mass is of the order of TeV. The Lagrangian describing the interaction of the graviton with the SM fields is given then by

$$\mathcal{L}_{graviton} = -\frac{x_1 \tilde{k}}{m_G} h^{\mu\nu(1)} \times d_i T_{\mu\nu}^{(i)}, \quad (2.14)$$

where  $T_{\mu\nu}^{(i)}$  is a 4D canonical energy-momentum tensor [134] for the SM field  $i$  and  $d_i$  is an integral of the profiles of the SM fields and KK gravitons.  $\tilde{k}$  is a free parameter inversely proportional to the Planck mass and varies from 0.01 to 1 when  $M_{graviton}$  is from 100 to 1500 GeV.

For radion the Lagrangian is similar and is given by:

$$\mathcal{L}_{radion} = -\frac{r}{\Lambda_R} \times a_i T_\mu^{\mu(i)}, \quad (2.15)$$

where  $\Lambda_R$  is a scale parameter proportional to the Planck mass and  $r$  is a 5D Radion

field. If we make an assumption that the profiles of the graviton and radion are localised at the TeV scale, then the coupling of them to the massive SM fields is of the order of 1. Throughout this thesis, theory curves contain model results for the case  $\tilde{k} = 0.1$  and  $\Lambda_R = 3$  TeV.

In this analysis the gravitons/radions in the search are expected to be produced by a gluon fusion mechanism. Five Feynman diagrams describe this process, two of which are present in the SM (a "box" and a "triangular" diagrams on Fig. 2.2), and the other three are a BSM extension of the SM (BSM contact interaction diagrams on Fig. 2.4).

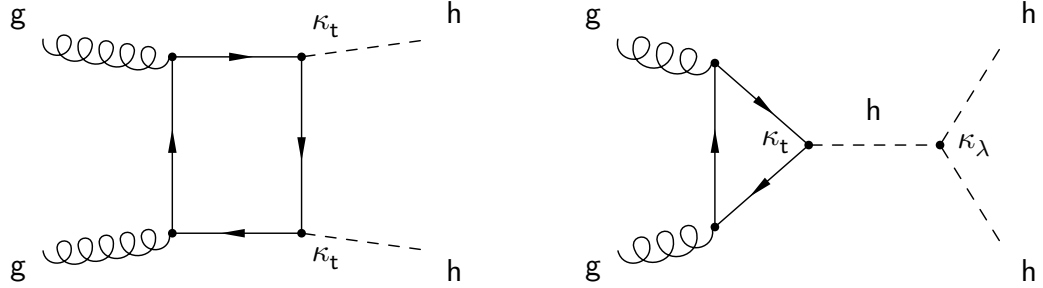


**Figure 2.2:** SM double Higgs boson production.

In the SM two main diagrams interfere destructively and the total cross section is thus lowered (Fig. 2.3 on the right). The box diagrams dominates the double Higgs boson production and peaks near 400 GeV. An extensive study has been performed by theorist for the future 100 TeV collider [?, 135]. However, since the kinematic distribution of the double Higgs mass remains to a high degree unchanged between 13 and 100 TeV (see Fig. 2.3 on the left), we can extrapolate 100 TeV results to those available at the current LHC machine energy. Fig. 2.3 has "nl" term, which denotes the contribution from the new non-linear  $t\bar{t}HH$  interaction if this new coupling exists

[136].

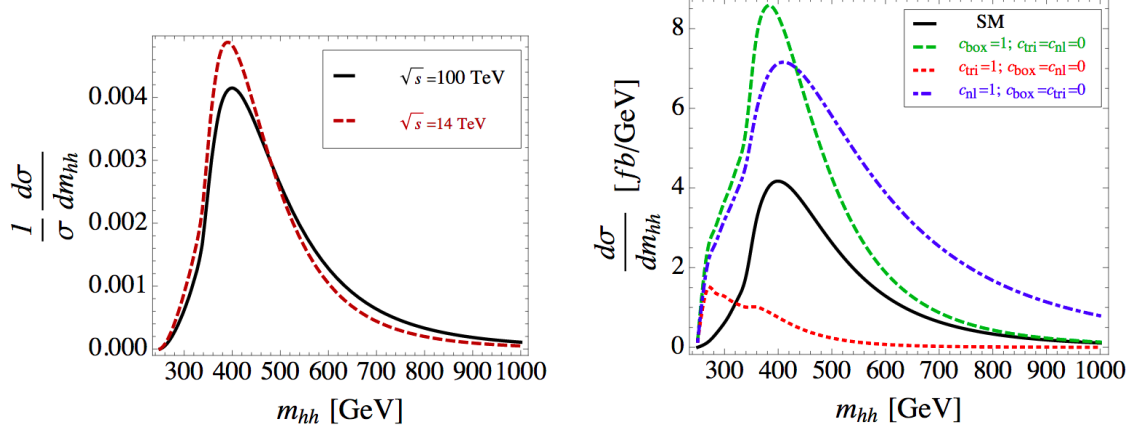


**Figure 2.3:** Left: comparison of the double Higgs boson mass distribution at the LO at 14 and 100 TeV center-of-mass energy, Right: the total SM HH cross section and the box and the triangular contributions ("box" and "tri" at the plots).

It is also interesting to measure BSM contact interaction couplings and a future non-resonant version of this analysis will target that. In this case,  $c_2$ , the coupling of two heavy quarks with two Higgs bosons,  $c_{2g}$ , the coupling of two gluons with two Higgs bosons, and  $c_g$ , the direct coupling of the gluons to the Higgs boson will be studied (see Fig. 2.4).

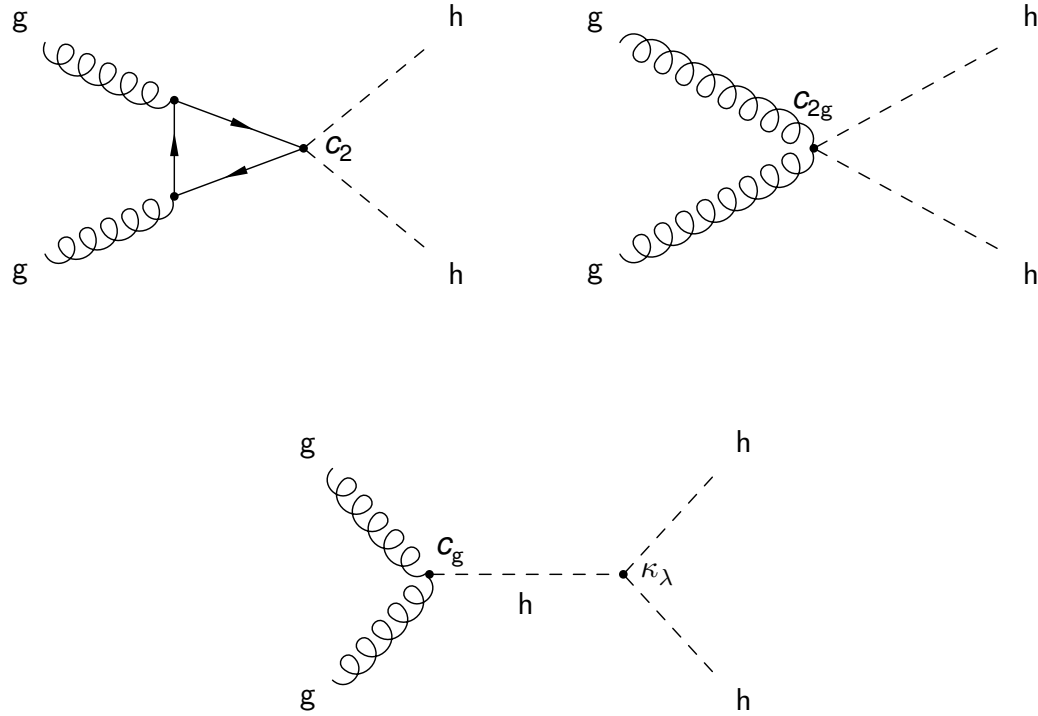


**Figure 2.4:** BSM double Higgs boson production.

Now it is time to discuss the decay of the double Higgs system. This analysis considers separately graviton and radion decays into two SM Higgs bosons with the subsequent decays of one Higgs boson to a pair of b quarks, and the other Higgs boson to W or Z boson pairs. W bosons are allowed to decay only leptonically. For Z boson decays, the signature is characterised by the on-shell Z boson decaying into a lepton pair and the off-shell Z boson decaying to invisible (neutrinos)(see Fig. 2.5).

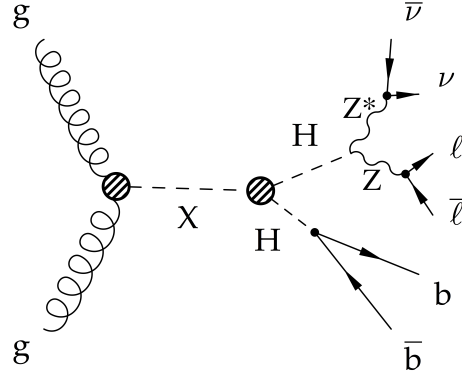


**Figure 2.5:** Double Higgs decay in the 2 b, 2 lepton, and 2 neutrino final state.

Before we finish this chapter, it is instructive to show all the decay channels of the double Higgs system to the SM particles, which is summarised in the Fig. 2.6. This thesis explores the branching fraction of the double Higgs boson decay through  $bbZZ$  in the two b quarks, two leptons, and two neutrinos final state, which equals approximately 2.8%.

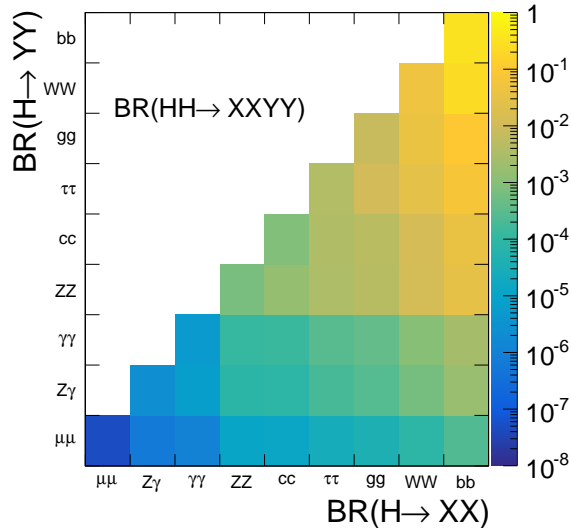


**Figure 2.6:** Double Higgs decay channels according to the SM branching fractions.

## CHAPTER 3

---

### **LHC and the CMS experiment**

---

#### **3.1 Introduction**

Large Hadron Collider (LHC) (see Fig. 3.1) is the most powerful particle accelerator that has ever been built. It is located at the border of the France and Switzerland, reutilising the tunnel used previously by the Large Electron Positron collider. The whole LHC story begins in 1977, when CERN director general Sir John Adams suggested that LEP tunnel can be reused to accommodate the future hadron collider of more than 3 TeV energies ???. At the 1984 ECFA-CERN workshop on a "Large Hadron Collider in the LEP Tunnel" ??, the plans for LHC were stated, where the primary ones were the BEH mechanism, Higgs boson, and the origin of masses of W and Z bosons. The parameters of the LHC machine were very ambitious: the centre-of-mass energy of 10 to 20 TeV, and a target luminosity of  $10^{33-34} \frac{1}{cm^2 s}$ . Luminosity is the coefficient which relates the cross section of the event under study to the number of events that will be generated in the LHC collision:  $N_{events} = L\sigma_{event}$ . Luminosity is the parameter control by the machine and for Gaussian beams ?? can be written as:

$$L = \frac{N_b^2 n_b f_{rev} \gamma_r}{4\pi \epsilon_n \beta^*} F$$

where  $N_b$  is the number of particle in the colliding bunch,  $n_b$  is the number of colliding

bunches in the beam,  $f_{rev}$  is the revolution frequency,  $\gamma_r$  is the relativistic factor,  $\varepsilon_n$  is the normalised transverse beam emittance,  $\beta^*$  is the beta function at the collision point, and  $F$  is the factor related to the crossing angle at the interaction point (IP). The luminosity is not constant and decays with time due to the degradation of the initial circulating beams. Decay time is approximately 45 h, and 29 h to reach  $1/e$  level. Adding contribution from the intrabeam scattering, scattering on the residual gas, etc, the final luminosity lifetime is about 15 h.

Another useful variation of the luminosity parameter is an integrated luminosity. Integrating over the yield of a single run we get:

$$L_{int} = L_0 \tau_L \left[ 1 - e^{-\frac{T_{run}}{\tau_L}} \right],$$

where  $L_0$  is the initial luminosity,  $T_L$  is the total length of the run, and  $\tau_L$  is the luminosity lifetime. The optimum runtime thus is either 5.5 or 12 hours, which potentially leads to  $80 - 120/fb$  of data with barn  $b$  denoting a unit area of  $10^{28} m^2$ .

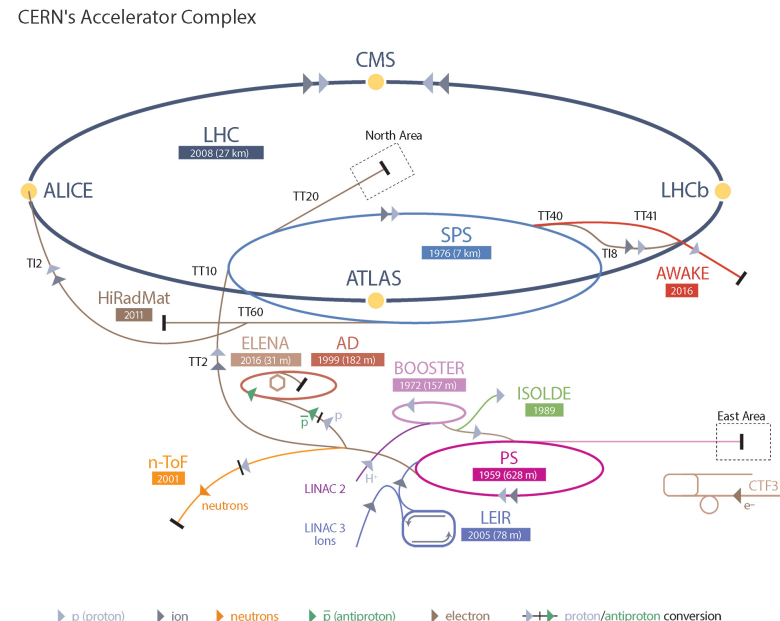
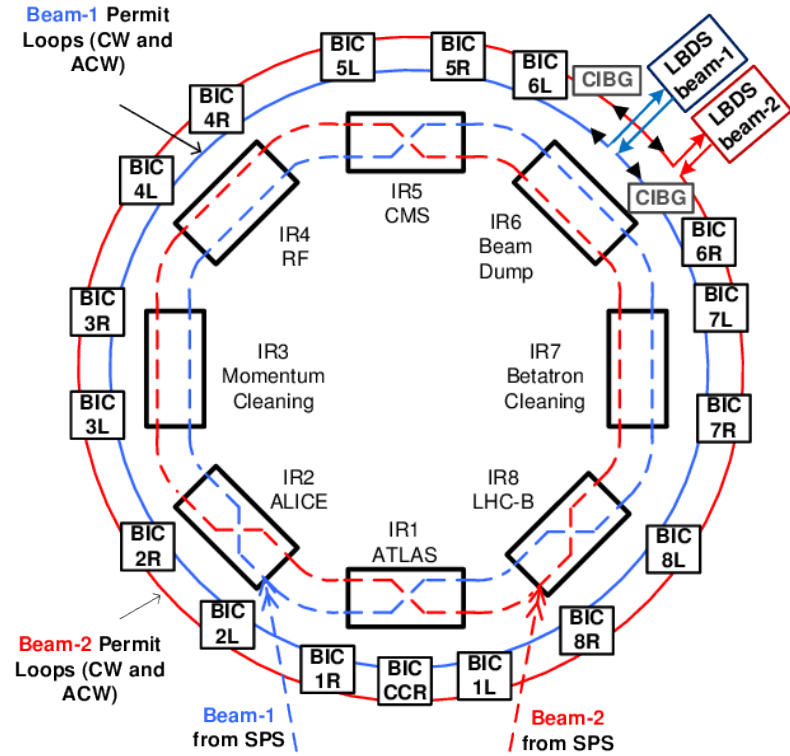


**Figure 3.1:** Schematic layout of the LHC.

## 3.2 The LHC

The first LHC budget plan was approved in 1996 and the final cost sum was completed in 2008. 4 years later the Higgs discovery happened, in 2012, quite fast for such a huge project! Now we will talk about the most important parts of the LHC complex one-by-one. Let us start with magnets.

### 3.2.1 The Magnets

To keep the beam of protons on a circular orbit LHC needs strong magnets. The proven technology existed since Tevatron and relied on  $NbTi$  superconductors. 1232 dipoles at  $8\text{ }T$ , which are cooled to the below  $2\text{ }K$  temperature using superfluid Helium, bend the beam 3.2. The dipole cold mass is in the so-called Helium bath and is cooled down to  $1.9\text{ }K$ . Each of the  $16.5\text{ }m$  (with ancillaries) long and  $570\text{ }mm$  in diameter dipoles is slightly curved by  $5.1\text{ }mrad$  to help a chain of dipoles complete 360 degrees. The dipole is located inside of the dipole cryostat, which is a long cylindrical tube  $914\text{ }mm$  in diameter made of low-carbon steel. During the standard operation time the vessel contains the vacuum.

## LHC DIPOLE : STANDARD CROSS SECTION

CERN AC/DI/MM - HE107 - 30 04 1999

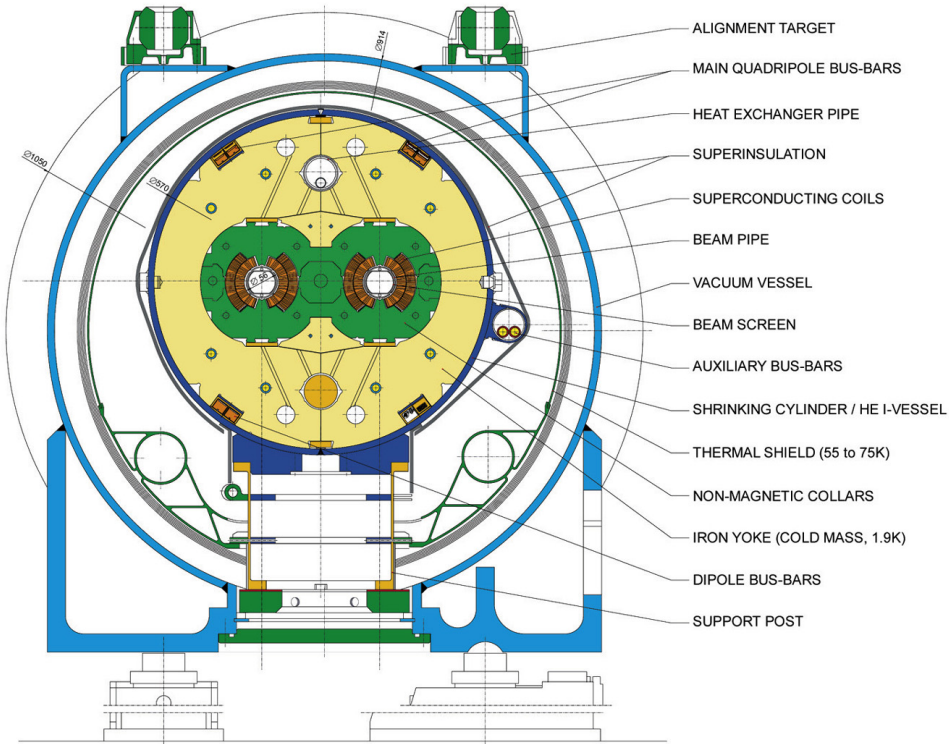


**Figure 3.2:** The cross section of the LHC dipole.

The material and the properties of the cables for the dipoles had to be carefully chosen. Each dipole coil is 56 mm in diameter and is made of cables of two types. The cable in the inner layer contains 28 strands 1.065 mm each. The outer layer contains 36 strands 0.825 mm each 3.3.

To correct the orbit, higher order correctors are used with about 3800 single aperture and 1000 twin aperture magnets evenly spaces around the circular trajectory.

Another important task that is performed with the use of magnets is the beam insertion, which is done at eight specific insertion locations. LHC also uses *NbTi* magnets to accomplish this work.

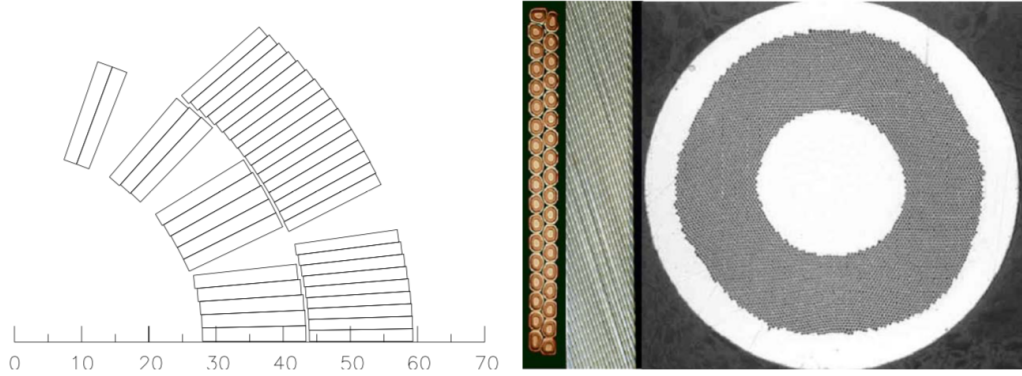


**Figure 3.3:** Cables of the dipole magnet. Left: cross section view. Right: Strand and cables

### 3.2.2 Radio Frequency System

The beam that comes from injectors will be placed, accelerated and kept on the orbit with the help of Radio Frequency (RF) cavities (see Fig. 3.4). The same system will be used to correct for injection errors in the beam direction. RF will be operating at the  $400\text{ MHz}$ , which is 10 times more than the revolution frequency of  $40\text{ MHz}$ .

Four RF cavities grouped together into one cryomodule constitute an important accelerating module. If something happens to this module, it can be easily replaced in short period of time.

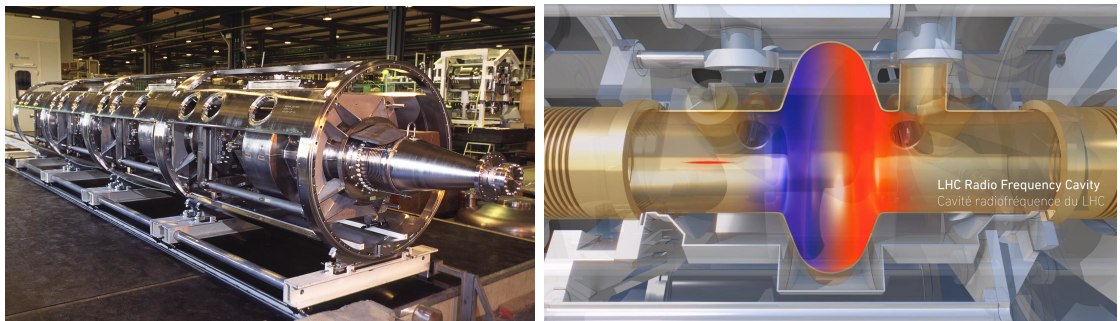


**Figure 3.4:** LHC RF cavities. Left: a cryomodule with four RF cavities. Right: a single RF cavity schematic drawing. The colour field is used to highlight the fact of two field of the different polarity.

### 3.2.3 Vacuum System

Three types of vacuum systems are necessary for the LHC proper operation. The vacuum system for the cryomagnets, the insulation vacuum for helium distribution, and, of course, the vacuum for the beam (VBS). As a convention, taking into account ionisation cross sections for gasses of the interests, cryogenic temperatures are expressed as corresponding gas densities normalised to the hydrogen. VBS, to ensure the 100 hours long run time, requires the equivalent hydrogen densities (EHD) to be below  $10^{15} H_2 \frac{1}{m^3}$ . To minimise the backgrounds from the experiments, the EHD at the interaction points should be  $10^{13} H_2 \frac{1}{m^3}$ . Those parts of the beam system, which operate under room temperatures, are under the pressure of  $10^{-10}$  to  $10^{-11}$  mbar. All the vacuum section are subdivided into smaller modules to allow easy repair and fine tuning. VBS, as the most demanding in terms of the vacuum quality, have to be properly designed and must address a number of challenges, such as synchrotron radiation that significantly affects vacuum chambers in the arcs around the tunnel, as well as an electron cloud effect which exists along the length of the whole circle of the LHC. After the beam is inserted and is stabilised, the final adjustment of the VBS is needed to guarantee the perfect performance.

To finish the discussion of the VBS, let us discuss which heat sources have the main effect on the vacuum of the beam that must exist at the 1.9 K.

- Synchrotron radiation ( $0.2 W/m$  per beam)
- Energy loss by nuclear scattering ( $30 mW/m$  per beam)
- Image currents ( $0.2 W/m$  per beam)
- Electron cloud related effects (vary)

To obstruct the heat sources mentioned above, specific beam screens are developed (see Fig. 3.5). Screens have elliptical shape, so-called racetrack shape, which gives extra space for cooling while optimises the aperture. Finally, the lifetime of the vacuum is mostly determined by the interactions of the vacuum gas nuclei with the protons of the beam. Values of the cross sections of such processes are given in ??.

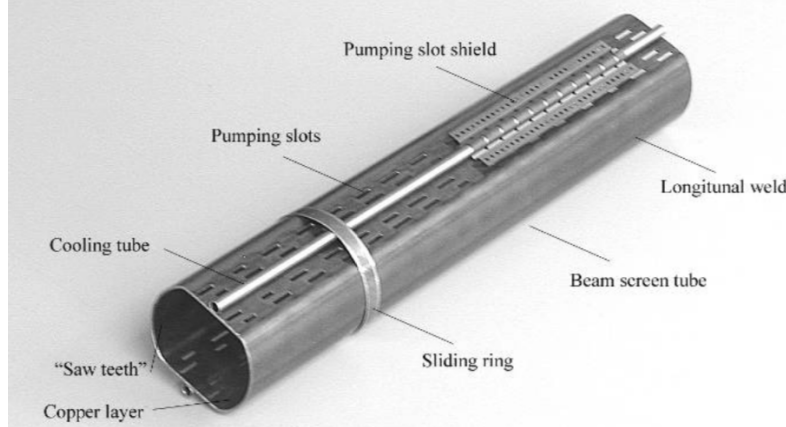


**Figure 3.5:** Beam screen.

### 3.2.4 Powering

To power the LHC, 1612 electrical circuits of 131 types are used. The magnets are powered in eight symmetrical sections. Some sections rely on all 131 types of circuits, while others may use only specific ones. To power the main quadrupoles which focus the beam, the power converters are located in the underground area. A total of 3286 current leads is needed to connect all the circuits and power cables. 1070 of the leads operate between 600 A and 13 kA (see Fig. 3.6). The other leads work in the range 60 to 120 A.



**Figure 3.6:** 13 kA high-temperature superconducting current lead.

### 3.2.5 Cryogenic system

The cryogenic system (see Fig. 3.7) must supply the LHC cold mass of 37 Mkg within 15 days with the necessary temperature settings and work with the temperatures different by 75 K. The system must also be able to deal with the fast pressure raises and flow surges, and should be able to recover in a short period of time from such perturbations not to affect the run of the whole LHC. Another important point during the cryogenic design that had to be addressed is the fact that the LHC tunnel is

inclined in the horizontal plane by 1.41 °. This equals to 120 m difference in the vertical location of two diametrically opposite points of the tunnel with respect to the surface level and results in the additional hydrostatic pressure that can affect the flow of the cryogen. To avoid any instability of the LHC work like this, the gas is transported in the super-heated-vapour state.

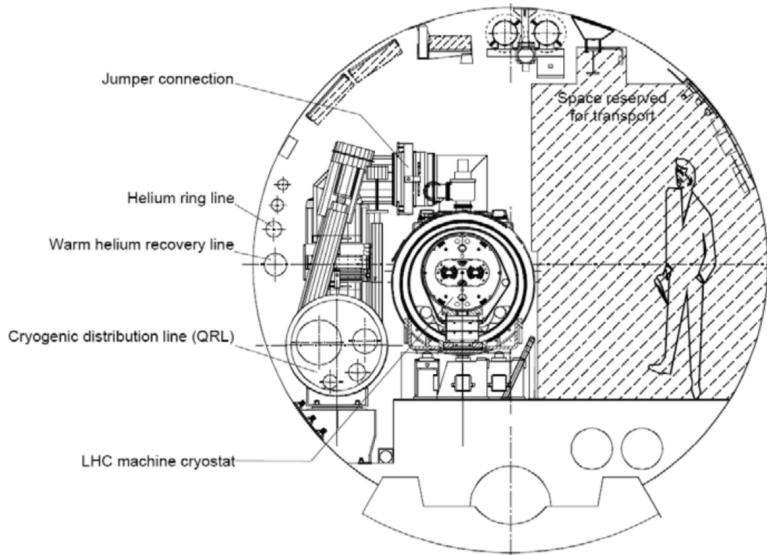


**Figure 3.7:** Cross section of the LHC tunnel

Since the cost of the production of 1.8 K temperature is high, several temperature levels are employed (see Fig. 3.8):

- 50 to 75 K for the thermal shielding that protects the cold masses
- 4.6 to 20 K for lower temperature interception and to cool the beam screens
- 1.9 K for quasi-isothermal helium in the superfluid state to cool the magnet cold mass
- 4 K for the transportation system that directs the 1.8 K helium from the exchanger to the 1.8 K refrigerator

- 4.5 K for RF cavities and lower sections of the high-temperature superconducting current leads
- 20 to 300 K for upper sections of the high-temperature superconducting current leads

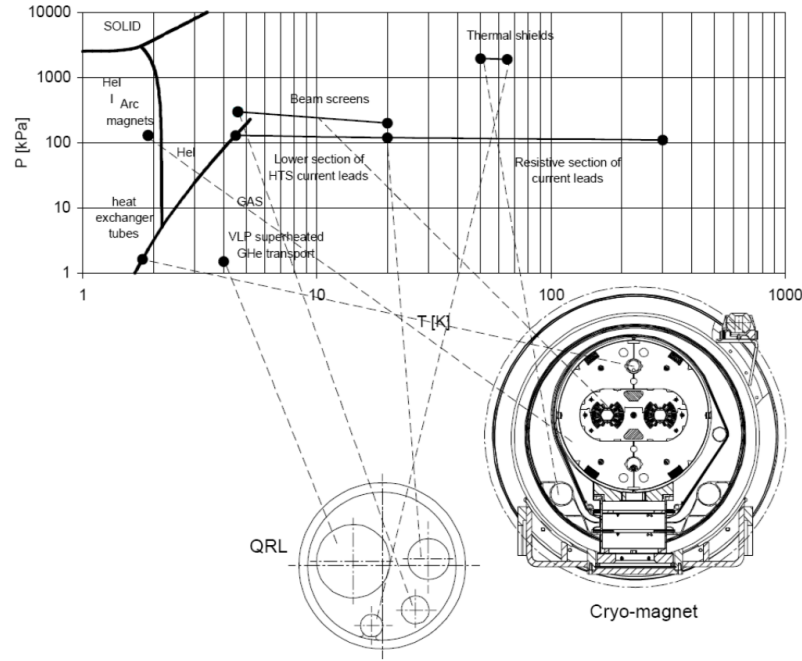


**Figure 3.8:** LHC cryogenic states and the temperature scale.

### 3.2.6 Beam dumping system

The LHC beam carries a lot of power and a well-designed and reliable beam extraction and dumping system is needed. Point 6 at LHC contains such system, which is able to fast-extract the beam in a loss-free way. The system for each ring comprises:

- 15 kicker magnets for extraction
- 15 steel septum magnets around the Point 6 interaction point
- 10 modules of the dilution kicker magnets

- the beam dump proper with the associated steel and concrete for shielding
- dedicated dilution devices

### **3.2.7 Beam injection system**

The injection at LHC is done at two points and for two beams separately: at Point 2 and Point 8. The beam comes to the insertion point from outside and below the machine level. A series of magnets and a kicker then deflects the beam horizontally and vertically to place the beam on the LHC orbit. To protect against the problematic injections and malfunctioning of the kickers, a series of the collimators correct the incoming beam.

### **3.2.8 LHC injection chain**

To place the beam at the final LHC orbit, the protons from the hydrogen bottle extracted from the hydrogen gas have to travel a long pass during which they are put into bunches and accelerated to the nominal collision speed.

### The LHC injection complex

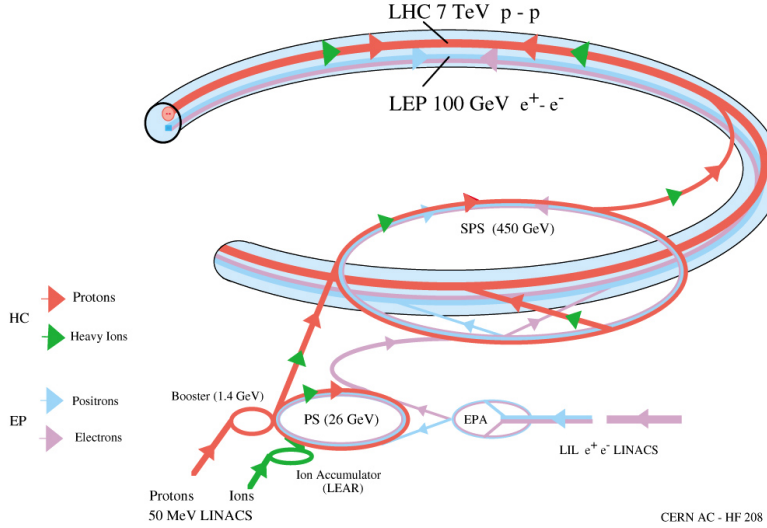


**Figure 3.9:** LHC injection complex.

The accelerator complex consists of: LINAC, Booster, Proton Synchrotron, Super Proton Synchrotron, and finally, the LHC main ring (see Fig. 3.9).

The whole LHC complex has to satisfy requirements of the final ring, such as:

- the beam emittance has to be compatible with the small aperture of the LHC superconducting magnets
- the effect of the synchrotron radiation has to be taken into account when calculating the required cryogen needs for the intensity of the incoming beam
- the beam-beam interactions that enhance the betatron oscillations
- in the injector the space-charge limits have to be taken into account

### 3.3 The CMS experiment

The total inelastic cross section of the proton-proton interaction at  $\sqrt{s} = 14$  TeV will be about 100 mb. The detectors observe the event rate of nearly  $10^9$  inelastic

events per second. This flow of data is too large to be stored, and also, does not contain that many event of interest. Therefore, the trigger system must reduce the event rate to manageable 100 events per second. In addition, a pile up (PU) of 20-200 events overlaid with the event of interest will be expected, which results in about 1000 particles produced every 25 ns. All sub-detectors of CMS (see Fig. 3.10), thus, have to be able to work fast and in a good synchronisation with each other.

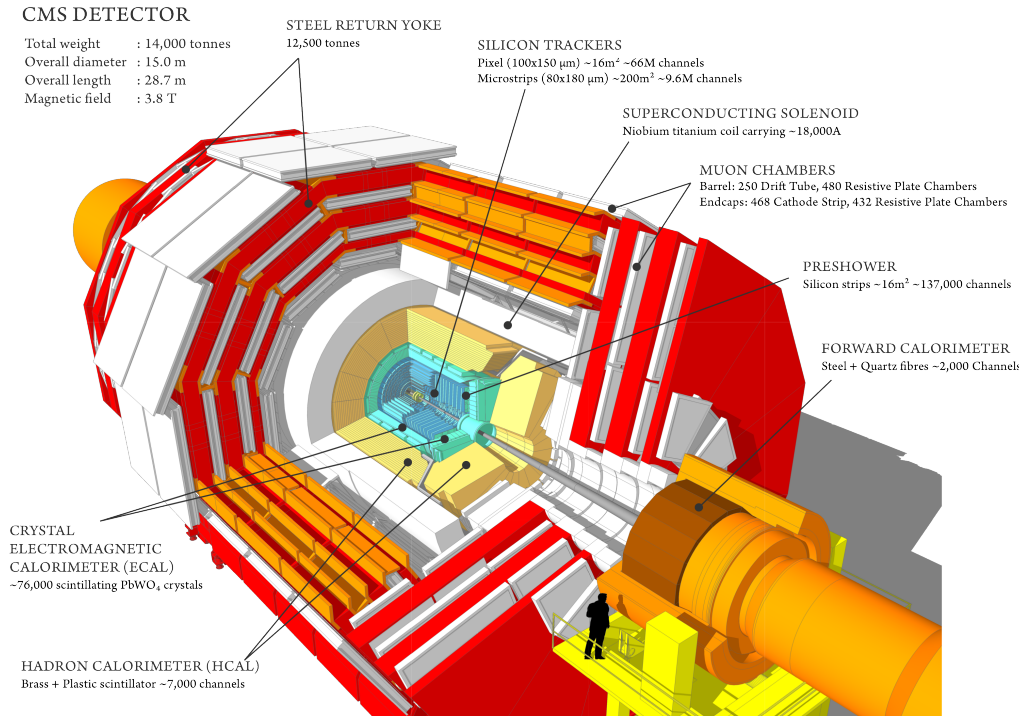


**Figure 3.10:** CMS experiment with all sub-detectors shown.

### 3.3.1 The CMS challenging environment

One can summarise all challenges and requirements that the CMS has faced in the following list:

- good muon momentum resolution over the momentum scale covering almost a TeV range, good dimuon resolution at the 100 GeV, and a capability to de-

termine correctly the charge of the highly energetic muon all the way up to 1 TeV

- good momentum resolution of the charged particles in the inner tracker. Emphasis on the efficient  $\tau$  lepton and b-jets reconstruction
- good performance of the electromagnetic calorimeter (ECAL), with the particular attention to the diphoton mass resolution, ability to reject efficiently  $\pi^0$ , ability to identify isolated photons and leptons
- good missing transverse mass and dijet-mass resolution, which depends heavily on the performance of the hadronic calorimeter (HCAL)

The CMS design has been driven by the needs to have a large bending power, which is to be provided by the superconducting magnet, to be able to disentangle among each other various charged particles. The size of the magnet is 13 m in length and 6 m in inner diameter. 4 T solenoid provides 12 Tm bending power. The inner diameter is large enough to host the inner tracker and the ECAL. To address the high multiplicity problem, the CMS inner tracker uses 10 layers of the silicon microstrip detectors. The inner barrel contains four layers of strips and the outer barrel has six layers. Each silicon sensor is  $320 \mu m$  in height and a specifically designed overlay of strips provides a spatial resolution of  $13\text{-}38 \mu m$ . About the same resolution is achieved by the other tracker. The whole tracker contains 15148 silicon modules with the 9.3 million strips. Tracker provides the experiments with the tracks information left by the charged particles traversing its material.

To further improve the impact parameter determination and secondary vertex reconstruction, three layers of the silicon pixel detector are inserted near the interaction

region. Pixel detector is composed of 1440 silicon pixel detector modules organised in three concentric cylindrical layers, and also two disks in the forward regions.

The ECAL technology is based on the on the lead tungstate crystals ( $PbWO_4$ ). The ECAL measures the energy deposited by photons and electrons. ECAL contains 75848 crystals where the energy showers will be produced by the particles releasing their energy when interacting with the material of the crystals. Before the ECAL, a preshower system is placed to reject  $\pi^0$ . It contains layers of lead radiators followed by layers of the silicon strips to initiate and subsequently to measure the energy of the particle. The ECAL measured energy of the particles is a function of the stochastic term (S), noise (N), and a constant term (C).

$$\left(\frac{\sigma}{E}\right)^2 = \left(\frac{S}{\sqrt{E}}\right)^2 + \left(\frac{N}{E}\right)^2 + C^2 \quad (3.1)$$

The ECAL is surrounded by the HCAL system which is based on the brass/scintillator sampling hadronic technology. HCAL measures energy of particles made of quarks. Central part is later covered by the *tail-catcher* leaving 11 hadronic interaction lengths to the particle interactions. Further, the forward calorimeter is used to ensure the coverage in  $\eta$  up to 5. Note, that the coverage of ECAL and HCAL are about up to  $\eta = 3$ .

Additional dedicated detectors such as CASTOR, ZDC, etc, ensure that the detector has a full  $4\pi$  coverage. HCAL does not fully absorb energy of the the particles traversing its medium, except very low energy particles, thus the energy of the particles is sampled to estimate the total amount.

Overall, the CMS detector is 21.6 m in length and 14.6 m in diameter. The weight of the whole construction is near 12 500 tons. ECAL covers more than 25 radiation lengths, HCAL, from 7 to 11, depending on the  $\eta$  region. Outer HCAL is located

outside of the magnet.

The superconducting magnet of CMS provides the experiment with almost 4 T magnetic field and is operated at the 4.7 K temperature. Additionally, a magnet yoke is made of five barrel wheels is used for the magnetic flux return and serves as a support for the embedded muon system, which is located outside of the ECAL and HCAL systems. Muons are energetic enough to traverse the ECAL and leave the detector. Tracks in the muon system will be used to reconstruct standalone muons, and in combination with the tracker, to reconstruct the global muons.

### 3.3.2 CMS coordinate system

It is useful to introduced a convenient coordinates system used by the CMS experiment. We will use rapidity and pseudorapidity many times in the analysis section of the thesis. The coordinate system employed by the CMS uses the rapidity,  $y$ , and pseudorapidity,  $\eta$ . They are derivatives of the log functions of the energy and a projection of the momentum on the  $z$  axis and the angle  $\theta$  with respect to the beam axis (see Fig. 3.11 ??):

$$y = \frac{1}{2} \ln \frac{E + p_z}{E - p_z} \quad \eta = -\ln \left( \tan \frac{\theta}{2} \right) \quad (3.2)$$

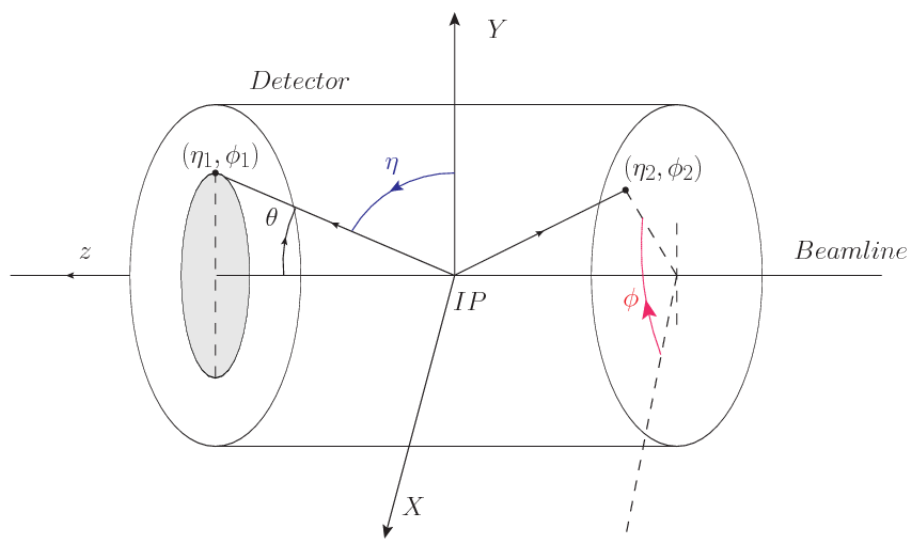


**Figure 3.11:** Coordinate system of the CMS detector.

## CHAPTER 4

---

### Analysis overview

---

In 2012, CMS [77] and ATLAS [78] collaborations officially discovered a Higgs-like particle and with that breakthrough the picture of the SM [20, 70, 71] of the particle physics has been completed. Most of the basic properties of the Higgs boson have been measured. However, it remains difficult to distinguish several processes with very low cross sections from the irreducible SM background processes with a similar signature. One such important but rare process is a double Higgs (HH) boson production. HH directly relates to the Higgs boson self-coupling, and thus, has an access to the shape of the Higgs boson potential. In the SM, HH production is a non-resonant process with a cross section of  $\sigma = \text{fb}$  [79] at  $\sqrt{s} = 13$  TeV.

Several Beyond the Standard Model (BSM) theories and models, such as supersymmetry, composite Higgs, Warped Extra Dimensions (WED) [33, 60, 62, 63, 75], predict scenarios when the double Higgs boson cross section is significantly increased and may be observed with the current data. There may be two different types of the BSM HH production: a non-resonant production, introducing BSM terms to the SM lagrangian or a resonant production, in which the process is mediated by a narrow width heavy mass resonance that subsequently would decay to SM Higgs bosons. [75].

In this analysis through the gluon fusion mechanism a heavy narrow resonance, such as RS1 KK graviton or RS1 radion ("graviton" or "radion" later in the text) [64–66] is produced. It decays to two Higgs bosons, which further decay to the  $b\bar{b}$  pair (the first Higgs boson) and the ZZ/WW pair (the other Higgs boson). The analysis covers masses of graviton/radion from 250 GeV to 1000 GeV. Since no evidence of the signal has been reported by the previous HH analyses, we proceed directly to setting 95 % upper confidence limits on the production of the graviton with a subsequent decay to Higgs bosons times the branching ratios of the Higgs boson decaying to a pair of  $b$  quarks and the other Higgs boson to two leptons and two neutrinos respectively (Fig. 4.1). We observe no deviation with the given data and evaluated uncertainties, the results are compatible with the Standard Model.

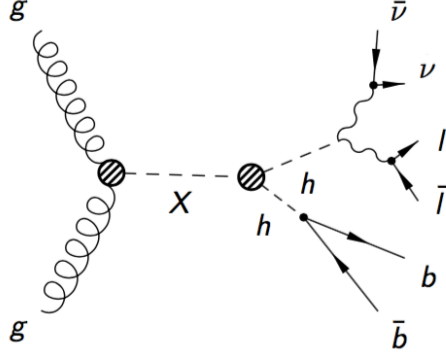


**Figure 4.1:** The Feynman diagram of the graviton/radion production with the subsequent decay to HH. HH system decays to a pair of  $b$  quarks and Z bosons. Shown is 2  $b$  quarks, 2 leptons, and 2 neutrinos final state.

## 4.1 Analysis Strategy

The analysis is based on ntuples and object selection from the approved VHbb sister analysis [?]. Leptons,  $b$  jets, and the missing transverse energy (MET) are reconstructed using the standard CMS procedures [74] and the Particle Flow (PF) algo-

rithm [73]. b-jets are identified using the Combined MVA v2 (CMVA) algorithm [68]. Then, on shell Z boson candidates are selected of dilepton pairs of the same flavour with a net charge zero for a pair. Higgs boson candidate decaying to b quarks ( $Hbb$ ) is reconstructed as a pair of b jets with the highest CMVA output value. Finally, double Higgs boson pseudo-transverse mass, which is used in the shape analysis to extract limits, is constructed computing the transverse mass of the sum of the Lorentz vectors of the two leptons forming the on-shell Z, MET, and a pair of the b jets forming the  $H \rightarrow b\bar{b}$ . Additionally, a cut on the missing transverse energy is introduced to preserves the orthogonality with the existing HIG-18-013 “2b 2l 2q” analysis, which also works with the  $bbZZ$  decays. In a similar fashion, the cut on the Z mass ( $m_Z > 76$  GeV) is used to orthogonalise the analysis with respect to the HH phase space used in the legacy  $bbWW$  analysis where the final signature is identical to ours. Lastly, the cut on the BDT is used to reduce the background contamination in the signal region.

Main backgrounds are  $t\bar{t}$  and Drell-Yan in association with jets. To determine their normalization, we construct two dedicated control region, which are correspondingly  $t\bar{t}$  and Drell-Yan dominated. Then, during the simultaneous fit of signal region (SR), as well as control region  $t\bar{t}$  (CRTT), and control region Drell-Yan (CRDY), we obtain rates for these processes. Others, minor backgrounds, are single top production, diboson samples (WW, WZ, ZZ), and ZH production and are determined from the Monte Carlo (MC) simulation.

In the next chapters we will discuss all of the aspects of the analysis in details starting with the chapter on Data.

## CHAPTER 5

---

### Data and Triggers

---

## 5.1 Data

This measurement uses the full dataset of 2016 collected with the CMS detector in pp collisions at 13 TeV center-of-mass energy with the corresponding integrated luminosity of  $35.9 \text{ fb}^{-1}$ .

As the measurement is based on dilepton signatures, the DoubleMuon and DoubleElectron primary datasets are analyzed and only on-shell  $Z(\ell\ell)$  decays are considered, where  $\ell = e, \mu$ . CMS delivered data in several runs. The run periods and the corresponding integrated luminosities are listed in Table 5.1 for DoubleMuon channel, DoubleElectron channel numbers are similar.

**Table 5.1:** List of used 2016 DoubleMuon data sets. An uncertainty of 2.5% is assigned for the 2016 data set luminosity [101]

Dataset	$\int \mathcal{L} (\text{fb}^{-1})$
DoubleMuon_Run2016B-03Feb2017-v2	$\sim 5.9$
DoubleMuon_Run2016C-03Feb2017-v1	$\sim 2.7$
DoubleMuon_Run2016D-03Feb2017-v1	$\sim 4.3$
DoubleMuon_Run2016E-03Feb2017-v1	$\sim 4.1$
DoubleMuon_Run2016F-03Feb2017-v1	$\sim 3.2$
DoubleMuon_Run2016G-03Feb2017-v1	$\sim 3.8$
DoubleMuon_Run2016H-03Feb2017-v1	$\sim 11.8$
Total Lumi	35.9

## 5.2 Triggers

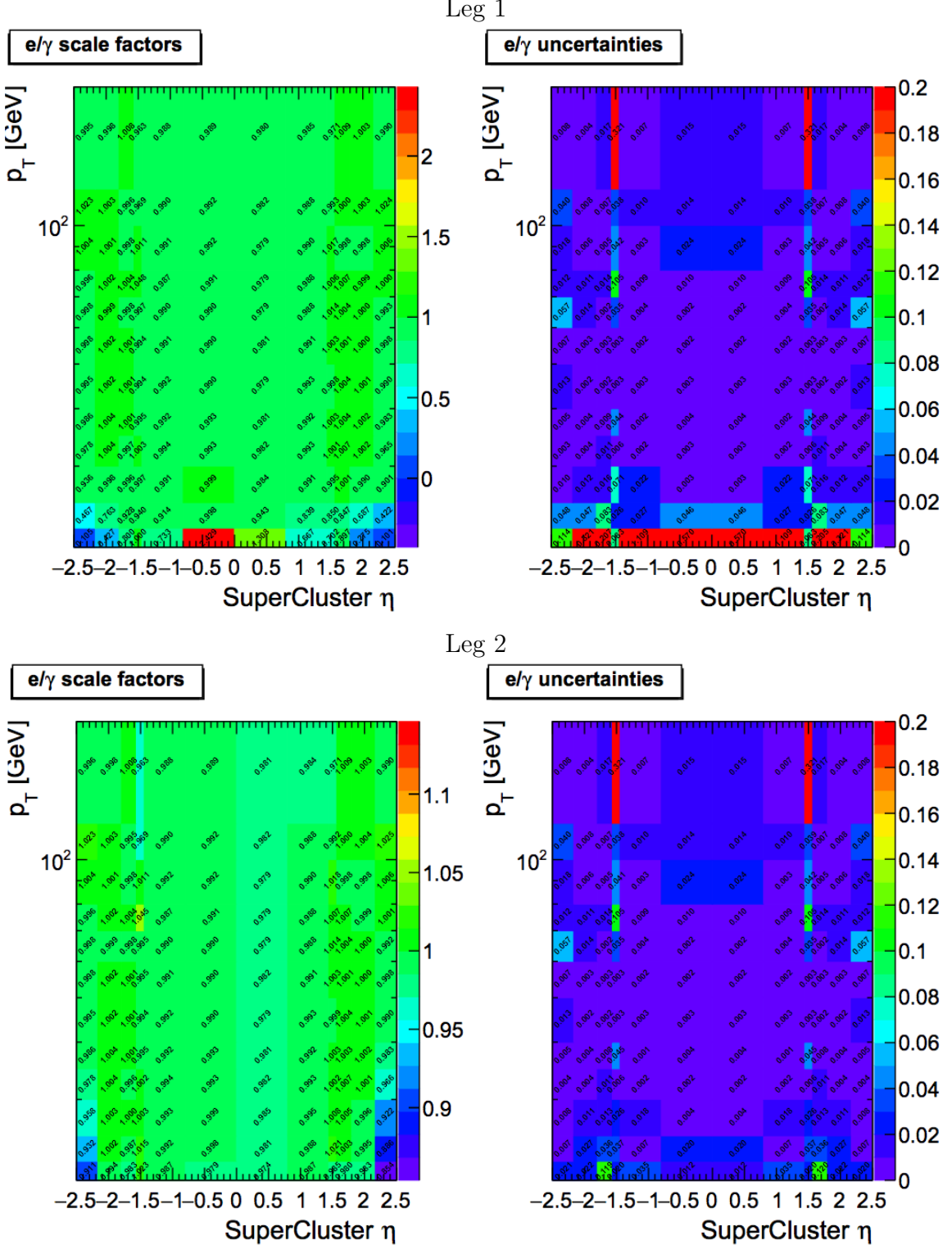
The rate at which particles are produced at LHC is not suitable for a direct persistence to the tape, it is too high and contains lots of uninteresting events. Therefore, we need a "trigger" that can select the potentially interesting events, such as those which will produce the Higgs particle or a Z/W boson, etc. In parallel, trigger also reduces the rate to just a few hundred "events" per second, which can be read out and stored on computer disk for subsequent offline analysis. Our  $bbZZ$  analysis is performed in the dielectron and dimuon channels, so low momentum events are important to us. That is why unprescaled dilepton triggers with the lowest available transverse momentum thresholds are utilised. The triggers at the level 1 (L1) and high level trigger (HLT) are listed in Table 5.2. Dielectron trigger requires the leading electron to pass 23 GeV  $p_T$  cut and the trailing (subleading) electron to pass 12 GeV  $p_T$  cut, both electrons should be within  $\eta < 2.5$ . Dimuon triggers require the leading muon to pass 17 GeV  $p_T$  cut and 8 GeV  $p_T$  cut for the subleading muon, both muons should be within  $\eta < 2.4$ . The  $\eta$  region (1.4442 to 1.566) in the gap between the barrel and endcap is excluded.

Due to the fact that there are discrepancies between trigger efficiencies in data and in simulation, we need trigger scale factors. Before measuring them, identification

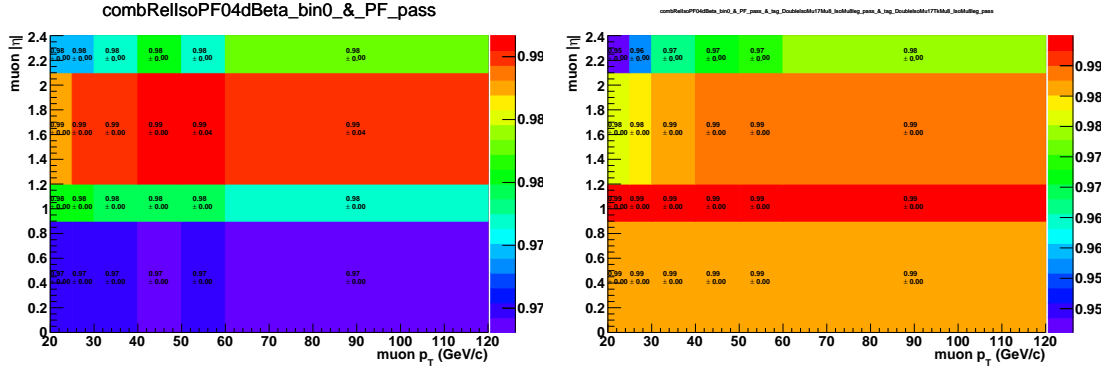
**Table 5.2:** Triggers for dimuon and dielectron analysis channels both at L1 and HLT levels.

Channel	L1 Seeds	HLT Paths
$Z(\mu\mu)$ $Z(\nu\nu)H \rightarrow b\bar{b}$	L1_SingleMu20	HLT_Mu17_TrkIsoVVL_Mu8_TrkIsoVVL_v* OR HLT_Mu17_TrkIsoVVL_TkMu8_TrkIsoVVL_v* OR HLT_Mu17_TrkIsoVVL_Mu8_TrkIsoVVL_DZ_v* OR HLT_Mu17_TrkIsoVVL_TkMu8_TrkIsoVVL_DZ_v*
$Z(ee)$ $Z(\nu\nu)H \rightarrow b\bar{b}$	L1_SingleEG30 OR L1_SingleIsoEG22er OR L1_SingleIsoEG24 OR L1_DoubleEG_15_10	HLT_Ele23_Ele12_CaloIdL_TrackIdL_IsoVL_DZ

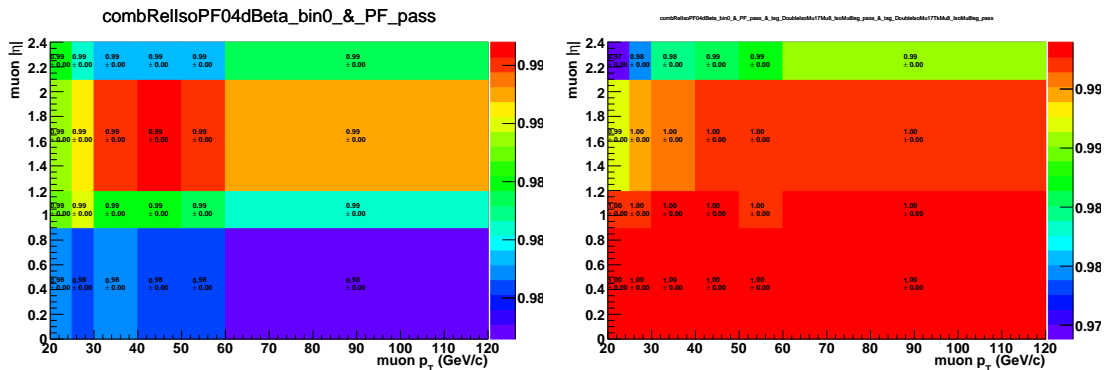
(ID) and isolation (ISO) cuts should be applied. Identification criteria helps selecting real prompt leptons, which isolation criteria stresses the fact that a track for the real prompt lepton should be isolated from the other activity nearby. Further,  $p_T$  cuts of the offline selection are replicated. For dielectron trigger leading and subleading electrons have to pass 25 GeV  $p_T$  cut and 15 GeV  $p_T$  cut correspondingly. Dimuon triggers require the leading muon to pass 20 GeV  $p_T$  cut and 15 GeV  $p_T$  cut for the subleading muon. Dilepton scale factor have been computed for each leg separately, since the cuts on each leg vary (Fig. 5.1). Following the recommendations from the Muon Particle Object Group (POG), scale factors have been computed separately for two groups: run H and other runs, and then the final scale factors are determined as luminosity averaged scale factors (Figs. 5.2, 5.3, 5.4). Muon ID, ISO, and electron ID+ISO scale factors are shown at Figs. 5.5, 5.6, 5.7.



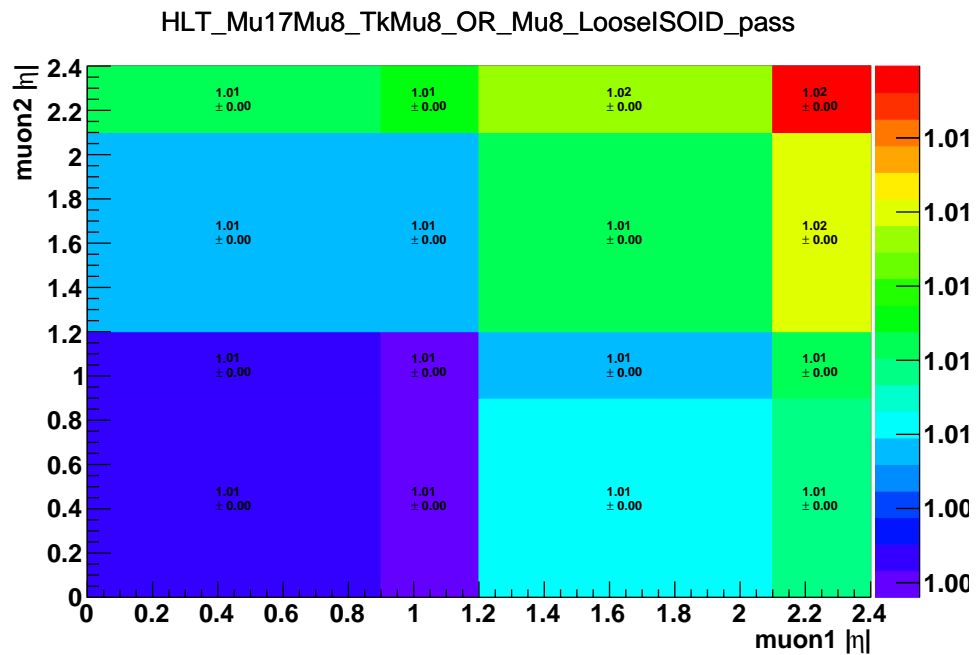
**Figure 5.1:** Electron scale factors in  $p_T$  and  $\eta$  bins for 2016 data set for the HLT\_Ele23\_Ele12\_CaloIdL\_TrackIdL\_IsoVL\_DZ trigger. ID cut (general purpose MVA WP90) and ISO cuts are applied, then the scale factors are measured. Taken from [110]



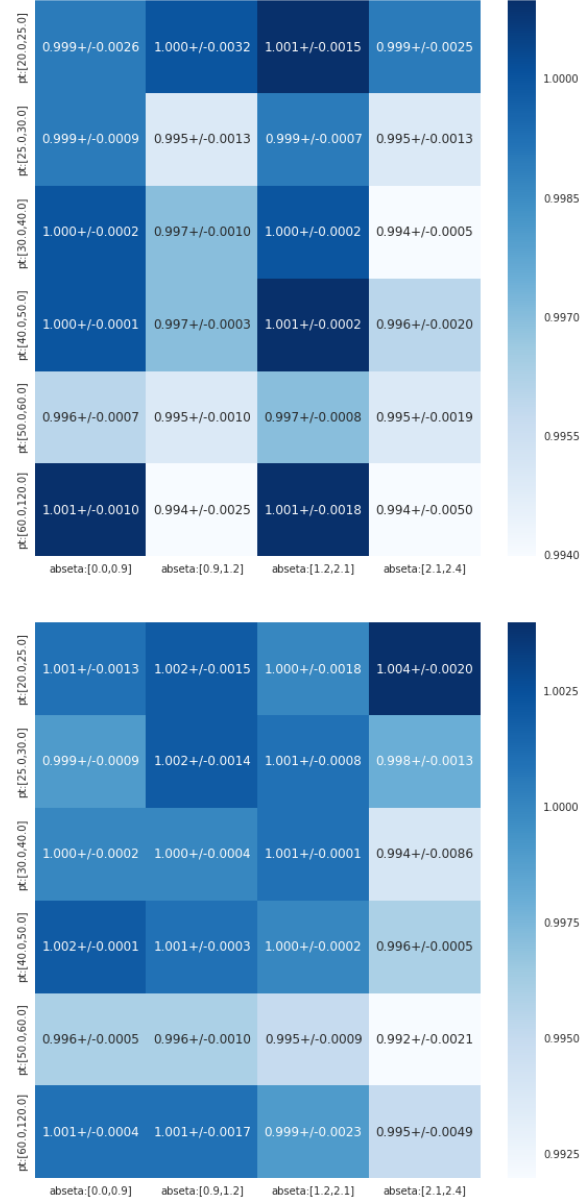
**Figure 5.2:** Muon scale factors in  $p_T$  and  $\eta$  bins for 2016 data runs B, C, D, E, F, G for the HLT\_Mu17\_TrkIsoVVL\_Mu8\_TrkIsoVVL\_v\* OR HLT\_Mu17\_TrkIsoVVL\_TkMu8\_TrkIsoVVL\_v\* triggers. Left: Scale factors for 8 GeV leg. Right: Scale factors for 17 GeV leg, provided that the subleading leg passed 8 GeV cut.



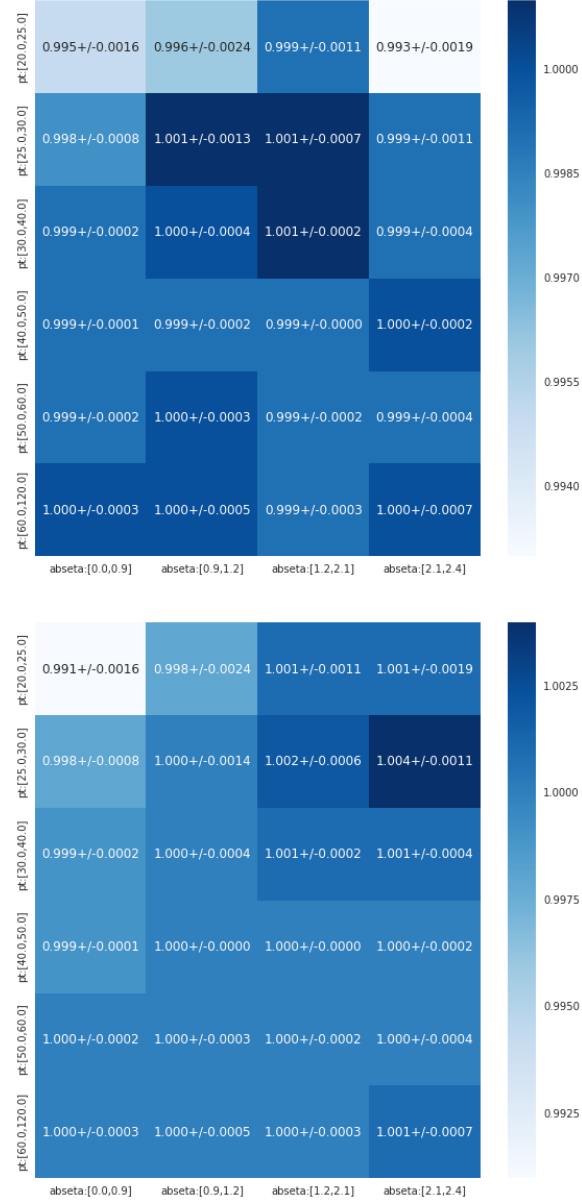
**Figure 5.3:** Muon scale factors in  $p_T$  and  $\eta$  bins for 2016 data run H for the HLT\_Mu17\_TrkIsoVVL\_Mu8\_TrkIsoVVL\_v\* OR HLT\_Mu17\_TrkIsoVVL\_TkMu8\_TrkIsoVVL\_v\* triggers. Left: Scale factors for 8 GeV leg. Right: Scale factors for 17 GeV leg, provided that the subleading leg passed 8 GeV cut.



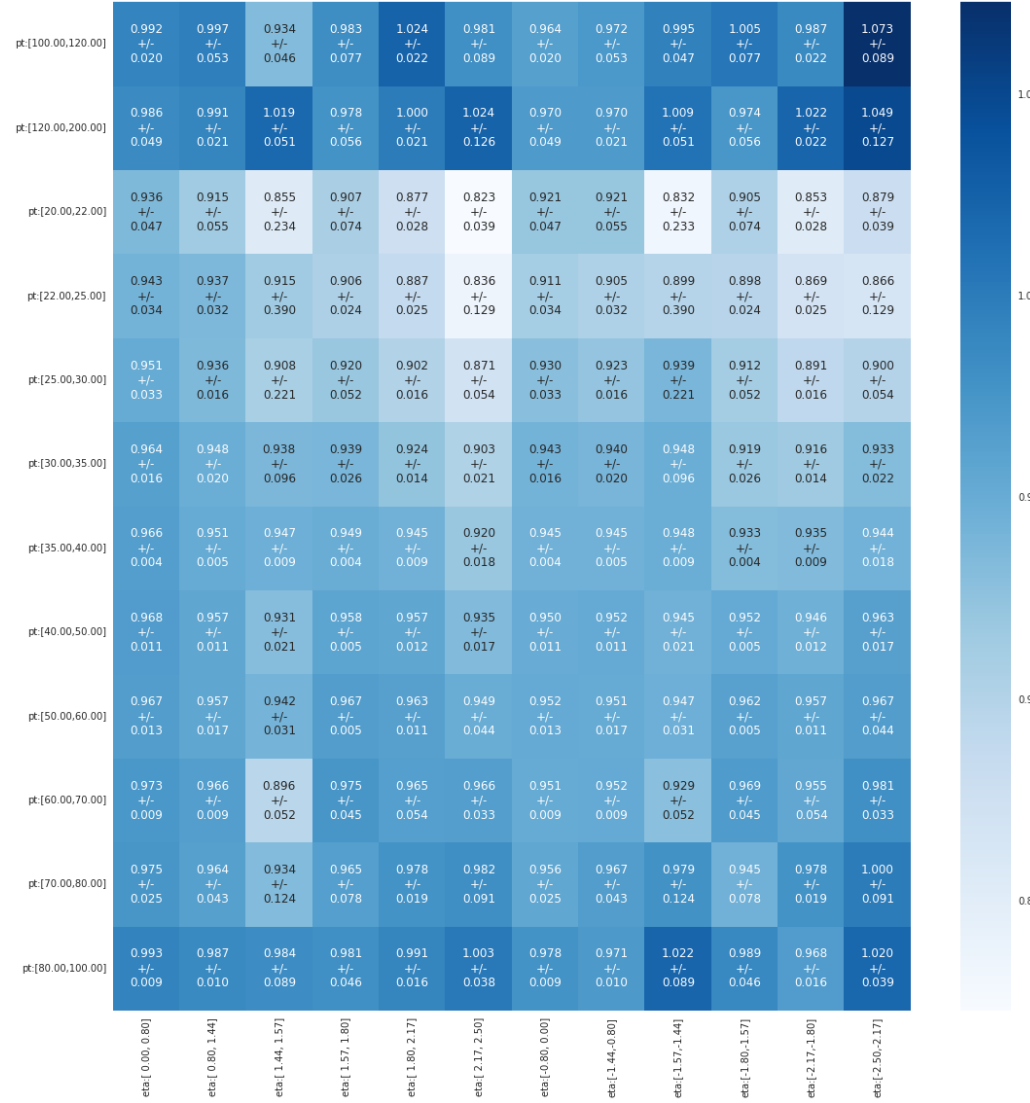
**Figure 5.4:** Scale factors in  $\eta$  bins of the leading and subleading muons for 2016 data set for dZ requirement, measured after muons have passed the HLT\_Mu17\_TrkIsoVVL\_Mu8\_TrkIsoVVL\_v\* OR HLT\_Mu17\_TrkIsoVVL\_TkMu8\_TrkIsoVVL\_v\* triggers.



**Figure 5.5:** Muon ID scale factors in  $p_T$  and  $\eta$  bins. Left: runs B to F. Right: runs G and H.



**Figure 5.6:** Muon ISO scale factors in  $p_T$  and  $\eta$  bins. Left: runs B to F. Right: runs G and H.

Figure 5.7: Electron ID+ISO scale factors in  $p_T$  and  $\eta$  bins.

## CHAPTER 6

---

### Simulated Samples

---

Before we look at the data, all the studies are done with the simulation. The most important requirements on the simulation is that it is accurate and has enough events in all the phase space corners. While this is almost true for the main backgrounds, for which the simulated samples are produced centrally for the use of the whole CMS, specific signal samples cannot be produced with big statistics for all analyses, since there are hundred analysis teams in CMC. Luckily for us, both  $bbZZ$  and  $bbWW$  samples have been produced with  $O(0.5\text{ M})$  events).

## 6.1 Signal simulation

MC signal samples of the resonant Higgs boson pair production have been generated at the Leading Order (LO) using the MADGRAPH 5 version 2.2.2.0 generator [29]. The gluon fusion production of a heavy narrow resonance is followed by the decay of the resonance into two SM Higgs bosons whose mass is fixed at 125 GeV.

Two signal MC samples are generated to cover the Higgs decay modes contributing to the 2 b jets 2 leptons 2 neutrinos final state of this measurement. The first sample type is a HH decay in to  $bbZZ$  channel, where one Higgs boson decays to a pair of b-quarks and the second Higgs boson decays into two Z bosons. In the second

sample type bbVV events are generated, where HH can decay through bbWW and bbZZ channels. For both samples, the Z boson-pair and the W boson-pair are set to decay leptonically to two leptons and two neutrinos, where a lepton could be an electron or a muon. The second, bbVV, sample is filtered using the generator level information such that only the events with a W-boson pair (bbWW) are kept, while the Z-pair events are dropped: there are very few of them in the bbVV sample, and most importantly, high statistics bbZZ is taken from the dedicated bbZZ sample of the first type.

Events in the signal bbZZ and bbWW MC samples are normalised to 2 pb HH production cross section, which is a typical value of the heavy resonance production at 300 GeV predicted by the WED. Additionally the normalization includes the branching ratios of the Higgs boson decays contributing to the final state studied here: 0.0012 and 0.0266 for  $HH \rightarrow bbZZ \rightarrow bb\ell\ell\nu\nu$  and  $HH \rightarrow bbWW \rightarrow bb\ell\nu\ell\nu$ , respectively [46].

Unless mentioned otherwise, throughout the text plots and numbers represent the graviton study. The data and backgrounds for the radion measurement are the same, thus distributions also show the same good Data MC agreement and can be found for at Figs. 8.4 for the graviton case and 8.5 for the radion case.

## 6.2 Background simulation

In this analysis the main backgrounds are  $t\bar{t}$  and Drell-Yan plus jets with the mass of the boson greater than 50 GeV. Not all the background processes pass our tight preselection (see section 8), those which do, are single top, dibosons, and ZH backgrounds that are listed in the Table 6.1:

The simulated samples of the background processes such as  $t\bar{t}$  [48] and the single

**Table 6.1:** Background Monte Carlo samples

---

DY1JetsToLL_M-50_TuneCUETP8M1_13TeV-madgraphMLM-pythia8
DY2JetsToLL_M-50_TuneCUETP8M1_13TeV-madgraphMLM-pythia8
DY3JetsToLL_M-50_TuneCUETP8M1_13TeV-madgraphMLM-pythia8
DY4JetsToLL_M-50_TuneCUETP8M1_13TeV-madgraphMLM-pythia8
WW_TuneCUETP8M1_13TeV-pythia8
WZ_TuneCUETP8M1_13TeV-pythia8
ZZ_TuneCUETP8M1_13TeV-pythia8
ZH_HToBB_ZToLL_M125_13TeV_aMC@NLO
TT_TuneCUETP8M1_13TeV-powheg-pythia8
ST_tW_top_5f_inclusiveDecays_13TeV-powheg-pythia8_TuneCUETP8M1
ST_tW_antitop_5f_inclusiveDecays_13TeV-powheg-pythia8_TuneCUETP8M1
ST_t-channel_top_4f_leptonDecays_13TeV-powheg-pythia8
ST_t-channel_antitop_4f_leptonDecays_13TeV-powheg-pythia8
ST_s-channel_4f_leptonDecays_13TeV-amcatnlo-pythia8

---

top tW and t-channel production processes [52] are generated at the next-to-leading order (NLO) with POWHEG [109], while single top s-channel production process is generated at NLO with MADGRAPH.  $t\bar{t}$  and single top production cross sections are rescaled to the next-to-next-to-leading order (NNLO). Drell-Yan (DY) process samples in association with 1, 2, 3 or 4 jets are generated at the leading order using MADGRAPH with the MLM matching [53] and rescaled to NNLO using FEWZ program [47, 104, 105].

As for the electroweak (EWK) order, DY samples have been rescaled to EWK NLO order with the NLO/LO k-factor of 1.23 [39]. Diboson samples are generated at LO with PYTHIA8.212 [107].

The main background process, which involves SM Higgs boson, is an associated production of the Higgs boson with a Z boson (ZH). ZH process is simulated using the generator *MadGraph5\_aMC@NLO* [49] with FxFx merging [108] and rescaled to NNLO with MCFM generator [55].

For LO and NLO samples NNPDF3.0 parton distribution functions (PDF) set

is used. POWHEG and MADGRAPH interfaced with PYTHIA8.212 [107] are used for the parton showering and hadronization steps. To describe the underlying event CUETP9M1 set derived in [106] is used. GEANT4 [35] is used to model the response of the CMS detector.

All the final cross sections denoted as NNLO are calculated at NNLO QCD accuracies and have been computed with the tool they were generated with. They found to be in agreement with the values from the LHC Higgs cross section working group [40, 42–45].

During the data taking in 2016 the average number of proton-proton interactions per bunch crossing was 24 (denoted as pile up later), and in MC samples this information has been introduced overlapping these interactions with the events of interest.

## CHAPTER 7

---

### Physics Objects Reconstruction

---

This the first ever bbZZ analysis performed at CERN with the real data. We use the standard set of the CMS reconstructed physics objects. Below, we describe reconstruction of each separately: electrons, muons, jets and b jets, and MET.

## 7.1 Electrons

The Gaussian Sum Filter (GSF) algorithm is used to reconstruct electrons [96]. GSF helps to estimate track parameters. The procedure starts as follows: a mixture of Gaussian distributions (normally about 4-6 components) [143] is used to estimate the energy loss in each layer of the tracker. The energy loss is modelled by the Bethe-Heitler formula. Two most important track properties are then computed: a weighted mean and the most frequent value (mode). The first estimate is unbiased while the latter one has a smaller width. In practice, mostly one works with the mode. Gaussian mixtures are determined minimising either the absolute difference between the cumulative density functions (CDFs) of the model and of the Gaussian mixture, or the Kullback-Leibner distance, which is a logarithm of the ratio of the probability density functions (pdfs) of the model with respect to the mixture. Finally, the tracks are extrapolated further to the ECAL. The measurement selects electrons,

which pass the following selection: leading electron  $p_T > 25 \text{ GeV}$  and subleading electron  $p_T > 15 \text{ GeV}$ ,  $|\eta| < 2.5$ , an isolation cut of 0.06, for which the cone of 0.3 is used to compute the  $\rho$ -subtracted PF isolation. Lepton isolation is calculated as a scalar sum of the transverse momentum ( $p_T$ ) of all the charged and neutral hadrons as well as photons around the lepton (excluding the cone) normalised to the  $p_T$  of the lepton itself.

On top of the selection defined above, a specific CMS Particle Object Group (POG) recommended working point (WP) is applied, which is a discriminant based on the a multivariate analysis (MVA) for classification of signal/background electrons. The WP consists of nearly 20 variables utilising the information from the impact point, tracks, and the ECAL:  $\chi^2$  variables of the track and the quality of its estimate,  $\delta\eta$ ,  $\delta\phi$ , energy of the 3 by 3 cluster, ECAL energy over momentum, etc. For this analysis we use the loose working point (another name can be WP90), as described in [110]. ID and ISO, as well as the HLT SFs are applied.

## 7.2 Muons

In this analysis we are using global muons reconstructed using the information from the tracker and muon system [92,93]. During the offline reconstruction, muons chambers segments are used as seeds for the "standalone muon" reconstruction. The seed is a position, a direction, and an initial momentum of the muon candidate. This serves as an input to the track fitting procedure utilising muon system information. The resulting object after executing this technique is what is called a standalone muon. Then, for each standalone muon the algorithm searches for the tracks reconstructed in the inner tracking system (tracker tracks) that would match the muon. Then for each standalone muon - tracker track pair the Kalman filter based fit [144] is performed.

The result is a collection of muons which are referred to as global muons. In this analysis the kinematic and isolation selection of global muons is the following: leading muon  $p_T > 20 \text{ GeV}$  and subleading muon  $p_T > 15 \text{ GeV}$ ,  $|\eta| < 2.4$ , a relative isolation cut of 0.15, with the cone of 0.4 used to compute  $\Delta\beta$ -subtracted PF isolation. Finally, a tighter selection - muon POG recommended WP Loose is applied [92, 102]. WP consists of track quality information:  $\chi^2$  of various fits, number of good hits in the tracker, number of layer missing the expected hit, impact parameter variables, matching variables (e.g., a segment in the muon station matched to the tracker track extrapolation), compatibility variables (e.g., a muon segment compatibility). ID, ISO, HLT and tracker SFs are applied.

### 7.3 Jets

Particle flow (PF) algorithm is used to reconstruct jets [94, 95], with the help of the anti- $k_T$  clustering algorithm having a distance parameter of  $R = 0.4$  [100, 121]. Jets are collimated bunches of stable hadrons originating from quarks and gluons after fragmentation and hadronization. Therefore, jet finding procedure is a back-propagation that starts with the detected objects and following the rules of the quantum mechanics for fragmentation and hadronization targets to identify the initial partons. Anti- $k_T$  is a sequential clustering algorithm that first defines the notion of the distance between the two particles in the collection of particles of the event, and also a distance between the particle and the beam axis. Then sequentially iterating over the particles collection it computes the smallest distances, if the smallest one is between the particles, their 4-momentum is combined into one. If the smallest distance is between the particle and the beam axis, then the particle is called the jet, removed from the collection, and the whole procedure continues. anti- $k_T$  is known

to be insensitive to the underlying event and to the pile up, therefore, is commonly used.

Reconstructed jets are further corrected for detector effects using specific corrections determined from the data and MC. Only jets passing  $|\eta| < 2.4$  and ( $p_T > 30 \text{ GeV}$ ) are considered for the analysis. All the necessary jet energy resolution (JER) and jet energy scale (JES) corrections provided by the JetMET group are applied [113].

## 7.4 Identification of b jets

MVA technique combining the information about the impact parameter, identified secondary vertices, as well as soft lepton (if any) contained inside of the jet is used by the CMVA algorithm to identify b quark originated jets. The output is a continuous MVA discriminant ranging in value from -1 to +1. Optimal cut is determined by the POG for several working points. We use CMVAv2 medium working point ( $> 0.4432$ ). We checked all three WPs and WP Medium gives the best limits. b tagging and mistagging corrections are applied.

## 7.5 Missing transverse energy

Even though neutrinos leave no trace in the CMS detector, their presence may be inferred through the momentum imbalance. A quantity reconstructed in this fashion in the plane perpendicular to the beam axis is called a missing transverse energy/momentun (MET). Precise reconstruction of leptons, photons, jets, etc is necessary for the correct computation of the MET. Detector miscalibration and PU also affect MET performance, thus the studies with the real data are always con-

ducted.

Due to the conservation of the momentum in the transverse plane, MET can be calculated as an absolute value of the negative vectorial sum of the transverse momentum of all observed particles:  $\vec{E}_T \equiv -\sum \vec{p}_T$

MET reconstructed using PF reconstructed particles [147] is what the majority of the CMS teams uses for analyses of 2016 data. Several correction recommended by the JetMET POG are applied [114]: jet corrections, corrections for the PU effect, etc. On top, a set of filters related to the instrumental effects is employed, such as removal of the misreconstruction caused by the fisier in the HCAL and/or noise in the tracker, etc. [115]. Schematic representation of the MET in the event with Z or photon is shown on the Fig. 7.1.

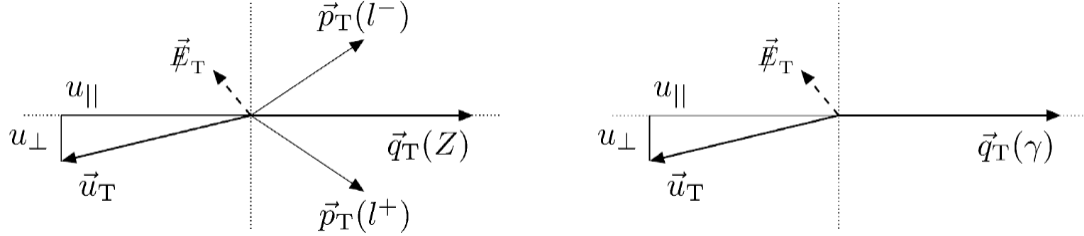


**Figure 7.1:** Z boson (left) and photon (right) kinematics with the vector of all the visible objects (denoted by  $u$ ) and a resulting MET.

## CHAPTER 8

---

### Event Selection

---

The resonances in search decay to two SM Higgs bosons. However, Higgs bosons further decay almost immediately. Therefore, it is critical to reconstruct Higgs bosons decay products with the high precision.

## 8.1 Higgs and Z Boson Selection

Only dilepton pairs having net charge of zero are considered as  $Z \rightarrow \ell\ell$  candidates. Pairs of prompt isolated leptons must have a dilepton mass greater than 76 GeV. This ensures the orthogonality with HIG-17-006 bbVV analysis (later also referred to as bbWW analysis) as well as helps selecting decays of real Z bosons.

Higgs boson candidates are reconstructed from the b jet pairs utilising the two b jets with the highest CMVA<sub>v2</sub> discriminant value. We do not veto additional b jets as with the increased PU growths the probability to have more b jets.

Double Higgs boson candidate is computed as a sum of Lorentz vectors of the  $Z \rightarrow \ell\ell$  candidate, MET, and a  $H \rightarrow b\bar{b}$  candidate. Then, we compute the transverse mass of that object.

This transverse mass definition that we follow is one of the commonly used and is logical in the sense that we subtract the longitudinal momentum component which

leaves us with the transverse momentum components only (while the energy remains the total energy). More precisely, as the z-component of the neutrinos' momentum is unknown and we decided not to reconstruct it, we form a pseudo transverse mass:  $\tilde{M}_T(HH) = \sqrt{E^2 - p_z^2}$  (further referred as transverse mass for brevity), where  $E$  and  $p_z$  are the energy and the z-axis component of the Lorentz energy-momentum vector of the HH candidate.

The resulting distribution,  $\tilde{M}_T(HH)$ , is what will be used in the binned shape analysis with the Higgs Combination Tool following the section "Binned shape analysis" as described at the twiki page [119]. Shape analysis is more sensitive than the simple cut-and-count experiment (one bin distributions) since more information/discrimination power is given to the likelihood function.

Initial data files, called ntuples, have enormous size of the order of more than a Terabyte per background process. To reduce the size of the ntuples and remove clear background events (on the other hand, to remove signal-like events we apply a sophisticated selection and use a BDT), we apply a "common-sense" HH preselection, which starts with the requirement on dilepton mass to be greater than 50 GeV and the event to contain at least two "good" jets - with  $p_T > 30$  GeV and  $|\eta| < 2.4$ . In addition to requirements on Higgs bosons decaying to b quarks mentioned above, we define Z bosons as two opposite sign muons with  $p_T > 20/15$  GeV (leading/subleading lepton) or two opposite sign electrons with  $p_T > 25/15$  GeV (leading/subleading lepton).

Later analysis cuts, the selection chain to improve signal-background separation, include:

- the requirement of at least two b jets in the event, out of which two with the highest CMVAv2 score are used to define  $H \rightarrow b\bar{b}$  candidate
- the lower end cut on the  $H \rightarrow b\bar{b}$  mass set to 20 GeV to remove the low mass

resonances, while giving BDT as many events in the CRDY as possible at the same time. The upper end cut is not explicitly set for the same purpose. The actual  $H \rightarrow b\bar{b}$  mass distribution after the analysis selection is concentrated in the range 30 to 220 GeV

- the Z boson selection takes the most energetic two leptons of the opposite sign and requires their dilepton mass to pass  $76 \text{ GeV} < Z \text{ mass} < 106 \text{ GeV}$  condition used for the signal region definition. This is a standard  $\pm 15 \text{ GeV}$  window for Z boson selection whose lower end also preserves orthogonality with the existing HIG-17-006 bbVV analysis
- HH candidate is approximated by the sum of  $\cancel{E}_T$ , Z, and  $H \rightarrow b\bar{b}$  decays. A loose cut on HH transverse  $> 100 \text{ GeV}$  removes evidently background events
- finally, an additional set of  $\cancel{E}_T$  cuts is used to ensure orthogonality with the existing HIG-18-013 bbZZ analysis focusing on the 2b jets + 2 leptons + 2 quarks, see Table 8.1. The MET cuts have been optimised by both analyses to yield the best limit when the results of two measurements are combined.

**Table 8.1:**  $\cancel{E}_T$  cut to orthogonalise the analysis with respect to HIG-18-013.

Signal mass, GeV	$\cancel{E}_T$ cut, GeV
260-300	$> 40$
350-600	$> 75$
650-1000	$> 100$

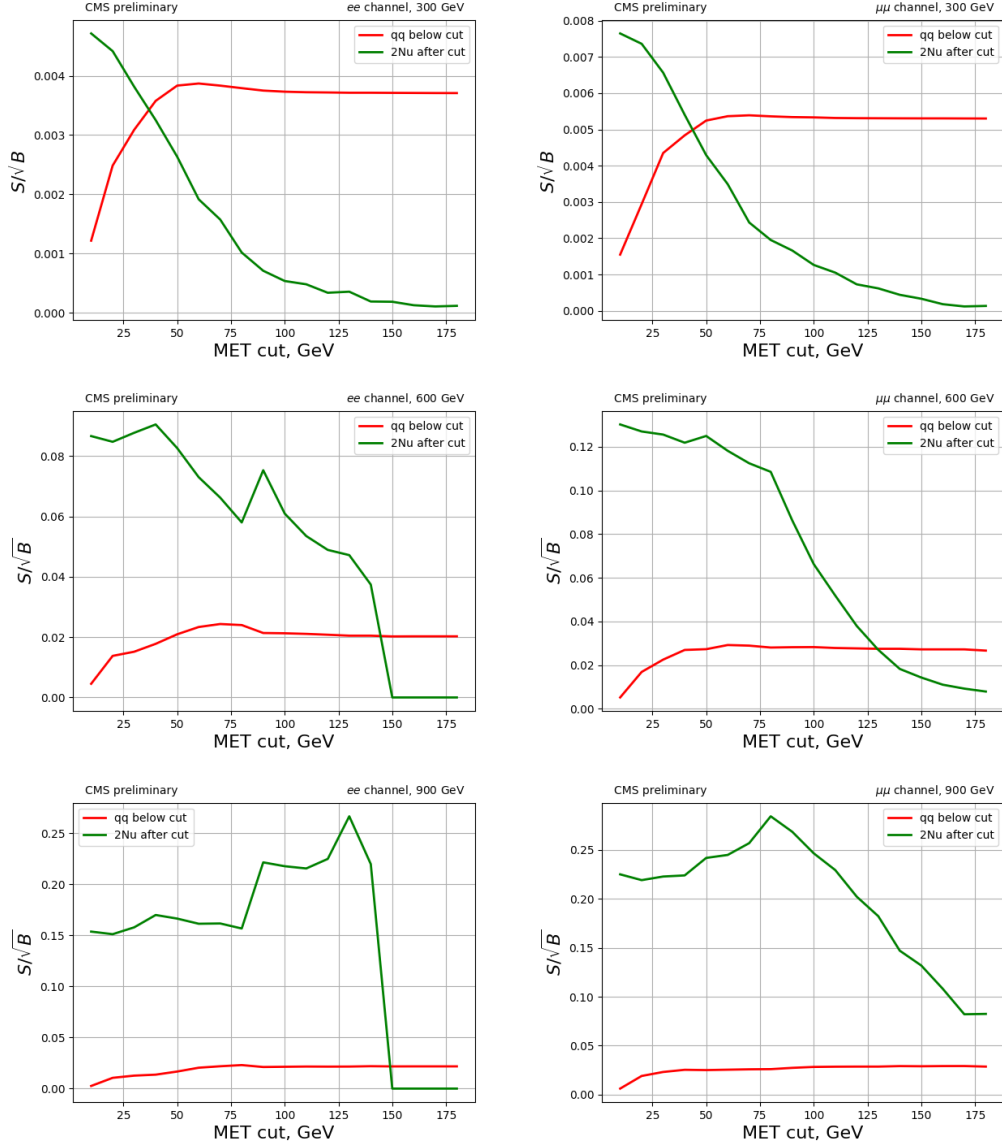


**Figure 8.1:** Significance-like ( $\sqrt{S}/B$ ) figure of merit as a function of the MET cut. Green curve shows the significance for our analysis keepings event above the cut, red curve is for HIG-18-013 analysis and their phase space is below the cut value. Top: 300 GeV cut. Middle: 600 GeV cut. Bottom: 900 GeV cut. On the left dielectron channel is shown, while dimuon plots are on the right.

## 8.2 $H \rightarrow b\bar{b}$ and $Z \rightarrow \ell\ell$ variables to define signal and control regions

In this analysis we define three regions in the  $H \rightarrow b\bar{b}$  and  $Z \rightarrow \ell\ell$  space. Two regions, CRDY and CRTT, are used to extract the normalizations of DY and  $t\bar{t}$  backgrounds correspondingly. Signal region (Fig. 8.2) is chosen by the set of  $H \rightarrow b\bar{b}$  and  $Z \rightarrow \ell\ell$  cuts 8.2. To further reduce background contamination in this region, an additional cut on the MVA output is used. Boosted decision trees (BDT) MVA technique is employed to separate background from signal. Below we describe in details selection of each region and BDT construction.

For CRDY we invert  $H \rightarrow b\bar{b}$  cut, keeping in the lower sideband only events with the mass of Higgs boson higher than 20 GeV to avoid fakes from QCD. For CRTT we invert  $Z \rightarrow \ell\ell$  cut, keeping only high mass sideband to ensure the orthogonality with the existing HIG-17-006 bbVV analysis, since the lower sideband is already included in the phase space used by them.

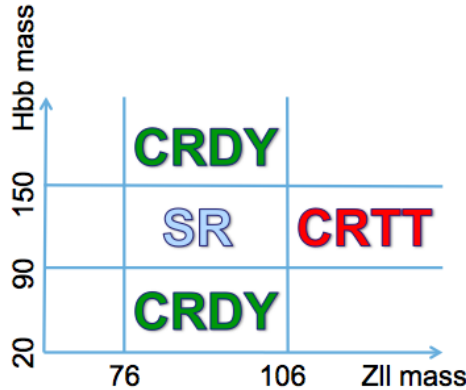


**Figure 8.2:** Signal region, control region  $t\bar{t}$ , and control region Drell-Yan in the phase space of  $Z \rightarrow \ell\ell$  and  $H \rightarrow b\bar{b}$  masses.

**Table 8.2:** Efficiency of the BDT selection requirement.  $ee$  channel (top) and  $\mu\mu$  channel (bottom).

sample	Efficiency at 300 GeV, [%]	Efficiency at 900 GeV, [%]
signal (bbZZ)	89.2	94.9
signal (bbWW)	75.0	88.4
$t\bar{t}$	28.8	0.2
Drell-Yan	74.2	1.2
Single top	33.1	1.1
ZH	88.8	10.7
Dibosons	90.0	5.0

sample	Efficiency at 300 GeV, [%]	Efficiency at 900 GeV, [%]
signal (bbZZ)	58.1	91.1
signal (bbWW)	25.9	96.3
$t\bar{t}$	13.6	0.2
Drell-Yan	39.0	0.8
Single top	13.0	0.2
ZH	56.0	8.4
Dibosons	51.4	6.2

### 8.3 Signal and background characteristics

The signal region is further purified removing backgrounds by applying the cut on the BDT output (Table 8.2 contains the efficiency numbers for the BDT cut). The first set of BDT variables in the early version of the analysis included 30-50 variables, which could potentially discriminate signal from the background. The set contained variables related to the kinematic properties of the signature, as well as a dozen of angular variables. After the first optimization of the BDT training and produced ranking of variables, nine best variables were determined and chosen to be used for the final analysis. Removal or addition of other variables did not improve the performance significantly. To simplify the analysis, the same set of nine variables is used in both low and high mass trainings and for both spin hypotheses.

With 16 masses points in the range from 250 to 1000 GeV, one can: train 16

discriminants, train one complex hyperparametrised neural network, split the mass range into regions with the similar kinematics and thus train only few BDTs. The latter is the approach that has been adopted by mature (legacy) HH analyses, and we are following the same procedure. We split the mass range into two: low mass and high mass (à la HIG-17-002 and HIG-17-008). These simplification costs some performance loss but allows analysis to proceed with just two BDTs instead of training one BDT per mass point, which would require more than a dozen of trainings per heavy resonance. In case of the infinite statistics, training a dedicated BDT for each signal mass hypothesis would give a better performance, but in our case we are statistics dominated, thus training only two BDTs also has benefits in terms of the size of the signal sample, absence of the overtraining etc. In addition, the adopted path saves computational resources. Lastly, physics-wise, bbZZ signature is not the most sensitive, bb $\gamma\gamma$  is due to an excellent CMS diphoton mass resolution. Thus, the difference in sensitivity is a factor of 30-100 depending on the mass. Therefore, training a dozen of BDTs is clearly impractical. For more discussion on the topic please refer to the chapter 9.

The low/high mass boundary value for HH analyses is chosen typically in the range 300-450 GeV. In our case the performance of the boundary around 300 GeV (area under the ROC curve for low mass BDT is 0.9138 and 0.9805 for high mass BDT) is similar to the boundary option at the 450 GeV (area under the ROC curve for low mass BDT is 0.9086 and 0.9957 for high mass BDT), and to the one in the middle of the range (area under the ROC curve for 400 GeV for low mass BDT is 0.9074 and 0.9928 for high mass BDT). Therefore, we chose the value of 450 GeV, which is also a choice of the bbbb analysis [120]. Upon running the full analysis chain up to the expected limits, the choice of 450 GeV was verified to be the best split point option: the usage of the high mass BDT at the 400 GeV or low mass BDT at the 500

**Table 8.3:** Number of events surviving analysis cuts corresponding to the last entry in the 8.3 .

Process, mass point	ee channel, %	mm channel, %
bbZZ, 300 GeV	2256	4511
bbWW, 300 GeV	53	85
bbZZ, 900 GeV	8034	12963
bbWW, 900 GeV	12	23

GeV was yielding suboptimal results thus confirming the mass boundary choice.

Splitting the mass range into two regions, we arrive at the low mass BDT, which merges (with the weight '1') seven signal samples: 250, 260, 270, 300, 350 400, 450 GeV, and the high mass BDT, which combines nine signal samples of masses: 500, 550, 600, 650, 700, 750, 800, 900, 1000. In each case the composition of the background is the same, it is a mix (by cross section) of  $t\bar{t}$  and Drell-Yan plus jets.

Cut flow for  $ee$  and  $\mu\mu$  channels from the generator level up to before the BDT selection is shown on the figures 8.3. In the cut flow table 8.3 the following definitions are used: very loose selection means all GsfElectrons and Muons from the basic collections that match generator level electrons/muons and pass the very minimal kinematic cuts; loose selection means loose POG selection consisting of kinematic cuts, impact parameters  $dxy$  and  $dz$ , and iso cuts. Shown final efficiency values are given in terms of the number of events 8.3:

## 8.4 Data and MC comparison

BDT selection is applied in the signal region only, we are not cutting on BDT for control regions, therefore, all the mass points belonging to the low mass region (and separately to the high mass region) have the same background and data distributions. Thus, we provide plots for two mass points: one mass point representing low mass

	<b>2 very loose muons</b>	<b>2 loose muons</b>	<b>mva ID</b>	<b>leading pt and eta gap</b>	<b>iso&lt;0.15</b>	<b>trigger</b>	<b>&gt;=2b-jets, Hbb and Zll cuts</b>
<b>bbWW300</b>	100.0	41.8	21.6		20.3	17.8	16.6
<b>bbZZ300</b>	100.0	87.4	61.6		56.7	43.0	40.7
<b>bbWW900</b>	100.0	53.5	15.8		14.6	10.5	9.9
<b>bbZZ900</b>	100.0	84.0	63.3		59.7	53.6	50.2
	<b>2 very loose electrons</b>	<b>2 loose electrons</b>	<b>mva ID</b>	<b>leading pt and eta gap</b>	<b>iso&lt;0.06</b>	<b>trigger</b>	<b>&gt;=2b-jets, Hbb and Zll cuts</b>
<b>bbWW300</b>	100.0	38.8	18.9		17.4	13.0	10.0
<b>bbZZ300</b>	100.0	68.2	46.3		43.9	24.7	23.1
<b>bbWW900</b>	100.0	38.5	14.9		13.1	5.5	4.8
<b>bbZZ900</b>	100.0	71.4	46.0		43.7	36.0	33.9

**Figure 8.3:** Cut flow for mm (top) and ee (bottom) channels.

region, 300 GeV, and one mass point representing high mass region, 900 GeV. Signal bbZZ and bbWW rates for all plots are multiplied additionally by a factor of 500 purely for the visualization purpose and do not go in the real analysis.

Postfit plots that include SR in the simultaneous fit with control regions, hence a common jargon name "Full postfit" plots, in contrast to the control regions only type of the fit, or a control regions plus signal region sideband. Figures 8.4 - 8.5 show data and MC comparison in the SR, CRDY, and CRTT. For both  $ee$  and  $\mu\mu$  channels, low and high mass regions. The latest style plots produced for the analysis public document (Physics Analysis Summary called "PAS") can be found at Fig. 8.4 for the graviton case and Fig. 8.5 for the radion case.

Distributions of nine variables that go into the BDT have been studied in depth during the pre-approval process and are available in the Appendix of the analysis note [111]. All variables show good data/MC agreement after applying postfit scale factors (not to be confused with the POG recommended scale factors in the section below). The most important variables in this analysis, namely the BDT itself and the variable that we fit,  $\tilde{M}_T(HH)$ , are shown in the Fig. 8.4 for graviton and in Fig. 8.5 for the radion.

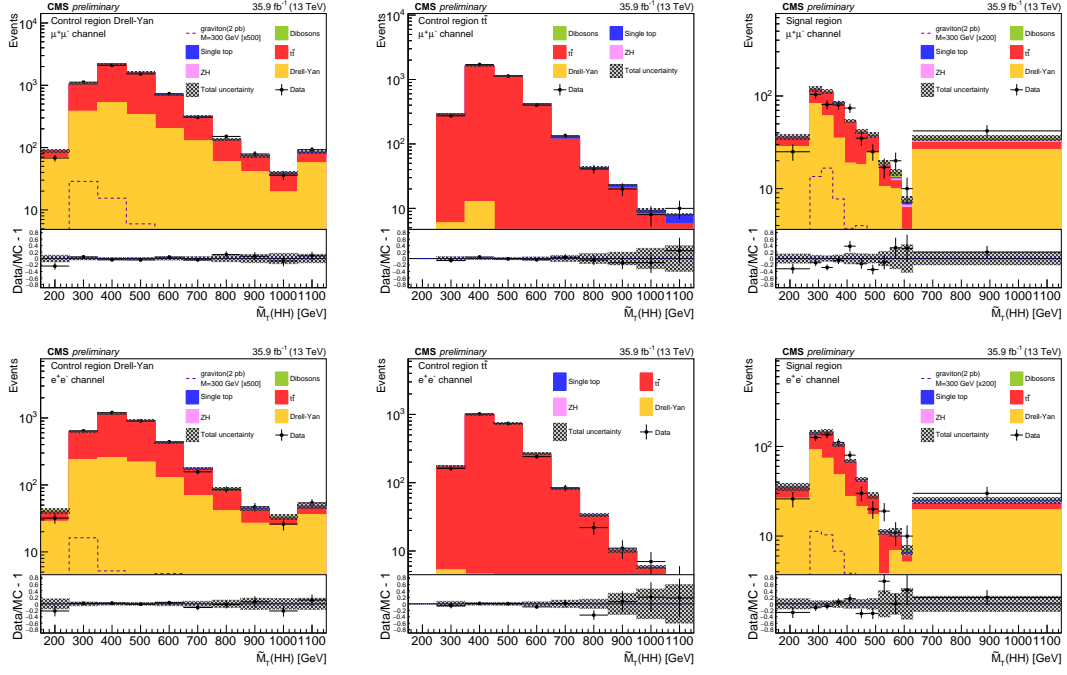


**Figure 8.4:** Transverse mass of the reconstructed HH candidates for data, the simulated signal graviton sample for the 300 GeV mass hypothesis, and simulated backgrounds scaled according to the fit results. The top row shows the figures for the muon channel while the bottom row is for the electron channel. For each row, the left plot is for the Drell-Yan control region, the middle is for the  $t\bar{t}$  control region, and the right is for the signal region. Signal normalization choice is discussed in the text. The crosshatched area represents the sum of statistical and systematic uncertainties.

## 8.5 Scale Factors

Electron ID and ISO scale factors, as well as HLT scale factors (Fig. 5.1), have been computed by VHbb group, which ntuples and analysis setup we reutilise. Scale factors have been presented at the EGamma physics object groups (POG) meeting [112] and fully approved. We reuse those scale factors and apply them to our MC samples.

Muon ID scale factors, as well as ISO scale factors, have been derived separately for runs G/H and B/C/D/E/F runs (2016 data at LHC has been split into several "runs") and then luminosity averaged to obtain the final numbers [57]. Tracker scale factors (5.1) are taken from the Muon POG twiki page [58] and used as is. HLT dimuon scale

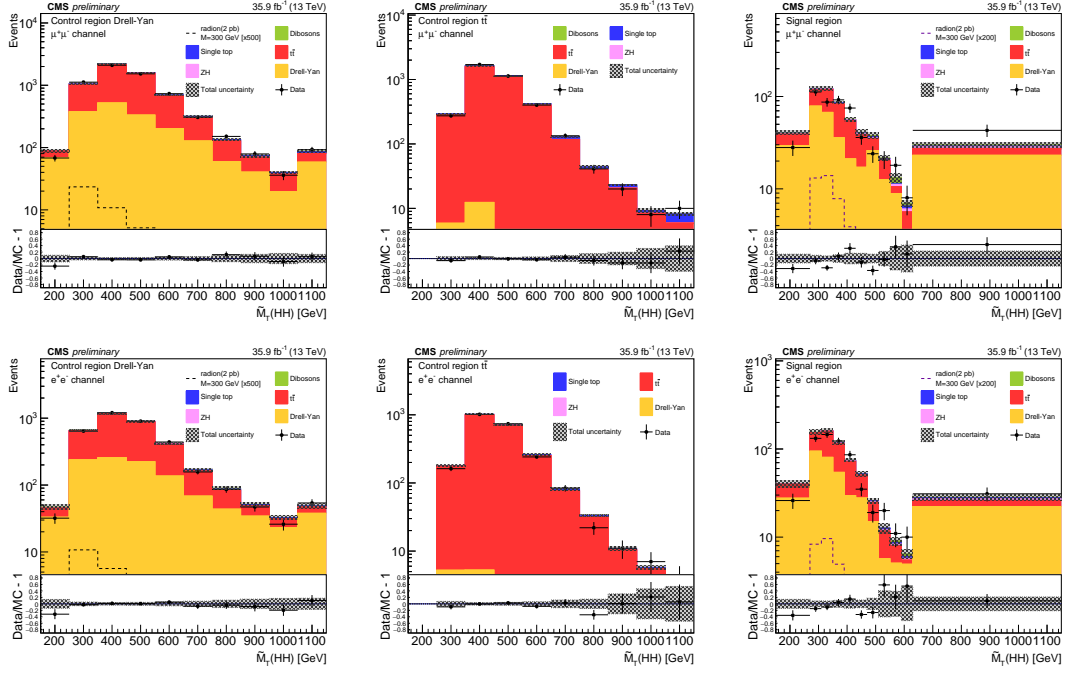


**Figure 8.5:** Transverse mass of the reconstructed HH candidates for data, the simulated signal radion sample for the 300 GeV mass hypothesis, and simulated backgrounds scaled according to the fit results. The top row shows the figures for the muon channel while the bottom row is for the electron channel. For each row, the left plot is for the Drell-Yan control region, the middle is for the  $t\bar{t}$  control region, and the right is for the signal region. Signal normalization choice is discussed in the text. The crosshatched area represents the sum of statistical and systematic uncertainties.

factors were derived by VHbb group and further approved by the muon POG. These scale factors were derived separately for run H (Fig. 5.3) and B/C/D/E/F/G (Fig. 5.2) runs and then luminosity averaged [59]. On top, separate scale factors are calculated for the dZ requirement of `HLT_Mu17_TrkIsoVVL_Mu8_TrkIsoVV_L_DZ_v*` OR `HLT_Mu17_TrkIsoVVL_TkMu8_TrkIsoVVL_DZ_v*` triggers, using dilepton events that have already passed the `HLT_Mu17_TrkIsoVVL_Mu8_TrkIsoVVL_v*` OR `HLT_Mu17_TrkIsoVVL_TkMu8_TrkIsoVVL_v*` triggers (Fig. 5.4).

## CHAPTER 9

---

### **BDT Discriminant**

---

The Toolkit for Multivariate Data Analysis with ROOT (TMVA) package is used to perform BDT training [117]. This ROOT-integrated library enables the usage of the machine learning techniques for the physics data analysis and is commonly used.

## **9.1 Construction of the BDT**

In this analysis we use the set of nine variables to construct the BDT. These variables are the same in both low and high mass trainings and for both heavy resonances.

Some variables are important only in the specific mass regime, some are ranked highly universally across the whole mass range. For example, in the low mass regime  $E_T^{\text{miss}}$  and  $H \rightarrow b\bar{b}$  mass are powerful discriminators against Drell-Yan to leptons plus jets. That is why these observables are located in the top three variables of the ranking for low mass BDT (Figs. 9.1). In the high mass regime the leverage is in the boost, therefore,  $\Delta R = \sqrt{\Delta\phi^2 + \Delta\eta^2}$  variables, as well as  $p_T$ -related variables show high performance (Figs. 9.1). Namely,  $p_T$  of both Higgs bosons, Z boson, and also separation  $\Delta R$  between two b-jets and also  $\Delta R$  between two leptons. It is worth noting that  $H \rightarrow b\bar{b}$  mass is a powerful discriminator ranked highly for all mass regimes and both channels. Plots of input variables and correlations are shown on

Rank	Importance, %	Rank	Importance, %
<b>1</b>	dR_bjets	<b>1</b>	dR_leps
<b>2</b>	met	<b>2</b>	Hbb mass
<b>3</b>	Hbb mass	<b>3</b>	dR_bjets
<b>4</b>	pT(ZZ)	<b>4</b>	Hbb pT
<b>5</b>	dR_leps	<b>5</b>	Z pT
<b>6</b>	Hbb pT	<b>6</b>	pT(ZZ)
<b>7</b>	Z pT	<b>7</b>	met
<b>8</b>	M(ZZ)	<b>8</b>	M(ZZ)
<b>9</b>	Z mass	<b>9</b>	Z mass

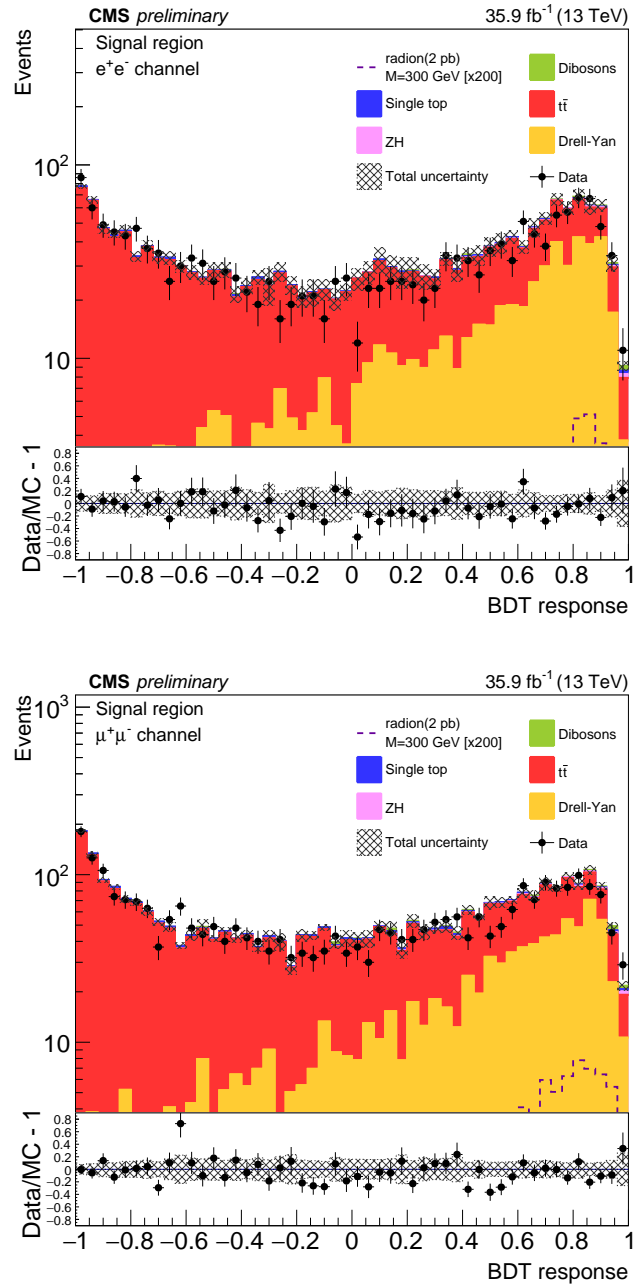
  

Rank	Importance	Rank	Importance
<b>1</b>	dR_bjets	<b>1</b>	Hbb mass
<b>2</b>	met	<b>2</b>	dR_bjets
<b>3</b>	Hbb mass	<b>3</b>	dR_leps
<b>4</b>	Hbb pT	<b>4</b>	Hbb pT
<b>5</b>	Z pT	<b>5</b>	pT(ZZ)
<b>6</b>	pT(ZZ)	<b>6</b>	Z pT
<b>7</b>	dR_leps	<b>7</b>	met
<b>8</b>	M(ZZ)	<b>8</b>	M(ZZ)
<b>9</b>	Z mass	<b>9</b>	Z mass

**Figure 9.1:** Ranking of variables in the BDT training for electron(muon) channel at the top(bottom). Left: low mass BDT. Right: high mass BDT.

the Figs. 9.3, 9.9, 9.7, 9.8, 9.13, 9.14.

It is hard to get high performance in the low mass training, since this is where all the backgrounds are concentrated (Figs. 9.3, 9.9). The rate of background in this region is enormous and most variables have similar distributions for signal



**Figure 9.2:** BDT plots for radion case, electron(muon) channel at the top(bottom). Signal region, 300 GeV mass hypothesis. For electrons cut is at 0.4, for muons at 0.7. More details at the table 12.1.

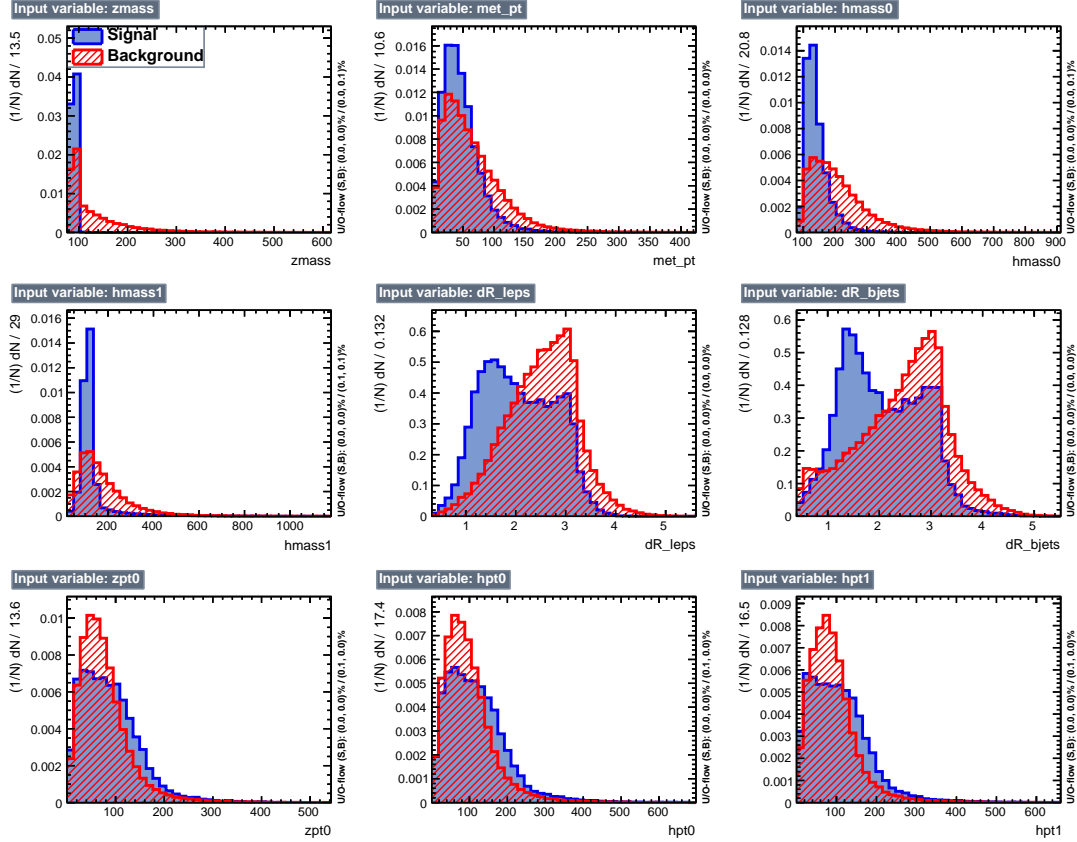


**Figure 9.3:** Variables used in the low mass training for electron channel. Index '1' refers to  $b\bar{b}$  and index '0' refers to ZZ.

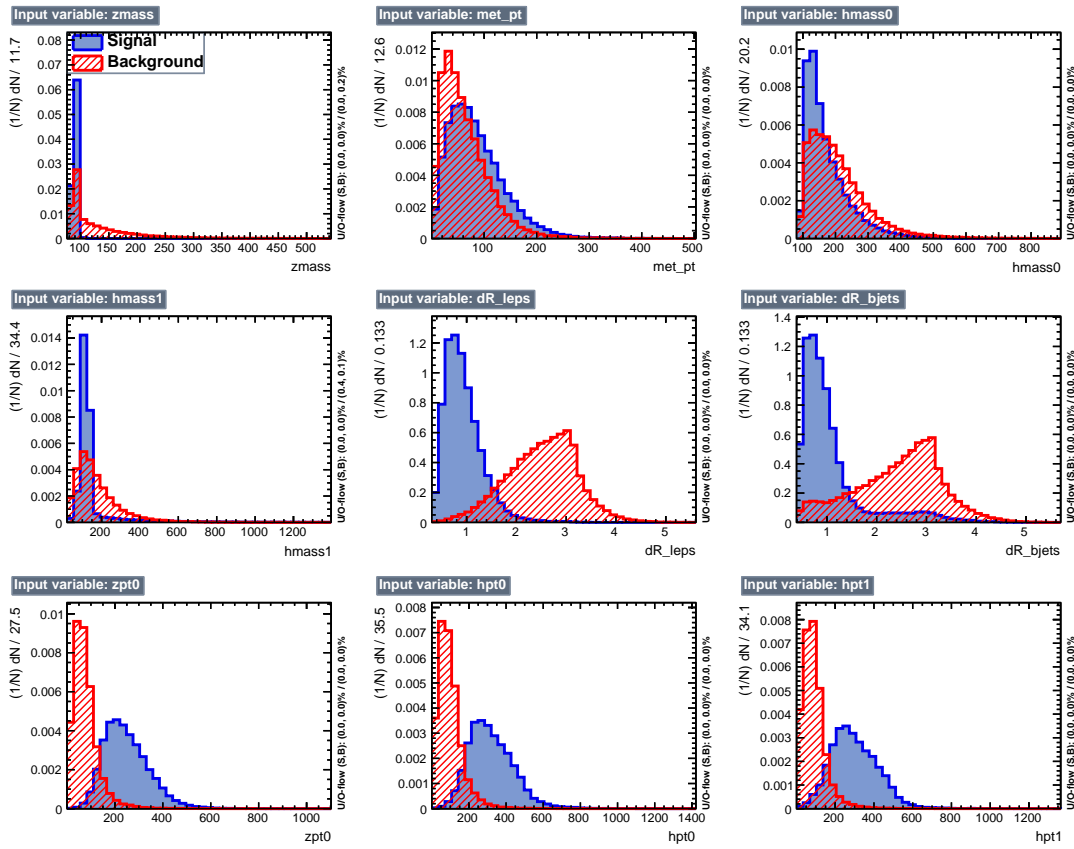


**Figure 9.4:** Variables used in the high mass training for electron channel.

and backgrounds. However, BDT performance is noticeably better than what can be achieved using a simple linear discriminant method (Figs. 9.5, 9.6, 9.11, 9.12).

Earlier versions of the analysis tried more granular approach to the number of BDTs, up to four BDTs to cover the whole range from 250 to 1000 GeV. But it was shown that this added extra complexity brings almost no improvement, while in fact is error prone and computationally twice more expensive. This is why other HH analyses also split the whole mass range only in two subranges and we followed the same suggestion. The BTD plots for radion case in the signal regions for 300 GeV mass hypothesis are shown at Fig. 9.2.

Performance of the high mass training is perfect (Figs. 9.4, 9.10, ). The ROC curves are close to the top right corner of the efficiencies space, which means a high signal efficiency is achieved along side with the low efficiency of the background. This is due to the fact that most backgrounds peak in the low mass region. Even linear discriminant is performing well in this situation (Figs. 9.5, 9.6, 9.11, 9.12).

For completeness purpose and research reproducibility, it is worth mentioning in this paragraph the technical details. The following TMVA specific parameters have been used for the BDT training (most parameters are default ones since no significant improvement was observed when varying the parameters one at a time): NTrees = 800, BoostType=Grad, Shrinkage=0.1, UseBaggedBoost=True, GradBaggingFraction=0.5, SeparationType= GiniIndex, nCuts=30, and MaxDepth=3.

Electrons and muons have been optimised separately but BDT trainings show similar performance (Fig. 9.6 and 9.12). BDT distributions for data and MC comparison are created with the nominal values for the lepton and b jet scale factors. When shape systematics is considered to produce final limits, BDT shapes are varied using 'Up' or 'Down' versions of the scale factors and all the input variables to the BDT are modified in the similar fashion as well. The BDT plots shown below are

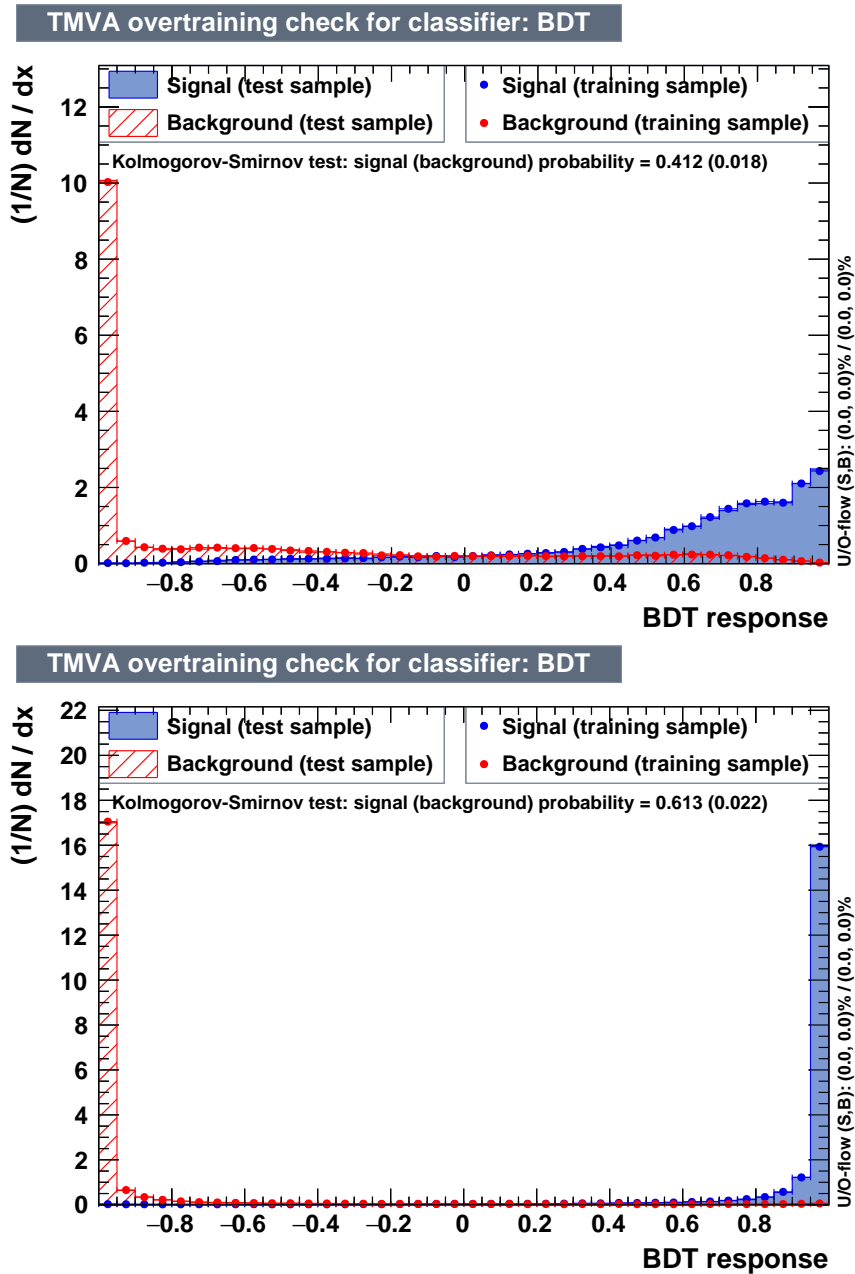


**Figure 9.5:** BDT discriminants for electron channel. Top: low mass training. Bottom: high mass training.

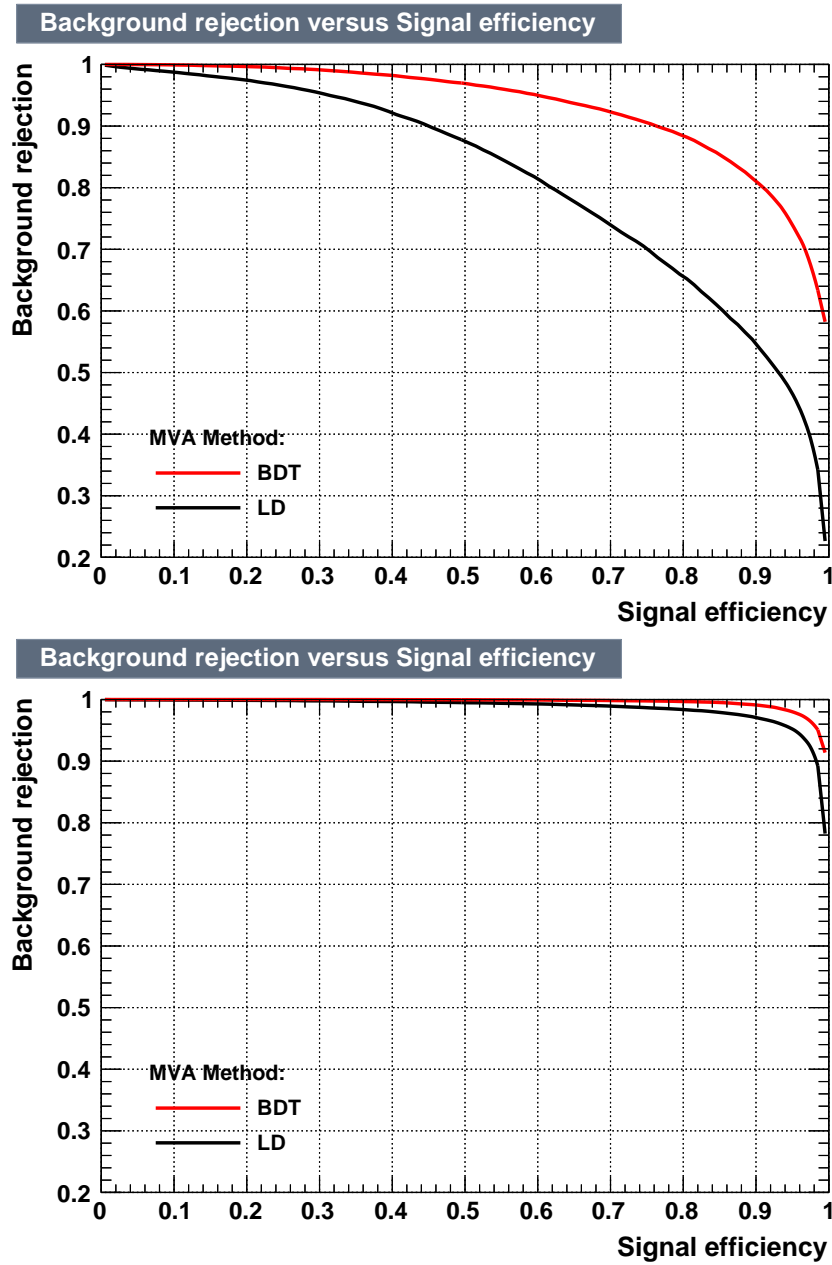
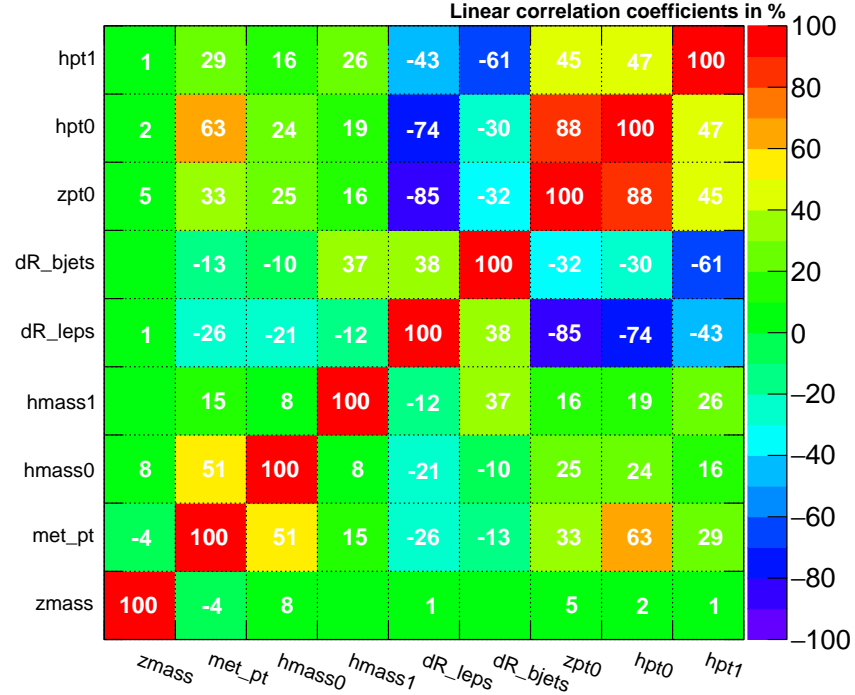


**Figure 9.6:** ROC curves for electron channel. Top: low mass training. Bottom: high mass training.

**Correlation Matrix (signal)**



**Correlation Matrix (background)**

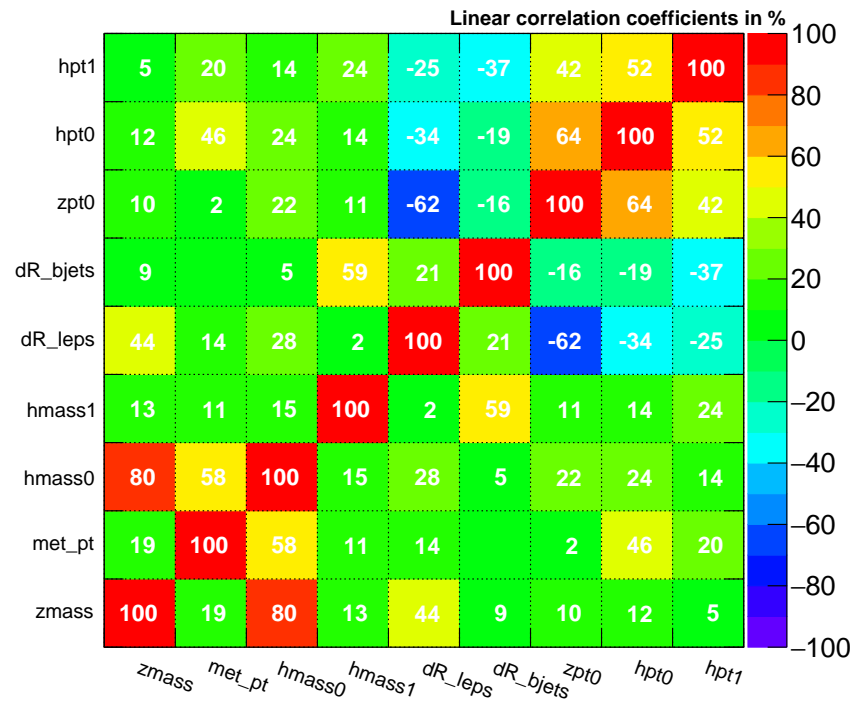
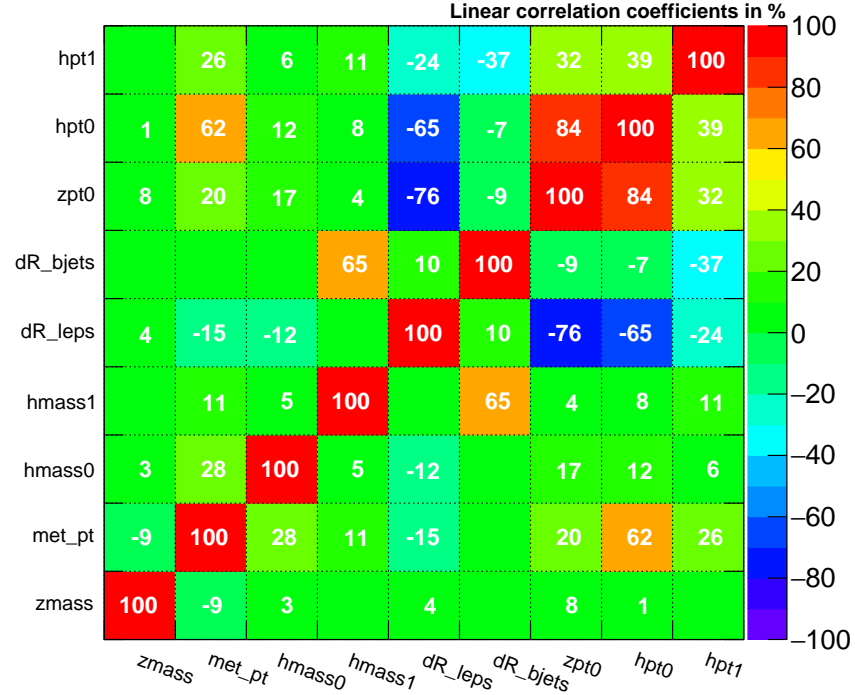


**Figure 9.7:** Input variables correlations for electron channel, low mass training. Top: signal sample mix. Bottom: background sample mix.

**Correlation Matrix (signal)**



**Correlation Matrix (background)**

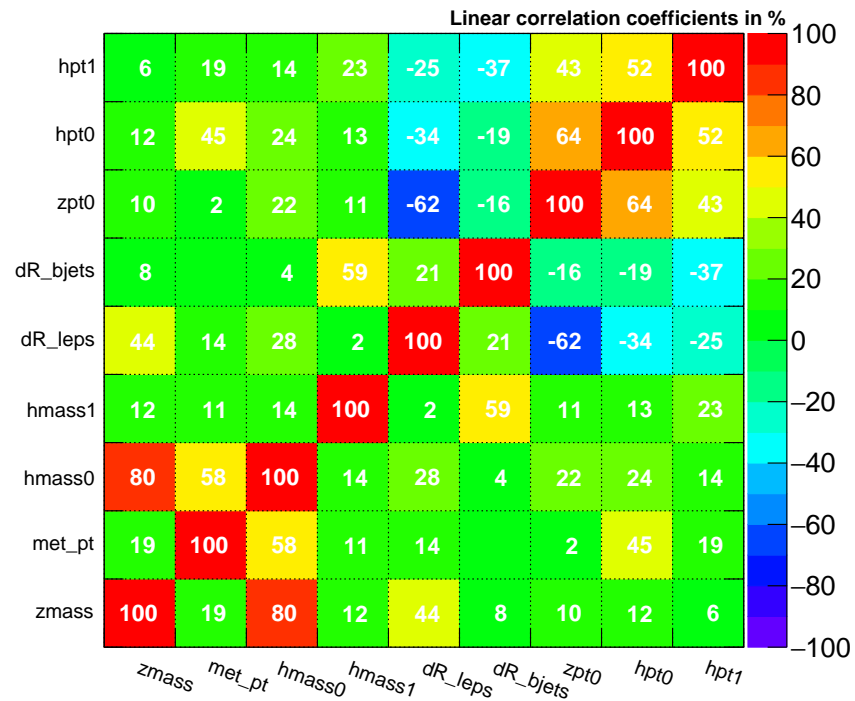


**Figure 9.8:** Input variables correlations for electron channel, high mass training. Top: signal sample mix. Bottom: background sample mix.

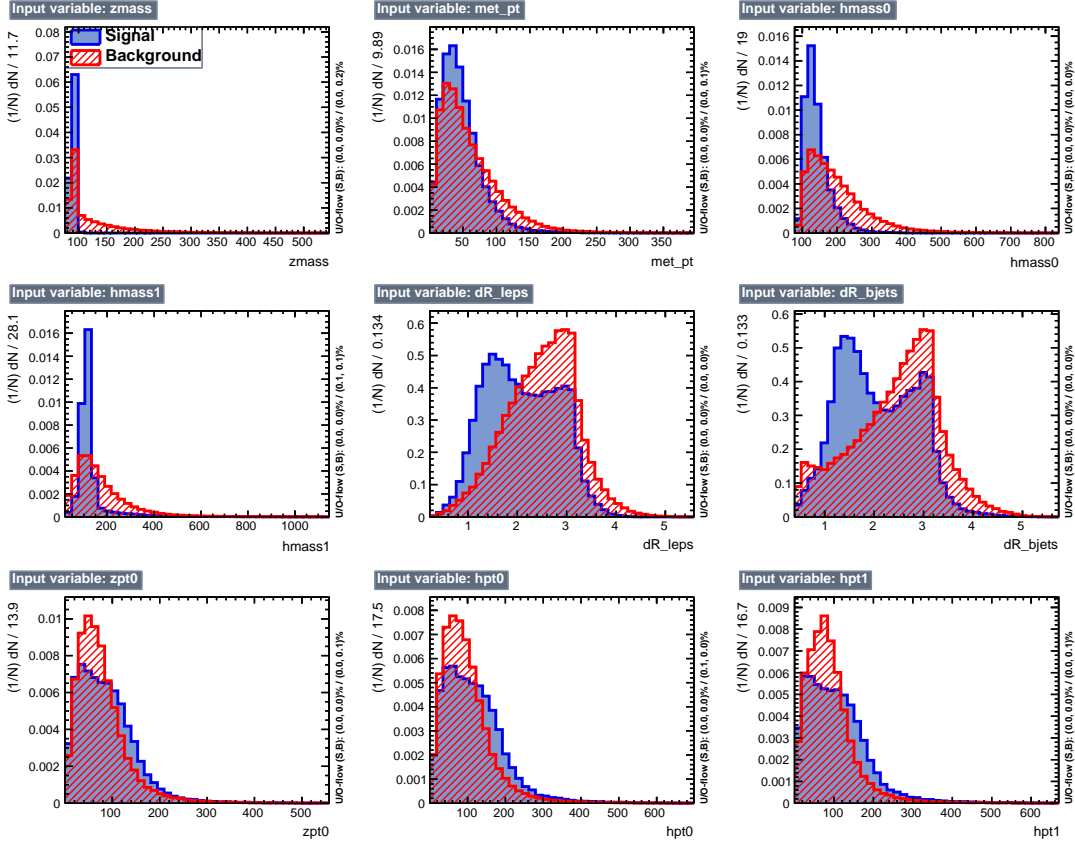


**Figure 9.9:** Variables used in the low mass training for muon channel. Index '1' refers to  $b\bar{b}$  and index '0' refers to ZZ.

further modified applying postfit values of DY and  $t\bar{t}$  normalizations returned from the Maximum Likelihood fit performed with the real data.

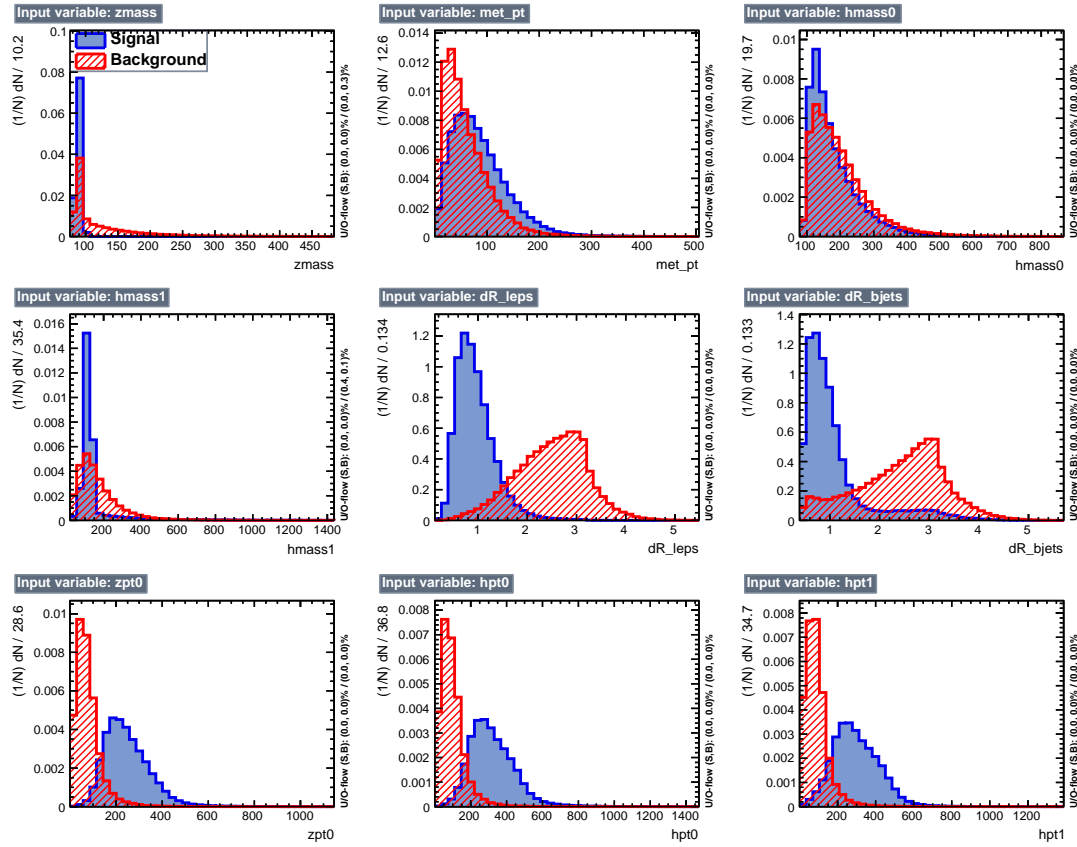


**Figure 9.10:** Variables used in the high mass training for muon channel.

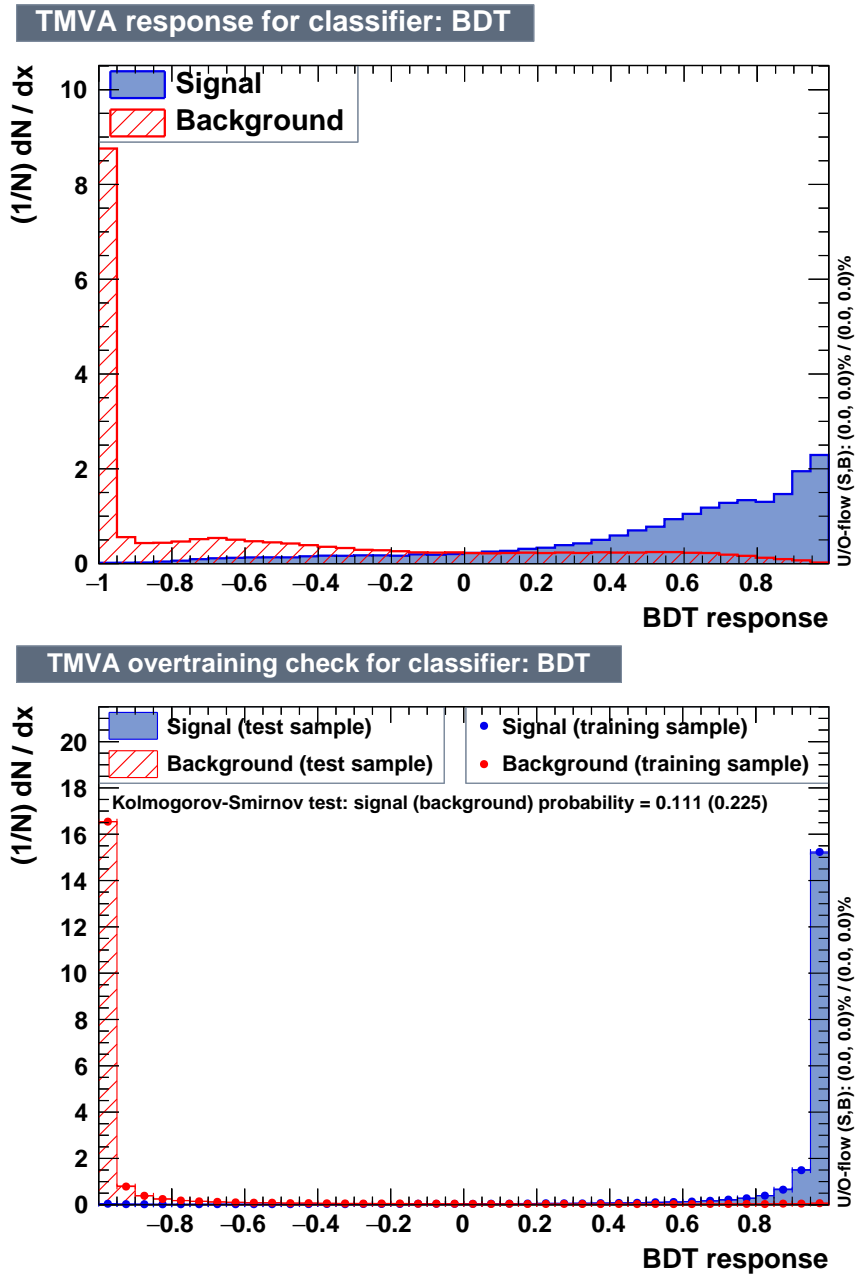


**Figure 9.11:** BDT discriminants for muon channel. Top: low mass training. Bottom: high mass training.

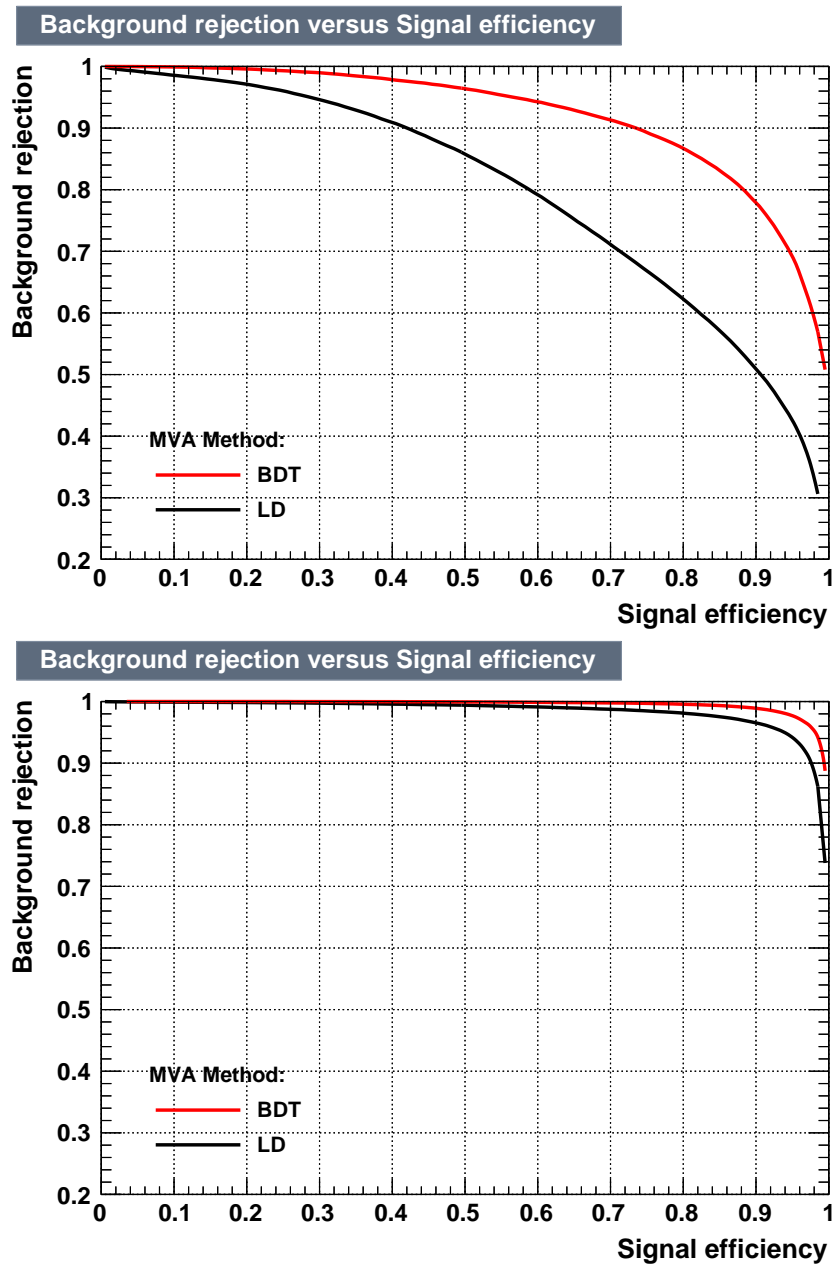
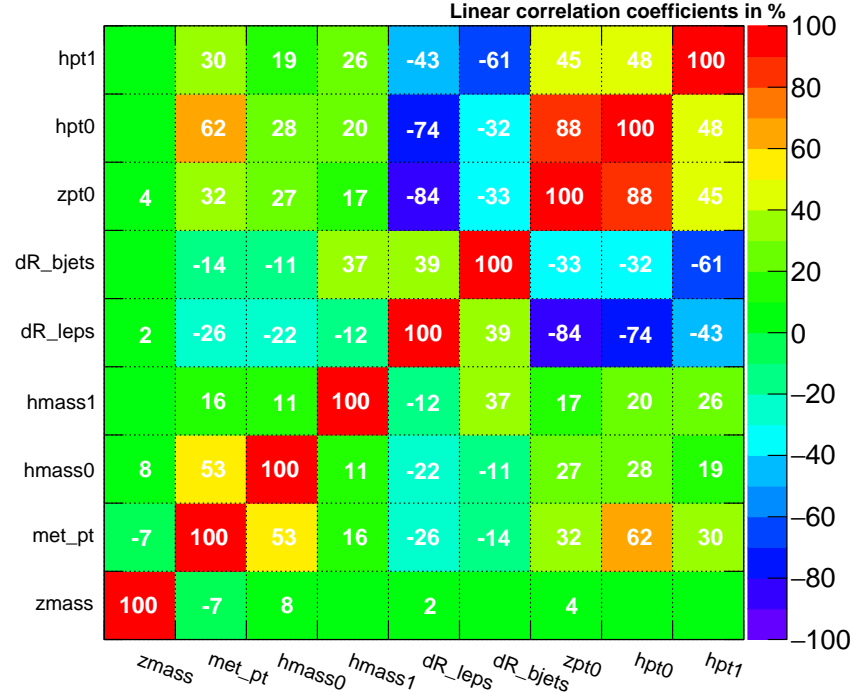


**Figure 9.12:** ROC curves for muon channel. Top: low mass training. Bottom: high mass training.

### Correlation Matrix (signal)



### Correlation Matrix (background)

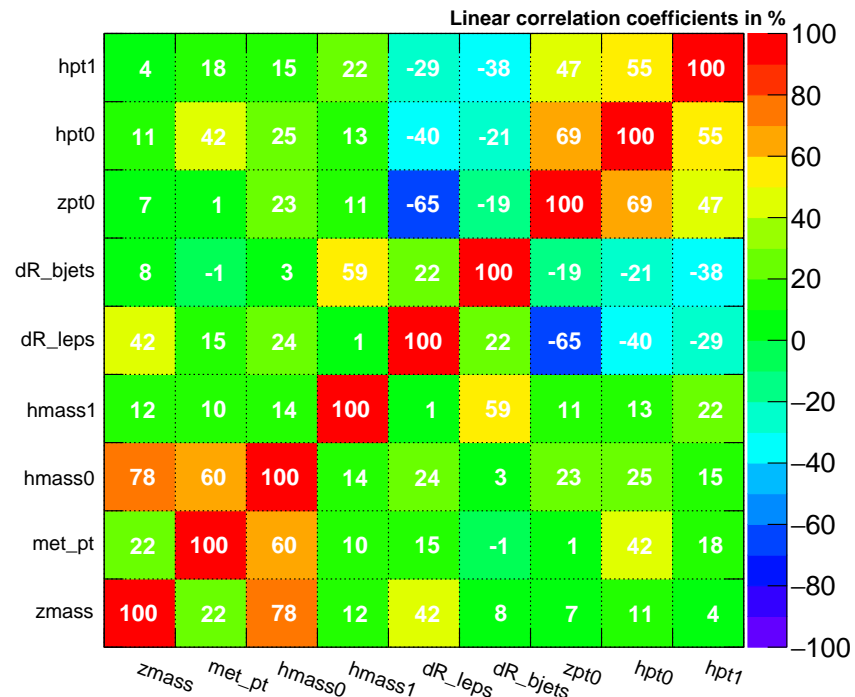
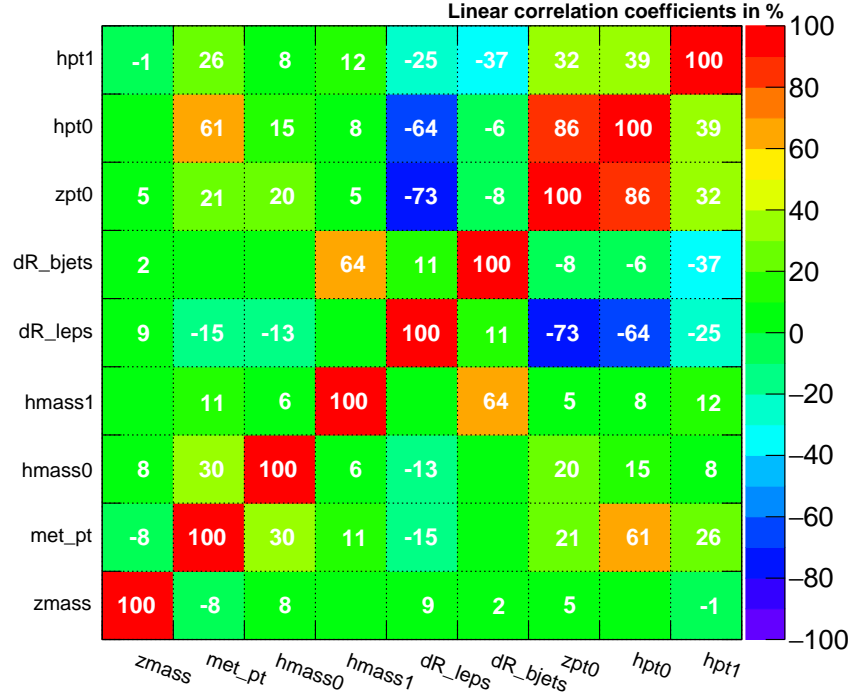


**Figure 9.13:** Input variables correlations for muon channel, low mass training. Top: signal sample mix. Bottom: background sample mix.

**Correlation Matrix (signal)**



**Correlation Matrix (background)**

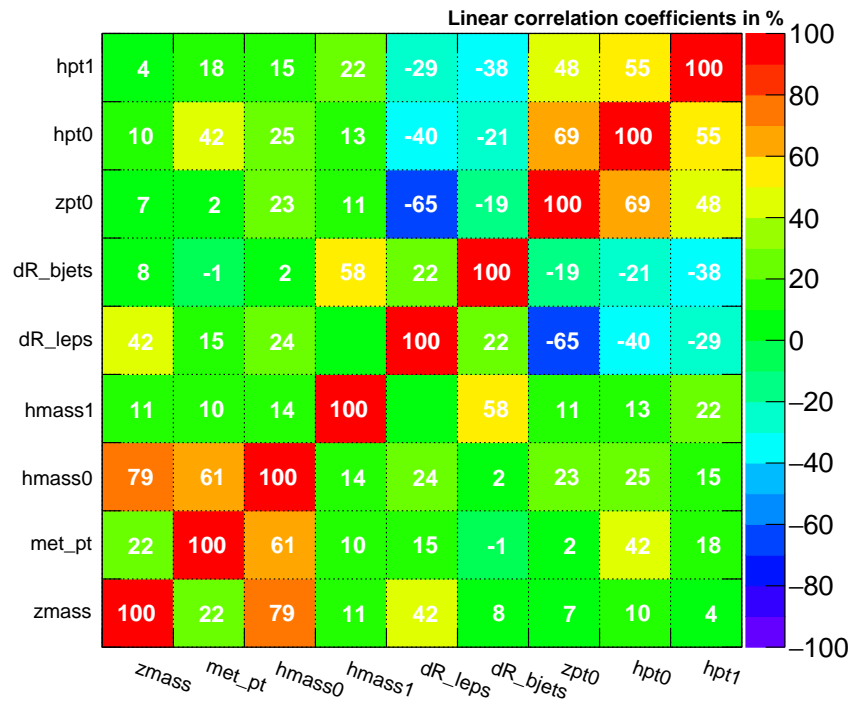


**Figure 9.14:** Input variables correlations for muon channel, high mass training. Top: signal sample mix. Bottom: background sample mix.

## CHAPTER 10

---

### Systematic Uncertainties

---

Systematic uncertainties that affect the sensitivity of our di-Higgs search come from a variety of sources such as theoretical uncertainties on cross sections or proton structure, experimental uncertainties related to the modelling of the detector response, the amount of collected data, and the discrepancies between the simulated samples and the real data.

Systematic uncertainties can be divided into two broad categories: those affecting only the yields of selected events from different processes (the "normalization" uncertainties) and those that, in addition to the change in rate, may distort the shape of the  $\tilde{M}_T(\text{HH})$  distribution used in the extraction of the limits (the "shape" uncertainties).

### 10.1 Normalization uncertainties

The sources of systematic uncertainties that affect normalizations are discussed in the list below. The sizes of some systematic uncertainties may vary depending on the resonance mass hypothesis and the decay channel of the leptonically decaying Zboson, in which cases ranges of the uncertainty values are listed. Normalization uncertainties discussed in this section do not affect the normalizations of the  $t\bar{t}$  and DY backgrounds because those are determined from data during the simultaneous fit

of the signal and control regions.

- **Luminosity** - CMS estimated this uncertainty on the integrated luminosity of the CMS 2016 data set to be 2.5% [?]. This uncertainty directly affects the expected event yields for the signal processes as well as all background processes except for the two dominant backgrounds, DY and  $t\bar{t}$ .
- **Pileup** - Signal and background event yields depend on the accuracy of the reproduction of pileup interactions in each simulated event. The effect of pileup is considered on each process. The recommended nominal value of 69.2 mb is used for the total inelastic pp cross section, for Down and Up variations, the values of 66.02 and 72.38 mb are used respectively, reflecting the imperfect knowledge of the total inelastic proton-proton interaction cross section at 13 TeV. The effect is seen only in the normalization and we, thus, consider this a normalization uncertainty and assign the value of 6%.
- **Proton PDF** - The systematic bias associated with the limited knowledge of the interacting proton content is evaluated using an ensemble of a hundred of PDF replicas from the NNPDF set [?] following the PDF4LHC prescription [?,?] and the RMS of the resulting process normalizations is taken as a measure of the bias. It is found to be of order 5%.
- **QCD scales** - Theoretical uncertainties in the QCD factorization and renormalization scales affect the expected yield of the signal and background events, excluding the  $t\bar{t}$  and DY yields as mentioned earlier. This uncertainty is estimated by varying independently these two scales in simulation by factors 0.5 and 2 with respect to the nominal values of the scales. The unphysical cases with one of the scales fluctuating up while the other fluctuates down are dis-

carded. In each bin of the HH transverse mass distribution the maximum and minimum variation are used to build an envelope around the nominal shape, resulting in the effect of the size 4-6% on the processes' yields.

- **Missing transverse energy/momentum** - Clustered energy in jets and leptons undergo energy corrections during event reconstruction, however, neutral hadrons and photons that do not belong to any jet ("unclustered energy") and jets with low transverse momenta (below 10 GeV) lack such corrections. This results in a small systematic bias in the reconstructed missing transverse momentum.  $\cancel{E}_T$  enters the  $\tilde{M}_T(\text{HH})$  variable, thus the effect of the unclustered energy has to be studied. We shift the energy of each particle not contained in jets or contained in low- $p_T$  jets by its uncertainty Up and Down. Such variations affect the event yields of signal and background processes at about 3% level but do not have a visible effect on the shape of the HH transverse mass, thus this source is categorised as a "normalization" systematic source.

## 10.2 Shape uncertainties

Several sources of systematic uncertainties affect not only the rate but also the shapes of various kinematic distributions which are inputs to the BDT or a part of the  $\tilde{M}_T(\text{HH})$  construction, the BDT discriminant itself, and the shape of the  $\tilde{M}_T(\text{HH})$  distribution. Each source is varied separately within one standard deviation up and down, and the effect is propagated through all related variables resulting in the nominal shape of the HH invariant mass distribution and two modified shapes corresponding to the Up and Down variations. Such triplet of shapes is prepared for each channel, each mass hypothesis, and for all processes.

All these shapes are fit simultaneously in the signal extraction likelihood fit. The discussion of the these sources of uncertainties follows.

- **Lepton efficiency** - The effect of the detector on the reconstruction of the lepton: identification and isolation selection criteria, and the requirement to pass trigger selection requirements are studied separately and are used to account for data/MC discrepancies. The corrections are derived from large dedicated samples of Zboson decays and also have an error associated with the procedure. The uncertainty on lepton efficiency corrections are derived as a function of lepton  $p_T$  and  $\eta$  and is propagated to the final  $\tilde{M}_T(\text{HH})$  distributions. The effect of these uncertainties is sub-percent for the muon channel and up to 6% for the electron channel.
- **Jet energy scale** - The uncertainty on the jet energy scale affects  $H \rightarrow b\bar{b}$  mass and  $p_T$ , which are inputs to the BDT. In addition, jet energy scale directly affects  $H \rightarrow b\bar{b}$  mass and  $\cancel{E}_T$ , which are used during the construction of the HH invariant mass. Jet energy scale is varied Up and Down within one standard deviation of its uncertainty as a function of jet  $p_T$  and  $\eta$ , and the effect on the jet kinematics and on the  $\cancel{E}_T$  is calculated and propagated through the steps of the measurement yielding the variation of the HH invariant mass shape. Jet energy scale uncertainty, with all factors combined, has the effect on the yields of the signal and some background components as large as 5 to 10%.
- **Jet energy resolution** - Data and MC a different energy resolution, which also affects the final  $\tilde{M}_T(\text{HH})$  shapes via its effect on the dijet invariant mass for  $H \rightarrow b\bar{b}$  and its effect on the  $\cancel{E}_T$ . Jet energy resolution is varied in simulation by one standard deviation as a function of jet  $p_T$  and  $\eta$  and the effect is propa-

gated through the steps of the measurement. Its effect on the  $\tilde{M}_T(\text{HH})$  yield is typically order of 0.5%.

- **b-tagging and mistagging** - The efficiency to tag a  $q_b$ -jet and the probability to misidentify a different flavor or a gluon jet and tag it as a  $q_b$ -jet is corrected in MC samples by factors derived from flavor-enhanced jet samples. The uncertainties on these corrections are propagated through the whole analysis setup. The effect of the  $q_b$ -tagging efficiency (mistagging/flavor misidentification) is about 5% (7–10%) for the Drell-Yan process and at the sub-percent level for other processes (7–10%).
- **Bin-by-bin uncertainties** - Since the available statistics for the simulated MC samples is limited, the lack of events in some bins of the  $\tilde{M}_T(\text{HH})$  distribution is addressed by bin-by-bin (BBB) uncertainty. This effect may result in sizeable fluctuations of the bin content of the HH invariant mass shapes that enter the likelihood fit. Therefore, for each bin of the HH invariant mass distributions an individual nuisance parameter is added to the likelihood fit with the Gaussian constraint of one standard deviation of the yield uncertainty in that bin.

## CHAPTER 11

---

### Statistical Analysis

---

The results in this measurement are obtained with the maximum likelihood fit. We perform a simultaneous fit of the SR and both CRs for both dielectron and dimuon channels using the likelihood function constructed as a product of Poisson terms over all bins of the input  $\tilde{M}_T(\text{HH})$  distributions in the three regions (SR, CRDY, CRTT) with Gaussian terms to constrain the nuisance parameters:

$$L(r_{\text{signal}}, r_k | \text{data}) = \prod_{i=1}^{N_{\text{bins}}} \frac{\mu_i^{n_i} \cdot e^{-\mu_i}}{n_i!} \cdot \prod_{j=1}^{N_{\text{nuisances}}} e^{-\frac{1}{2}\theta_j^2}$$

where the product index  $i$  refers to the bin of the input distributions, the product index  $j$  refers to uncertainties accounted for by the fit model, and  $n_i$  is the number of observed data events in the bin  $i$ . The mean value for each of the Poisson distributions is computed as:

$$\mu_i = r_{\text{signal}} \cdot S_i + \sum_k r_k \cdot B_{k,i},$$

where  $k$  refers to the background process  $k$ , and  $B_{k,i}$  is the content of the bin  $i$  of

the background shape for a process  $k$ , while  $S_i$  is the content of the bin  $i$  of the signal shape. The parameter  $r_k$  sets the normalization of the background process  $k$  while  $r_{signal}$  is the signal strength parameter, all  $r$  parameters are floating freely in the fit. Two values of the signal strength parameter are of special interest:  $r_{signal} = 0$  describes the background-only hypothesis, while  $r_{signal} = 1$  corresponds to the case when the HH cross section matches the cross section used for the initial signal normalization inspired by BSM models, 2pb in our case. The terms  $\theta_j$  represent the set of nuisance parameters that are introduced into the likelihood function as Gaussian constraints.

Figure 8.4( 8.5) shows the HH transverse mass distributions for the signal and two control regions for both channels for the graviton (radion) resonance mass hypothesis with normalizations and shapes of all components adjusted according to the best-fit values. The signal sample is normalized to the cross section of 2 pb, a typical value for predictions of WED models (e.g., at 300 GeV), and is further scaled, as indicated on the Figure, to make it clearly visible.

With the given 2016 dataset, the fit results show no evidence for HH production through a narrow resonance, whose width is negligible in comparison to experimental resolution, in the mass range from 250 GeV to 1 TeV. Thus, upper 95 % confidence level limits on the HH production cross section are set using the modified frequentist  $CL_s$  approach (asymptotic  $CL_s$ ) [30–32, 51].

The observed and expected 95% upper CL limits for the full mass range and both resonances are listed in Table 12.2. We produce the standard CMS Brazilian-flag type of plot for the limits, shown in Fig. 12.3. The green and yellow bands correspond to one and two standard deviations around the expected limit respectively. Since 450 GeV is the separation boundary between two mass regions: low mass and high mass, the limit calculation is performed with both of the BDTs at 450 GeV, where

the discontinuity is seen in the figure. The Figure also shows the expected production cross section for a RS1 KK graviton/RS1 radion in WED models. This cross section is computed in [63] under the assumption of no mixing with the SM Higgs boson.

## CHAPTER 12

---

### Limits Extraction

---

Prior to the derivation of the expected limits, we had to make sure their values are the most sensitive limits that our analysis can set. For that, we have done an optimization study finding the best cut value on the BDT discriminant with the idea to yield the lowest (the most sensitive) limit.

## 12.1 Optimization for the best limit

For this study, before doing the combination of electron and muon channels, we have optimized each of the channels separately. Systematical uncertainties were present only of the normalization type ( $\ln N$ ), since we are statistically limited and systematics plays a secondary role. As an example, for a specific analysis setup the 300 GeV fit in the muon channel yields the limit ('r-value') 255.25 (with the systematics but neglecting BBB uncertainties), without systematics the 'r-value' is 238.25. The difference is 17 parts in 255.25, which is just 6.7 %.

As can be seen from the plots 12.1 and 12.2, for high mass region the best cut to use is 0.99 for both electron and muon channels. For low mass region, the situation is more complicated. Depending on the mass point (and channel!) one cut is better than the other. For electron channel for 400 and 450 GeV mass points the best cut

**Table 12.1:** Suboptimal BDT cuts used in the analysis

channel	260 and 270 GeV	300 and 350 GeV	400 and 450 GeV	600 GeV to 1000 GeV
muons	0.1	0.7	0.7	0.99
electrons	0.4	0.4	0.925	0.99

is 0.925. In the lower region, the situation changes, 0.2 for 260 GeV, 0.4 for 270 and 300 GeV, 0.825 for 350 GeV.

Running the whole analysis for each separate cut and channel and spin hypothesis is not possible computationally taking into account the number of samples and shapes one has to create and process. That is why a reasonable compromise is to observe that for  $260 \rightarrow 350$  GeV included, the suboptimal cut can be 0.4, being well inside the  $1\sigma$  error band. This leaves the whole mass range with just three different cut values. This approach of suboptimal cuts, cuts which are close the best values but, most importantly, can be shared among several mass points, is what we adopted for this measurement.

For instance, for muons the best cuts are: 0.1 for 260 and 270 GeV, 0.5 for 300 GeV, 0.7 for 350 GeV, 0.925 for 400 and 450 GeV. Taking the approach of suboptimal cuts, the values we kept are: 0.1 for 260 and 270 GeV, 0.7 for  $300 \rightarrow 450$  GeV included. This way we simplify the analysis to three different BDT cuts per channel and, at the same time, remain optimal within the error bands with respect to the best cut values. This is summarized in the Table 12.1.

## 12.2 Results from the fit

The extraction of the results is performed by what is called at CMS "Binned shape analysis". We used Higgs Combination Tool ("HiggsCombine") [118], which is a framework with the help of which the Higgs boson had been discovered. HiggsCombine is

based on the RooStats package that has been very popular in the HEP community for years.

We do a simultaneous fit ( $\tilde{M}_T(\text{HH})$  transverse mass distribution is used) of all three regions: signal region and two control regions, to extract both signal strength parameter as well as normalizations of  $t\bar{t}$  and Drell-Yan backgrounds. We use the following command to produce expected limits with the Asimov [31] toy dataset :

```
combine -M Asymptotic -t -1 -v 3 -m massValue -run blind comb_card_massValue.txt.
```

The results in the Table 12.2 are final limits produced with the combined data of electron and muon channels. The corresponding plots, from which these numbers were extracted, are shown on the Figs. 12.3.

Full postfit distributions (the naming emphasises that all regions are used in the fit, signal region included) are shown on the Figs. 8.4 for the graviton case and Figs. 8.5 for the radion case.

**Table 12.2:** The expected and observed HH production cross section upper limits at 95% CL for different narrow resonance graviton (top) and radion (bottom) mass hypotheses for both dielectron and dimuon channels combined.

Mass, GeV	Observed Limit, pb	Expected Limit, pb
250	253.5	589.1
260	272.2	585.9
270	274.4	537.5
300	380.0	434.4
350	330.6	309.4
400	90.4	119.9
450	59.8	63.3
500	31.0	36.6
550	14.5	20.2
600	9.8	12.7
650	18.5	11.1
700	16.1	10.1
750	13.7	8.8
800	10.1	6.5
900	8.1	4.8
1000	5.8	4.2

Mass, GeV	Observed Limit, pb	Expected Limit, pb
250	107.3	297.7
260	170.8	410.9
270	207.0	470.3
300	451.7	496.9
350	532.6	496.9
400	155.7	171.1
450	89.3	82.0
500	36.0	54.4
550	18.7	28.5
600	13.2	19.6
650	24.6	17.2
700	16.4	12.0
750	13.9	10.4
800	12.6	9.8
900	6.9	5.6
1000	5.7	4.5

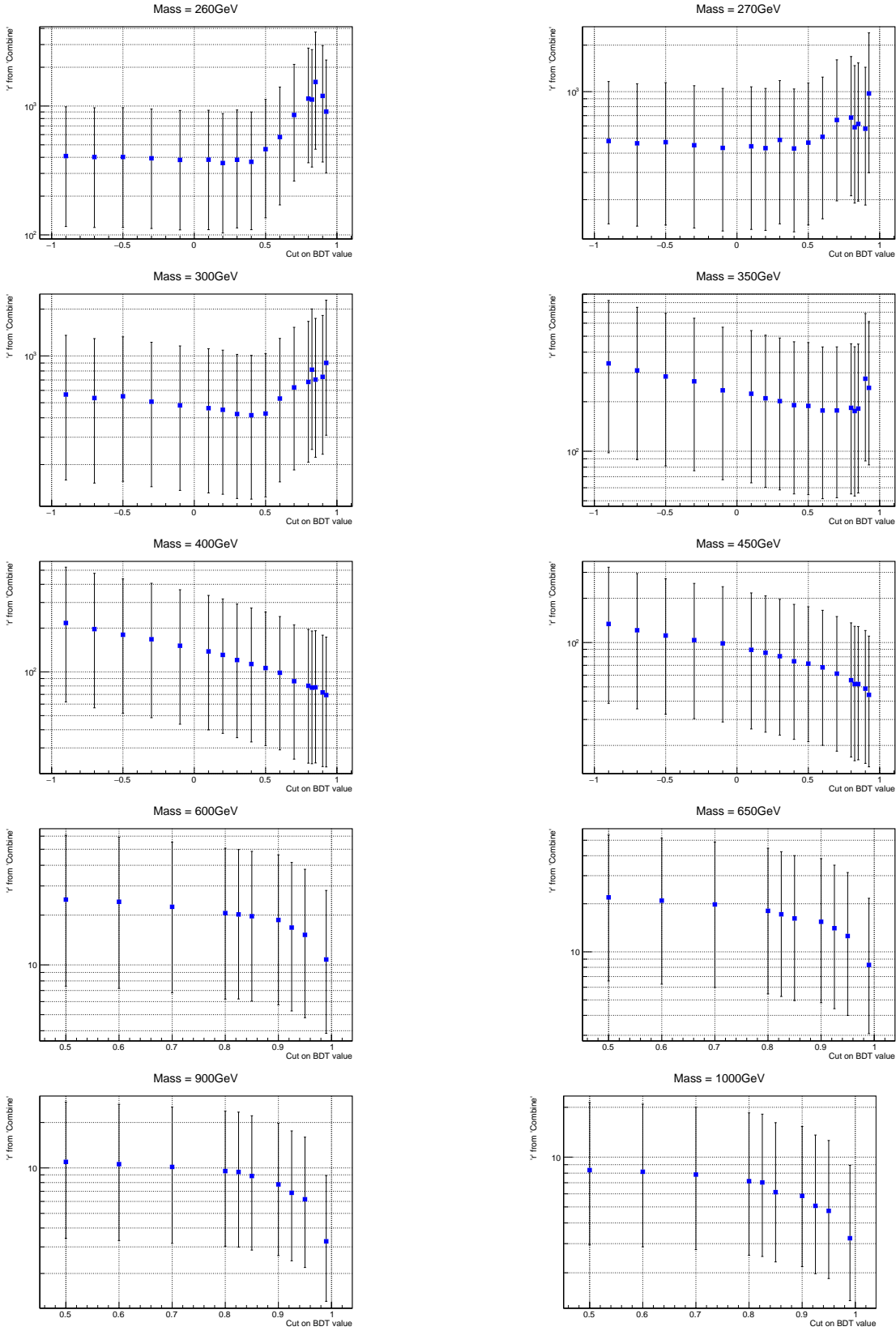


**Figure 12.1:** Cut on the BDT output vs 'r-value' from Combine. Electron channel.

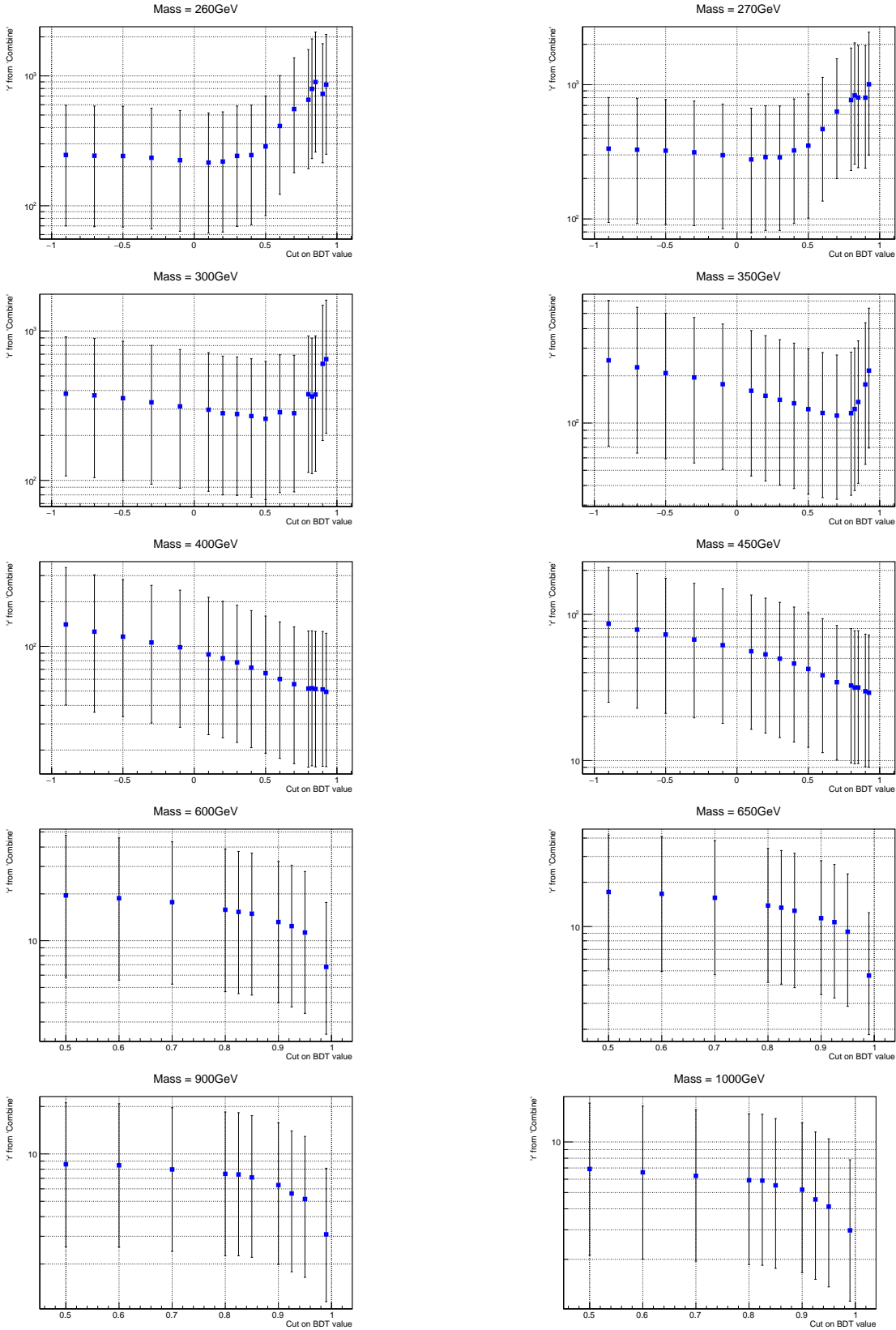


**Figure 12.2:** Cut on the BDT output vs 'r-value' from Combine. Muon channel.

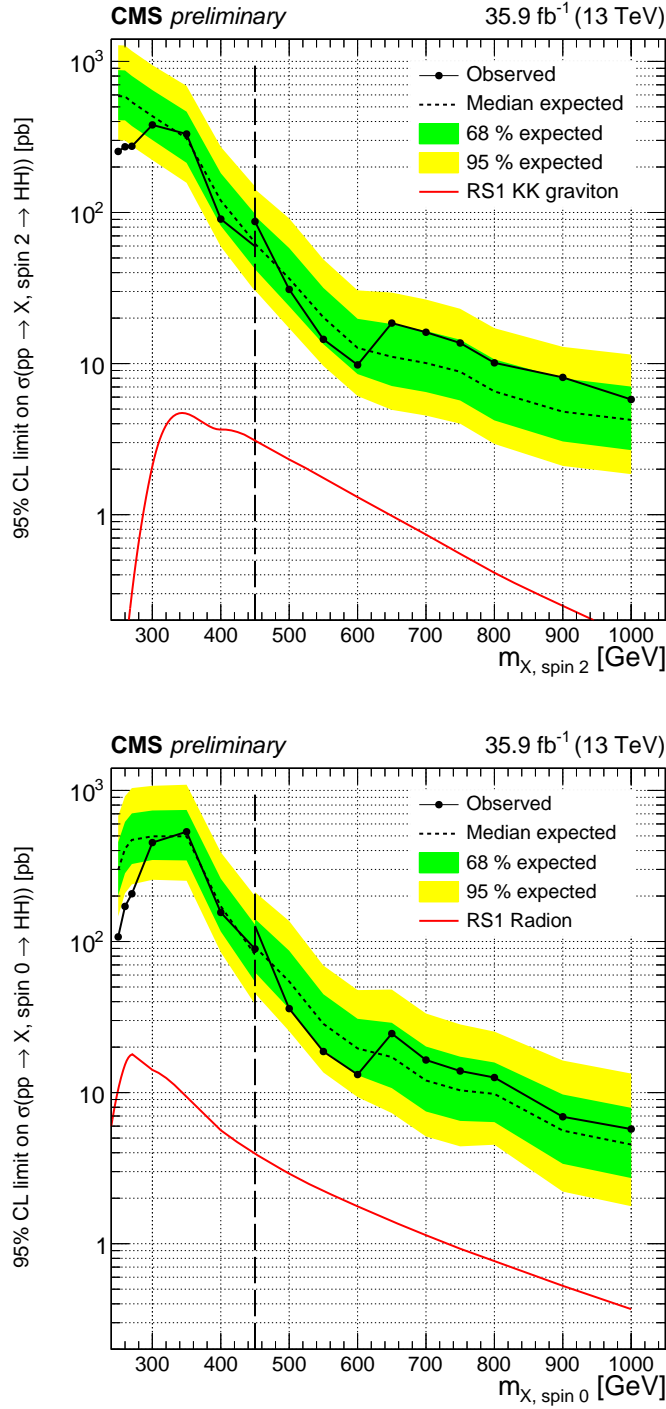


**Figure 12.3:** Expected (dashed line) and observed (solid line) limits on the cross section of a resonant HH production as a function of the mass of the narrow resonance for both leptonic channels combined. Graviton case is shown at the top and radion case at the bottom. The red line shows a theoretical prediction for the production of a WED particle with certain model assumptions [63].

## CHAPTER 13

---

### ***bbZZ measurements and combination of all HH channels***

---

Even for the HL-LHC with almost  $3\text{ ab}^{-1}$  of data, none of the HH analyses can reach the discovery sensitivity, thus the goal for all HH analyses now and in the nearest future is to contribute to the grand combination and only in this collaborative way to achieve the desired sensitivity. From the recent results of the HL-LHC HH combination projection analysis [145]: "the statistical combination of the five decay channels results in an expected significance for the standard model HH signal of  $2.6\sigma$ ". This is a clear sign that more data are needed. However, many Higgs analysts would agree that new statistical and MVA tools should be developed/employed. Thus, the next iteration of this analysis will most likely use a sophisticated neural network not only for the signal-background separation, but also for lepton reconstruction, etc.

This analysis is the search for the double Higgs boson production mediated by the intermediate graviton (and separately) by the radion in the  $\text{bbZZ}$  channel with the 2  $b$  jets, 2 leptons, 2 neutrinos final state with the  $35.9\text{ fb}^{-1}$  2016 dataset. According to the CMS Physics Coordination, for the paper in PRD this analysis has to be combined with the other  $\text{bbZZ}$  analysis, which is focused on the 2 bjets, 2 leptons, 2 jets signature. The mass range to be covered in the combined measurement is also from 250 GeV to 1000 GeV.

Regarding the latest grand combination for the spin 0 and spin 2 cases [146] shown

at the Fig. 13.1, the results are obtained for the extended mass range going from 250 GeV up to 3000 GeV, but no significant excess is found. The combination is done for the mass regions where at least two decay channels could contribute. Overall,  $b\bar{b}\gamma\gamma$  is the most sensitive channel in the low mass region and  $b\bar{b}b\bar{b}$  in the higher mass region (above  $\sim 500$  GeV).

This concludes the discussion of analysis details and in the next chapter we will summarise the main ideas that have been covered throughout this thesis.

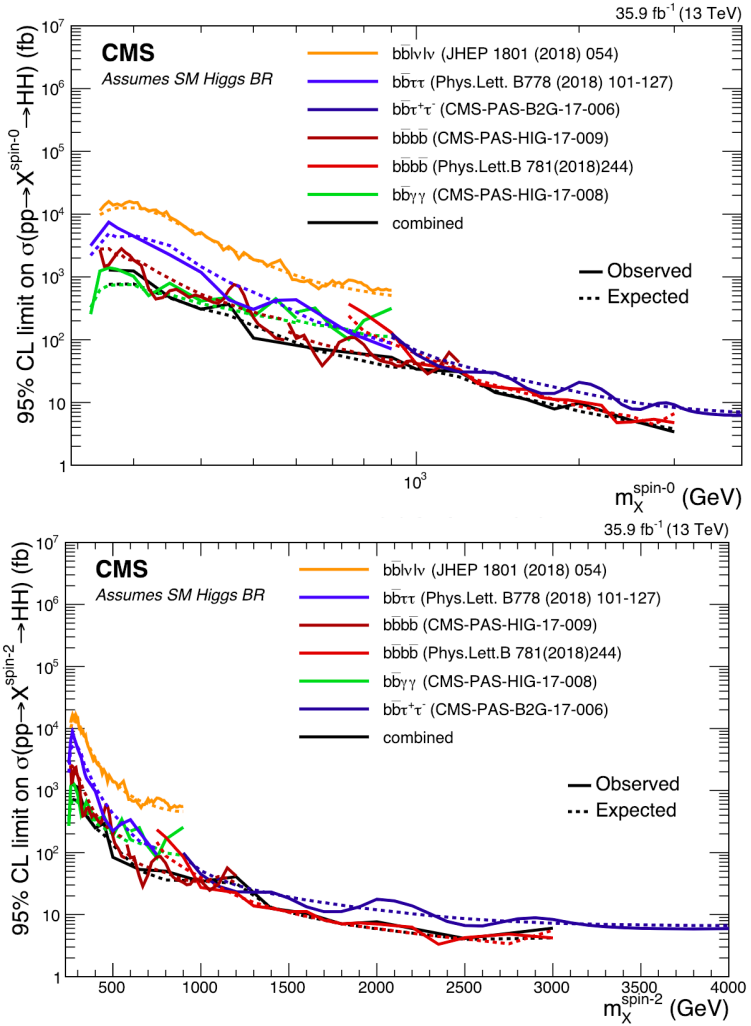


**Figure 13.1:** Combination of HH channels using 2016 data. Expected (dashed) and observed (solid line) 95% CL exclusion limits are shown. The results describe the production cross section of a narrow width spin 0 (top) and spin 2 (bottom) resonance decaying into a pair of SM Higgs bosons.

## CHAPTER 14

---

### Conclusions

---

This thesis described the search for the double Higgs boson production mediated separately by the KK graviton and by the radion heavy resonances in the  $bbZZ$  channel: one of the Higgs bosons decays to two  $q_b$  quarks while the other decays to a pair of Zbosons which, in turn, decay to a pair of neutrinos and a pair of electrons or muons. For this measurement we used 2016 data set with the integrated luminosity of  $35.9\text{fb}^{-1}$  collected by the CMS experiment at the LHC in the proton-proton collisions at  $\sqrt{s} = 13\text{ TeV}$ .

No statistically significant deviations from the SM predictions for background processes have been observed, and 95% upper confidence limits are reported for production cross section of a KK graviton/radion times the branching fraction of the subsequent decay into an HH system and further to our final state. The limits are derived for resonance masses in the 250 GeV to 1 TeV range.

This analysis became public in November 2018 [148]. Now, according to the CMS Physics Coordination, CMS would like to have a combination of this analysis with the other  $bbZZ$  analysis, which is focused on the 2 b jets, 2 leptons, 2 jets signature. Currents plans are to produce a paper for the Physical Review D (PRD), where we will report the best limits for all available  $bbZZ$  searches. Of course, prior to the grand  $bbZZ$  merge, each analysis combines the data from both dimuon and

dielectron channels. The mass range to be covered in the combined measurement is also from 250 GeV to 1000 GeV.

---

## References

---

- [1] Richard Phillips Feynman, Robert Benjamin Leighton, and Matthew Sands. *The Feynman lectures on physics; New millennium ed.* Basic Books, New York, NY, 2010. Originally published 1963-1965.
- [2] David J Griffiths. *Introduction to elementary particles; 2nd rev. version.* Physics textbook. Wiley, New York, NY, 2008.
- [3] Erwin Schrödinger. *Statistical thermodynamics; 2nd ed.* Cambridge Univ. Press, Cambridge, 1952.
- [4] E A Davis and Isabel Falconer. *J.J. Thompson and the discovery of the electron.* Taylor and Francis, Hoboken, NJ, 2002.
- [5] Oreste Piccioni. *The Discovery of the Muon*, pages 143–162. Springer US, Boston, MA, 1996.
- [6] Carl Bender. Mathematical physics.
- [7] G. Danby, J-M. Gaillard, K. Goulian, L. M. Lederman, N. Mistry, M. Schwartz, and J. Steinberger. Observation of high-energy neutrino reactions and the existence of two kinds of neutrinos. *Phys. Rev. Lett.*, 9:36–44, Jul 1962.

- [8] M. L. Perl, G. S. Abrams, and et al Boyarski. Evidence for anomalous lepton production in  $e^+ - e^-$  annihilation. *Phys. Rev. Lett.*, 35:1489–1492, Dec 1975.
- [9] K. Kodama et al. Observation of tau neutrino interactions. *Phys. Lett.*, B504:218–224, 2001.
- [10] Eric W. Weisstein. Fundamental forces.
- [11] S Chandrasekhar. *Newton's principia for the common reader*. Oxford Univ., Oxford, 2003. The book can be consulted by contacting: PH-AID: Wallet, Lionel.
- [12] Hanoch Gutfreund and Jurgen Renn. *The road to relativity: the history and meaning of Einstein's "The foundation of general relativity" : featuring the original manuscript of Einstein's masterpiece*. Princeton University Press, Princeton, NJ, Apr 2015.
- [13] J. Butterworth. *Smashing Physics*. Headline Publishing Group, 2014.
- [14] W N Cottingham and D A Greenwood. *An Introduction to the Standard Model of Particle Physics; 2nd ed.* Cambridge Univ. Press, Cambridge, 2007.
- [15] C. Patrignani et al. Review of Particle Physics. *Chin. Phys.*, C40(10):100001, 2016.
- [16] Andrew Wayne. QED and the Men Who Made It: Dyson, Feynman, Schwinger, and Tomonaga by Silvan S. Schweber. *The British Journal for the Philosophy of Science*, 46(4):624–627, 1995.
- [17] Michelangelo L Mangano. Introduction to QCD. (CERN-OPEN-2000-255), 1999.

- [18] R. P. Feynman. The theory of positrons. *Phys. Rev.*, 76:749–759, Sep 1949.
- [19] Matt Strassler. Of particular significance: Conversations about science with theoretical physicist matt strassler.
- [20] S.L. Glashow. Partial symmetries of weak interactions. *Nucl.Phys.*, 22:579–588, 1961.
- [21] F. Englert and R. Brout. Broken symmetry and the mass of gauge vector mesons. *Phys. Rev. Lett.*, 13:321–323, Aug 1964.
- [22] Peter W. Higgs. Broken symmetries and the masses of gauge bosons. *Phys. Rev. Lett.*, 13:508–509, Oct 1964.
- [23] G. S. Guralnik, C. R. Hagen, and T. W. B. Kibble. Global conservation laws and massless particles. *Phys. Rev. Lett.*, 13:585–587, Nov 1964.
- [24] Pauline Gagnon. *Who cares about particle physics? : making sense of the Higgs boson, the Large Hadron Collider and CERN*. Oxford University Press, 2016.
- [25] Precise determination of the mass of the Higgs boson and studies of the compatibility of its couplings with the standard model. Technical Report CMS-PAS-HIG-14-009, CERN, Geneva, 2014.
- [26] Jennifer Ouellette. Einstein’s quest for a unified theory. *APS*, 2015.
- [27] S. M. Bilenky. Neutrino in Standard Model and beyond. *Phys. Part. Nucl.*, 46(4):475–496, 2015.
- [28]

- [29] J. Alwall, R. Frederix, S. Frixione, V. Hirschi, F. Maltoni, O. Mattelaer, H. S. Shao, T. Stelzer, P. Torrielli, and M. Zaro. The automated computation of tree-level and next-to-leading order differential cross sections, and their matching to parton shower simulations. *JHEP*, 07:079, 2014.
- [30] Thomas Junk. Confidence level computation for combining searches with small statistics. *Nucl.Instrum.Meth.*, A434:435, 1999.
- [31] Glen Cowan, Kyle Cranmer, Eilam Gross, and Ofer Vitells. Asymptotic formulae for likelihood-based tests of new physics. *Eur. Phys. J.*, C71:1554, 2011. [Erratum: Eur. Phys. J.C73,2501(2013)].
- [32] SM Higgs Combination. Technical Report CMS-PAS-HIG-11-011, CERN, Geneva, 2011.
- [33] Matthew J. Dolan, Christoph Englert, and Michael Spannowsky. New Physics in LHC Higgs boson pair production. *Phys. Rev.*, D87(5):055002, 2013.
- [34] S. Frixione, P. Nason, and C. Oleari. Matching nlo qcd computations with parton shower simulations: the powheg method. *JHEP*, 11:070, 2007.
- [35] S. Agostinelli et al. GEANT4—a simulation toolkit. *Nucl. Instrum. Meth. A*, 506:250, 2003.
- [36] Gionata Luisoni, Paolo Nason, Carlo Oleari, and Francesco Tramontano.  $HW^\pm/HZ + 0$  and 1 jet at NLO with the POWHEG BOX interfaced to GoSam and their merging within MiNLO. *JHEP*, 10:083, 2013.
- [37] Comparison of nuisances for background only case, 350 GeV mass hypothesis.  
[http://rkamalie.web.cern.ch/rkamalie/feb12/Comparison\\_of\\_nuisances\\_expectedSignal0\\_350GeV.html](http://rkamalie.web.cern.ch/rkamalie/feb12/Comparison_of_nuisances_expectedSignal0_350GeV.html)

- [38] Comparison of nuisances for s+b case, 350 GeV mass hypothesis.  
[http://rkamalie.web.cern.ch/rkamalie/feb12/Comparison\\_of\\_nuisances\\_expectedSignal1\\_350GeV.html](http://rkamalie.web.cern.ch/rkamalie/feb12/Comparison_of_nuisances_expectedSignal1_350GeV.html)
- [39] k-factor for DY/Z. [https://twiki.cern.ch/twiki/bin/viewauth/CMS/SummaryTable1G25ns#DY\\_Z](https://twiki.cern.ch/twiki/bin/viewauth/CMS/SummaryTable1G25ns#DY_Z)
- [40] The LHC Higgs cross-section working group.  
<https://twiki.cern.ch/twiki/bin/view/LHCPhysics/LHCHXSWG>.
- [41] Standard Model Cross Sections for CMS at 13 TeV.  
<https://twiki.cern.ch/twiki/bin/viewauth/CMS/StandardModelCrossSectionsat13TeVInclusive>
- [42] SM Higgs production cross sections at  $\sqrt{s} = 13$  TeV.  
<https://twiki.cern.ch/twiki/bin/view/LHCPhysics/CERNYellowReportPageAt13TeV#ZHllH>
- [43] NNLO+NNLL top-quark-pair cross sections.  
[https://twiki.cern.ch/twiki/bin/view/LHCPhysics/TtbarNNLO#Top\\_quark\\_pair\\_cross\\_sections](https://twiki.cern.ch/twiki/bin/view/LHCPhysics/TtbarNNLO#Top_quark_pair_cross_sections)
- [44] Single Top Cross sections. <https://twiki.cern.ch/twiki/bin/viewauth/CMS/SingleTopSigma>.
- [45] CMS GEN XSEC Task Force. <https://twiki.cern.ch/twiki/bin/viewauth/CMS/GenXsecTaskForce>
- [46] SM Higgs Branching Ratios and Total Decay Widths (update in CERN Report4 2016).  
[https://twiki.cern.ch/twiki/bin/view/LHCPhysics/CERNYellowReportPageBR#Higgs\\_2\\_gauge](https://twiki.cern.ch/twiki/bin/view/LHCPhysics/CERNYellowReportPageBR#Higgs_2_gauge)
- [47] Ryan Gavin, Ye Li, Frank Petriello, and Seth Quackenbush. W Physics at the LHC with FEWZ 2.1. *Comput. Phys. Commun.*, 184:208, 2013.
- [48] Stefano Frixione, Paolo Nason, and Giovanni Ridolfi. A Positive-weight next-to-leading-order Monte Carlo for heavy flavour hadroproduction. *JHEP*, 09:126, 2007.

- [49] J. Alwall, R. Frederix, S. Frixione, V. Hirschi, F. Maltoni, O. Mattelaer, H. S. Shao, T. Stelzer, P. Torrielli, and M. Zaro. The automated computation of tree-level and next-to-leading order differential cross sections, and their matching to parton shower simulations. *JHEP*, 07:079, 2014.
- [50] Gunter Zech. Upper Limits in Experiments with Background Or Measurement Errors. *Nucl. Instrum. Meth.*, A277:608, 1989.
- [51] A. L. Read. Presentation of search results: the CLs technique. *J. Phys. G: Nucl. Part. Phys.*, 28, 2002.
- [52] Rikkert Frederix, Emanuele Re, and Paolo Torrielli. Single-top t-channel hadroproduction in the four-flavour scheme with POWHEG and aMC@NLO. *JHEP*, 09:130, 2012.
- [53] Johan Alwall et al. Comparative study of various algorithms for the merging of parton showers and matrix elements in hadronic collisions. *Eur. Phys. J. C*, 53:473–500, 2008.
- [54] Serguei Chatrchyan et al. Determination of jet energy calibration and transverse momentum resolution in CMS. *JINST*, 6:P11002, 2011.
- [55] John M. Campbell and R. K. Ellis. MCFM for the Tevatron and the LHC. *Nucl. Phys. Proc. Suppl.*, 205-206:10, 2010.
- [56] Emanuele Re. Single-top Wt-channel production matched with parton showers using the POWHEG method. *Eur. Phys. J.*, C71:1547, 2011.
- [57] Gael L. Perrin, Pedro Fernandez Manteca. Muon Identification and Isolation Scale-Factors on 2016 Dataset. <https://indico.cern.ch/event/611558/>

- [contributions/2465881/attachments/1407735/2151747/TnP\\_06\\_02\\_2017.pdf](https://twiki.cern.ch/twiki/bin/view/CMS/MuonWorkInProgressAndPagResults#Results_on_the_full_2016_data).
- [58] CMS Muon POG. Tracking SFs on the full 2016 data. [https://twiki.cern.ch/twiki/bin/view/CMS/MuonWorkInProgressAndPagResults#Results\\_on\\_the\\_full\\_2016\\_data](https://twiki.cern.ch/twiki/bin/view/CMS/MuonWorkInProgressAndPagResults#Results_on_the_full_2016_data).
- [59] Gael L. Perrin. Double Muon trigger efficiency per-leg approach. [https://indico.cern.ch/event/636555/contributions/2577291/attachments/1453162/2241537/TnP\\_DoubleMuSF\\_03\\_05\\_17.pdf](https://indico.cern.ch/event/636555/contributions/2577291/attachments/1453162/2241537/TnP_DoubleMuSF_03_05_17.pdf).
- [60] Peisi Huang, Aniket Joglekar, Min Li, and Carlos E. M. Wagner. Corrections to Di-Higgs Production with Light Stops and Modified Higgs Couplings. 2017.
- [61] Grace Dupuis. Collider Constraints and Prospects of a Scalar Singlet Extension to Higgs Portal Dark Matter. *JHEP*, 07:008, 2016.
- [62] Shinya Kanemura, Kunio Kaneta, Naoki Machida, Shinya Odori, and Tetsuo Shindou. Single and double production of the Higgs boson at hadron and lepton colliders in minimal composite Higgs models. *Phys. Rev.*, D94(1):015028, 2016.
- [63] Alexandra Oliveira. Gravity particles from Warped Extra Dimensions, predictions for LHC. 2014.
- [64] Oleg Antipin, David Atwood, and Amarjit Soni. Search for RS gravitons via  $W(L)W(L)$  decays. *Phys. Lett.*, B666:155–161, 2008.
- [65] A. Liam Fitzpatrick, Jared Kaplan, Lisa Randall, and Lian-Tao Wang. Searching for the Kaluza-Klein Graviton in Bulk RS Models. *JHEP*, 09:013, 2007.
- [66] Kaustubh Agashe, Hooman Davoudiasl, Gilad Perez, and Amarjit Soni. Warped Gravitons at the LHC and Beyond. *Phys. Rev.*, D76:036006, 2007.

- [67] CMS Higgs PAG. List of question for the preapproval checks. <https://twiki.cern.ch/twiki/bin/viewauth/CMS/HiggsWG/HiggsPAGPreapprovalChecks>.
- [68] CMS BTV POG. Supported Algorithms and Operating Points. [https://twiki.cern.ch/twiki/bin/viewauth/CMS/BtagRecommendation80XReReco#Supported\\_Algorithms\\_and\\_Operati](https://twiki.cern.ch/twiki/bin/viewauth/CMS/BtagRecommendation80XReReco#Supported_Algorithms_and_Operati).
- [69] Albert M Sirunyan et al. Search for resonant and nonresonant Higgs boson pair production in the bblnulnu final state in proton-proton collisions at  $\text{sqrt}(s) = 13 \text{ TeV}$ . 2017.
- [70] Abdus Salam and John Clive Ward. On a gauge theory of elementary interactions. *Nuovo Cim.*, 19:165–170, 1961.
- [71] Steven Weinberg. A model of leptons. *Phys.Rev.Lett.*, 19:1264–1266, 1967.
- [72] Albert M Sirunyan et al. Evidence for the Higgs boson decay to a bottom quark-antiquark pair. 2017.
- [73] Albert M Sirunyan et al. Particle-flow reconstruction and global event description with the CMS detector. *JINST*, 12(10):P10003, 2017.
- [74] Aruna Kumar Nayak. Reconstruction of physics objects in the CMS detector. *PoS*, CHARGED2012:010, 2012.
- [75] Lisa Randall and Raman Sundrum. Large mass hierarchy from a small extra dimension. *Phys. Rev. Lett.*, 83:3370–3373, Oct 1999.
- [76] Alexandra Oliveira. Gravity particles from Warped Extra Dimensions, predictions for LHC. 2014.

- [77] Serguei Chatrchyan et al. Observation of a new boson at a mass of 125 GeV with the CMS experiment at the LHC. *Phys. Lett.*, B716:30–61, 2012.
- [78] Georges Aad et al. Observation of a new particle in the search for the Standard Model Higgs boson with the ATLAS detector at the LHC. *Phys. Lett.*, B716:1–29, 2012.
- [79] Giuliano Panico. Prospects for double Higgs production. *Frascati Phys. Ser.*, 61:102, 2016.
- [80] I. Belotelov, I. Golutvin, D. Bourilkov, A. Lanyov, E. Rogalev, M. Savina, and S. Shmatov. Search for ADD extra dimensional gravity in di-muon channel with the CMS detector. CMS Note 2006/076, 2006.
- [81] M. Aldaya, P. Arce, J. Caballero, B. de la Cruz, P. Garcia-Abia, J. M. Hernandez, M. I. Josa, and E. Ruiz. Discovery potential and search strategy for the standard model Higgs boson in the  $H \rightarrow ZZ^* \rightarrow 4\mu$  decay channel using a mass-independent analysis. CMS Note 2006/106, 2006.
- [82] A. Brandt et al. Measurements of single diffraction at  $\sqrt{s} = 630$  GeV: Evidence for a non-linear  $\alpha(t)$  of the pomeron. *Nucl. Phys. B*, 514:3, 1998.
- [83] W. Buchmüller and D. Wyler. Constraints on SU(5)-type leptoquarks. *Phys. Lett. B*, 177:377, 1986.
- [84] CMS Collaboration. CMS technical design report, volume II: Physics performance. *J. Phys. G*, 34:995, 2007.
- [85] CMS Collaboration. Jet performance in pp collisions at  $\sqrt{s}=7$  TeV. CMS Physics Analysis Summary CMS-PAS-JME-10-003, 2010.

- [86] S. Chatrchyan et al. The CMS experiment at the CERN LHC. *JINST*, 3:S08004, 2008.
- [87] Particle Data Group, J. Beringer, et al. Review of Particle Physics. *Phys. Rev. D*, 86:010001, 2012.
- [88] ALEPH, CDF, D0, DELPHI, L3, OPAL, SLD Collaborations, the LEP Electroweak Working Group, the Tevatron Electroweak Working Group, and the SLD Electroweak and Heavy Flavour Groups. Precision electroweak measurements and constraints on the Standard Model. 2010.
- [89] I. Bertram, G. Landsberg, J. Linnemann, R. Partridge, M. Paterno, and H. B. Prosper. A recipe for the construction of confidence limits. Technical Report TM-2104, Fermilab, 2000.
- [90] L. Moneta, K. Belasco, K. S. Cranmer, A. Lazzaro, D. Piparo, G. Schott, W. Verkerke, and M. Wolf. The RooStats Project. In *13<sup>th</sup> International Workshop on Advanced Computing and Analysis Techniques in Physics Research (ACAT2010)*. SISSA, 2010. PoS(ACAT2010)057.
- [91] Vardan Khachatryan et al. Search for the standard model Higgs boson produced through vector boson fusion and decaying to  $b\bar{b}$ . *Phys. Rev.*, D92(3):032008, 2015.
- [92] Performance of muon identification in pp collisions at  $s^{**0.5} = 7$  TeV. Technical Report CMS-PAS-MUO-10-002, CERN, Geneva, 2010.
- [93] Serguei Chatrchyan et al. Performance of CMS muon reconstruction in  $pp$  collision events at  $\sqrt{s} = 7$  TeV. *JINST*, 7:P10002, 2012.

- [94] CMS COLLABORATION. Particle-flow event reconstruction in CMS and performance for jets, taus, and  $E_T^{miss}$ . CMS Physics Analysis Summary CMS-PAS-PFT-09-001, CERN, 2009.
- [95] CMS COLLABORATION. Commissioning of the particle-flow event reconstruction with the first lhc collisions recorded in the cms detector. CMS Physics Analysis Summary CMS-PAS-PFT-10-001, CERN, 2010.
- [96] Vardan Khachatryan et al. Performance of Electron Reconstruction and Selection with the CMS Detector in Proton-Proton Collisions at  $\sqrt{s} = 8$  TeV. *JINST*, 10(06):P06005, 2015.
- [97] CMS Collaboration. Search for pair production of first-generation scalar leptons in pp collisions at  $\sqrt{s} = 7$  TeV. Submitted to *Phys. Rev. Lett.*, 2010.
- [98] CMS Collaboration. Performance of cms muon reconstruction in pp collision events at  $\sqrt{s} = 7$  TeV. Submitted to *J. Inst.*, 2012.
- [99] ATLAS Collaboration. Search for the Higgs boson in the  $H \rightarrow WW^(*) \rightarrow \ell^+\nu\ell^-\bar{\nu}$  decay channel in pp collisions at  $\sqrt{s} = 7$  TeV with the ATLAS detector. Submitted to *Phys. Rev. Lett.*, 2011.
- [100] Matteo Cacciari and Gavin P. Salam. Dispelling the  $N^3$  myth for the  $k_t$  jet-finder. *Phys. Lett. B*, 641:57, 2006.
- [101] CMS Luminosity Measurements for the 2016 Data Taking Period. Technical Report CMS-PAS-LUM-17-001, CERN, Geneva, 2017.
- [102] CMS Muon POG. Reference muon id, isolation and trigger efficiencies for Run-II. <https://twiki.cern.ch/twiki/bin/viewauth/CMS/MuonReferenceEffsRun2>.

- [103] John M. Campbell, R. Keith Ellis, Paolo Nason, and Emanuele Re. Top-pair production and decay at NLO matched with parton showers. *JHEP*, 04:114, 2015.
- [104] Ryan Gavin, Ye Li, Frank Petriello, and Seth Quackenbush. FEWZ 2.0: A code for hadronic Z production at next-to-next-to-leading order. *Comput. Phys. Commun.*, 182:2388, 2011.
- [105] Ye Li and Frank Petriello. Combining QCD and electroweak corrections to dilepton production in FEWZ. *Phys. Rev. D*, 86:094034, 2012.
- [106] Vardan Khachatryan et al. Event generator tunes obtained from underlying event and multiparton scattering measurements. *Eur. Phys. J. C*, 76(3):155, 2016.
- [107] Torbjorn Sjostrand, Stephen Mrenna, and Peter Z. Skands. A Brief Introduction to PYTHIA 8.1. *Comput. Phys. Commun.*, 178:852–867, 2008.
- [108] Rikkert Frederix and Stefano Frixione. Merging meets matching in MC@NLO. *JHEP*, 12:061, 2012.
- [109] Simone Alioli, Paolo Nason, Carlo Oleari, and Emanuele Re. NLO single-top production matched with shower in POWHEG: s- and t-channel contributions. *JHEP*, 09:111, 2009. [Erratum: JHEP02,011(2010)].
- [110] Michele de Gruttola, Caterina Vernieri, Pierluigi Bortignon, David Curry, Ivan Furic, Jacobo Konigsberg, Sean-Jiun Wang, Paolo Azzurri, Tommaso Boccali, Andrea Rizzi, Silvio Donato, Stephane Brunet Cooperstein , James Olsen, Christopher Palmer, Lorenzo Bianchini, Christoph Grab, Gael Ludovic Perrin, and Luca Perrozzi. Search for the Standard Model Higgs Boson Produced in

- Association with W and Z and Decaying to Bottom Quarks. [http://cms.cern.ch/iCMS/jsp/db\\_notes/noteInfo.jsp?cmsnoteid=CMS%20AN-2015/168](http://cms.cern.ch/iCMS/jsp/db_notes/noteInfo.jsp?cmsnoteid=CMS%20AN-2015/168).
- [111] Michele de Gruttola, Rami Kamalieddin, Ilya Kravchenko, Lesya Shchutska. Search for resonant diHiggs production with bbZZ decays with the 2b2l2nu signature using 35.9/fb data of 2016 pp collisions at the LHC. [http://cms.cern.ch/iCMS/jsp/openfile.jsp?tp=draft&files=AN2017\\_198\\_v17.pdf](http://cms.cern.ch/iCMS/jsp/openfile.jsp?tp=draft&files=AN2017_198_v17.pdf).
- [112] Chris Palmer. VHbb Electron Trigger and ID+ISO SFs for 2016 data. [https://indico.cern.ch/event/604949/contributions/2543520/attachments/1439974/2216426/VHbb\\_TnP\\_SF\\_egamma\\_april.pdf#search=vhbb%20AND%20cerntaxonomy%3A%22Indico%2FExperiments%2FCMS%20meetings%2FPH%20%2D%20Physics%2FEgamma%22](https://indico.cern.ch/event/604949/contributions/2543520/attachments/1439974/2216426/VHbb_TnP_SF_egamma_april.pdf#search=vhbb%20AND%20cerntaxonomy%3A%22Indico%2FExperiments%2FCMS%20meetings%2FPH%20%2D%20Physics%2FEgamma%22).
- [113] CMS JetMET group. Jet Energy Resolution. <https://twiki.cern.ch/twiki/bin/viewauth/CMS/JetResolution>.
- [114] CMS MET group. MET Corrections and Uncertainties for Run-II. <https://twiki.cern.ch/twiki/bin/viewauth/CMS/MissingETRun2Corrections>.
- [115] CMS MET group. MET Filter Recommendations for Run II. <https://cern.ch/twiki/twiki/bin/view/CMS/MissingETOptionalFiltersRun2>.
- [116] CMS EGM POG. Multivariate Electron Identification for Run2. <https://twiki.cern.ch/twiki/bin/viewauth/CMS/MultivariateElectronIdentificationRun2>.
- [117] Helge Voss, Andreas Höcker, Jörg Stelzer, and Frerik Tegenfeldt. TMVA, the toolkit for multivariate data analysis with ROOT. In *XIth International Work-*

*shop on Advanced Computing and Analysis Techniques in Physics Research (ACAT)*, page 40, 2007.

- [118] CMS Higgs WG. Documentation of the RooStats -based statistics tools for Higgs PAG. <https://twiki.cern.ch/twiki/bin/view/CMS/SWGuideHiggsAnalysisCombinedLimit>.
- [119] CMS Higgs WG. Binned shape analysis with the Higgs Combination Tool. [https://twiki.cern.ch/twiki/bin/view/CMS/SWGuideHiggsAnalysisCombinedLimit#Binned\\_shape\\_analysis](https://twiki.cern.ch/twiki/bin/view/CMS/SWGuideHiggsAnalysisCombinedLimit#Binned_shape_analysis).
- [120] bbbb team. Search for resonant pair production of Higgs bosons decaying to bottom quark-antiquark pairs in proton-proton collisions at 13 TeV. <http://cms.cern.ch/iCMS/analysisadmin/get?analysis=HIG-17-009-pas-v5.pdf>.
- [121] Matteo Cacciari, Gavin P. Salam, and Gregory Soyez. The anti- $k_t$  jet clustering algorithm. *JHEP*, 04:063, 2008.
- [122] Torbjörn Sjöstrand, Stephen Mrenna, and Peter Skands. PYTHIA 6.4 physics and manual. *JHEP*, 05:026, 2006.
- [123] C. Giunti and M. Laveder. Neutrino mixing. In F. Columbus and V. Krasnoholovets, editors, *Developments in Quantum Physics*. Nova Science Publishers, Inc., 2004.
- [124] Savas Dimopoulos, Stuart Raby, and Frank Wilczek. Proton decay in supersymmetric models. *Physics Letters B*, 112(2):133 – 136, 1982.
- [125] M. Della Negra, P. Jenni, and T. S. Virdee. Journey in the search for the higgs boson: The atlas and cms experiments at the large hadron collider. *Science*, 338(6114):1560–1568, 2012.

- [126] Matthias U. Mozer. Electroweak Physics at the LHC. *Springer Tracts Mod. Phys.*, 267:1–115, 2016.
- [127] Roger Wolf. *The Higgs Boson Discovery at the Large Hadron Collider*, volume 264. Springer, 2015.
- [128] Steven Weinberg. The Making of the Standard Model. *Eur. Phys. J. C*, 34(hep-ph/0401010):5–13. 21 p. ; streaming video, 2003.
- [129] Jose Andres Monroy Montanez, Kenneth Bloom, and Aaron Dominguez. Search for production of a Higgs boson and a single Top quark in multilepton final states in pp collisions at  $\sqrt{s} = 13$  TeV, Jul 2018. Presented 23 Jul 2018.
- [130] Albert M Sirunyan et al. Search for Higgs boson pair production in the  $\gamma\gamma b\bar{b}$  final state in pp collisions at  $\sqrt{s} = 13$  TeV. 2018.
- [131] Lisa Randall and Raman Sundrum. A Large mass hierarchy from a small extra dimension. *Phys. Rev. Lett.*, 83:3370–3373, 1999.
- [132] Kunihiro Uzawa, Yoshiyuki Morisawa, and Shinji Mukohyama. Excitation of Kaluza-Klein gravitational mode. *Phys. Rev.*, D62:064011, 2000.
- [133] H. Davoudiasl, J. L. Hewett, and T. G. Rizzo. Phenomenology of the Randall-Sundrum Gauge Hierarchy Model. *Phys. Rev. Lett.*, 84:2080, 2000.
- [134] Michael Forger and Hartmann Romer. Currents and the energy momentum tensor in classical field theory: A Fresh look at an old problem. *Annals Phys.*, 309:306–389, 2004.
- [135] Chuan-Ren Chen and Ian Low. Double take on new physics in double Higgs boson production. *Phys. Rev.*, D90(1):013018, 2014.

- [136] Roberto Contino, Margherita Ghezzi, Mauro Moretti, Giuliano Panico, Fulvio Piccinini, and Andrea Wulzer. Anomalous Couplings in Double Higgs Production. *JHEP*, 08:154, 2012.
- [137] Gennadi Sardanashvily. *Noether's theorems: applications in mechanics and field theory*. Atlantis studies in variational geometry. Springer, Paris, 2016.
- [138] Thomas Schörner-Sadenius. *The Large Hadron Collider: harvest of run 1*. Springer, Cham, 2015.
- [139] CERN. *Large Hadron Collider in the LEP Tunnel*, Geneva, 1984. CERN.
- [140] Lyndon R Evans and Philip Bryant. LHC Machine. *JINST*, 3:S08001. 164 p, 2008. This report is an abridged version of the LHC Design Report (CERN-2004-003).
- [141] Karsten Eggert, K Honkavaara, and Andreas Morsch. Luminosity considerations for the LHC. Technical Report CERN-AT-94-04-DI. CERN-LHC-Note-263. LHC-NOTE-263, CERN, Geneva, Feb 1994.
- [142] Oswald Gröbner. The LHC Vacuum System. (LHC-Project-Report-181. CERN-LHC-Project-Report-181):5 p, May 1998.
- [143] Wolfgang Adam, R Frühwirth, Are Strandlie, and T Todor. Reconstruction of Electrons with the Gaussian-Sum Filter in the CMS Tracker at the LHC. Technical Report CMS-NOTE-2005-001, CERN, Geneva, Jan 2005.
- [144] Thomas Lenzi. Development and Study of Different Muon Track Reconstruction Algorithms for the Level-1 Trigger for the CMS Muon Upgrade with GEM Detectors. Master's thesis, U. Brussels (main), 2013.

- [145] Prospects for HH measurements at the HL-LHC. Technical Report CMS-PAS-FTR-18-019, CERN, Geneva, 2018.
- [146] Combination of searches for Higgs boson pair production in proton-proton collisions at  $\sqrt{s} = 13$  TeV. Technical Report CMS-PAS-HIG-17-030, CERN, Geneva, 2018.
- [147] The CMS collaboration. Missing transverse energy performance of the cms detector. *Journal of Instrumentation*, 6(09):P09001, 2011.
- [148] Search for resonant double Higgs production with  $b\bar{b}ZZ$  decays in the  $b\bar{b}\ell\ell\nu\nu$  final state. Technical Report CMS-PAS-HIG-17-032, CERN, Geneva, 2018.